



**LASER INTENSITY SCALING THROUGH  
STIMULATED SCATTERING IN OPTICAL FIBERS**

DISSERTATION

Timothy H. Russell, Captain, USAF  
AFIT/DS/ENP/02-3

**DEPARTMENT OF THE AIR FORCE  
AIR UNIVERSITY**

**AIR FORCE INSTITUTE OF TECHNOLOGY**

**Wright-Patterson Air Force Base, Ohio**

APPROVED FOR PUBLIC RELEASE; DISTRIBUTION UNLIMITED

| Report Documentation Page  |                             |  |
|--|-----------------------------|--|
| <b>Report Date</b><br>17 Dec 2001  | <b>Report Type</b><br>Final | <b>Dates Covered (from... to)</b><br>Sept 1998 - Dec 2001        |
| <b>Title and Subtitle</b><br>Laser Intensity Scaling Through Stimulated Scattering in Optical Fibers   |                             | <b>Contract Number</b>   |
|  |                             | <b>Grant Number</b>  |
|  |                             | <b>Program Element Number</b>                                    |
| <b>Author(s)</b><br>Capt Timothy H. Russell, USAF  |                             | <b>Project Number</b>  |
|  |                             | <b>Task Number</b>   |
|  |                             | <b>Work Unit Number</b>  |
| <b>Performing Organization Name(s) and Address(es)</b><br>Air Force Institute of Technology Graduate School of Engineering and Management (AFIT/EN) 2950 P Street, Bldg 640 WPAFB, OH 45433-7765   |                             | <b>Performing Organization Report Number</b><br>AFIT/DS/ENP/02-3 |
| <b>Sponsoring/Monitoring Agency Name(s) and Address(es)</b><br>Howard Schlossberg AFOSR/NE Air Force Office of Scientific Research 801 North Randolph Street, Rm 732 Arlington, VA 22203   |                             | <b>Sponsor/Monitor's Acronym(s)</b>                              |
|  |                             | <b>Sponsor/Monitor's Report Number(s)</b>                        |
| <b>Distribution/Availability Statement</b><br>Approved for public release, distribution unlimited  |                             |  |
| <b>Supplementary Notes</b><br>The original document contains color images.   |                             |  |
| <b>Abstract</b><br>The influence of stimulated scattering on laser intensity in fiber optic waveguides is examined. Stimulated Brillouin scattering (SBS) in long, multimode optical waveguides is found to generate a Stokes beam that propagates in the fiber LP01 mode. Additionally, the same process is found to combine multiple laser beams into a single spatially coherent source. Limitations in beam cleanup and combining are also investigated to identify ways to overcome them. The last portion of the dissertation theoretically examines suppression of stimulated Raman scattering in fibers to eliminate the restriction this imposes on the power of a fiber laser or amplifier. The suppression was modeled using both a holmium dopant and adding a long period grating to the fiber. |                             |  |
| <b>Subject Terms</b><br>Lasers, Optics, Fiber Optics, Nonlinear Optics, Electromagnetic Scattering, Coherent scattering, Light scattering, Raman scattering, Stokes radiation  |                             |  |

|   |  |
|---|--|
| <b>Report Classification</b><br>unclassified      | <b>Classification of this page</b><br>unclassified |
| <b>Classification of Abstract</b><br>unclassified | <b>Limitation of Abstract</b><br>UU                |
| <b>Number of Pages</b><br>204                     |  |

The views expressed in this dissertation are those of the author and do not reflect the official policy or position of the United States Air Force, Department of Defense, or the U. S. Government.

**LASER INTENSITY SCALING THROUGH  
STIMULATED SCATTERING IN OPTICAL FIBERS**

**DISSERTATION**

Presented to the Faculty  
Graduate School of Engineering and Management  
Air Force Institute of Technology  
Air University  
Air Education and Training Command  
in Partial Fulfillment of the Requirements for the  
Degree of Doctor of Philosophy

Timothy H. Russell, BS, MS

Captain, USAF

December 2001

APPROVED FOR PUBLIC RELEASE; DISTRIBUTION UNLIMITED

# LASER INTENSITY SCALING THROUGH STIMULATED SCATTERING IN OPTICAL FIBERS

Timothy H. Russell, BS, MS  
Captain, USAF

Approved:

Date

Tom S. Roberts

10 Dec 01

Won B. Roh (Chairman)

Won B. Roh (Chairman)  
  
Eric B. Roh

10 DEC 01

---

**Eric P. Magee (Member)**

  
John R. Marcante (Member)

5 Dec 2001

## **John R. Marciano (Member)**

  
Michael A. Marciniak (Member)

14 Dec 01

Michael A. Marciak (Member)

Kenneth W. Bauer Jr.

10 DEC 01

Kenneth W. Bauer, Jr. (Dean's Representative)

Accepted:

Accepted,  
John A. Lahr b

10 Dec 2001

Date

Robert A. Calico, Jr.

## Dean, Graduate School of Engineering and Management

### *Acknowledgments*

Over the last three years, in addition to the support I was given through my faith in God, I have enjoyed the technical and inspirational support of many people. I cannot mention everyone that provided help or the acknowledgments would take up the lion's share of the dissertation, but I would like to highlight some of the major contributors.

Dr. Roh's technical guidance was invaluable. He allowed me to forge my own path, but was always available to point me in the direction of an easier road. His open attitude encouraged me to ask questions that enhanced my understanding of nonlinear optics. His laboratory skills saved me time and demonstrated a strong methodology for conducting experiments. For these things, I will always be grateful.

My family and friends have also provided valuable help. While on vacation visiting Dayton, my mom spent time writing down and collecting data. She helped format the dissertation, saving me precious time in the final stages of writing. Most of all, along with the rest of my family, she never wavered in her belief in me. In fact, according to Mom, every question that I answered incorrectly on my tests and homework is most likely due to a poorly worded question.

Finally, I must thank my wife. Through my frustrations and fears, she has stood firm, encouraging me to continue to try when I felt there was no hope and forcing me to take breaks when my efforts had turned fruitless. She stayed up late with me, reading papers, examining figures, and printing out presentations so that I could get some much needed sleep. She brought me dinner and clothes when I had to stay at school late

and most important of all, through everything, she listened. With the ability to place her own problems in the back of her mind, she paid attention to mine. Without that support, I could have never have gotten where I am.

## *Table of Contents*

|  | Page  |
|--|-------|
| Acknowledgments.....                             | iv    |
| List of Figures .....                            | ix    |
| List of Tables .....                             | xvi   |
| List of Publications .....                       | xvii  |
| Abstract.....                                    | xviii |
| 1. Introduction.....                             | 1     |
| 1.1 Motivation.....                              | 1     |
| 1.2 Overview.....                                | 3     |
| 1.3 Document Organization .....                  | 6     |
| 2. Propagation of Light in Optical Fibers .....  | 8     |
| 2.1 Core Guided Fiber Modes.....                 | 8     |
| 2.2 Cladding-Guided Fiber Modes .....            | 16    |
| 3. Stimulated Scattering in Optical Fibers ..... | 19    |
| 4. SBS Beam Cleanup.....                         | 28    |
| 4.1 Background.....                              | 28    |
| 4.2 Theoretical Beam Cleanup.....                | 29    |
| 4.3 Experimental Beam Cleanup .....              | 39    |

|       |   |     |
|-------|---|-----|
| 4.3.1 | 50-micron Beam Cleanup .....                    | 39  |
| 4.3.2 | SBS Polarization Properties.....                | 49  |
| 4.3.3 | High Spatial Order Stokes Modes.....            | 57  |
| 4.3.4 | Ring Cavity Beam Cleanup .....                  | 61  |
| 4.4   | Conclusions.....                                | 66  |
| 5.    | SBS Beam Combining .....                        | 69  |
| 5.1   | Background.....                                 | 69  |
| 5.2   | Coherent Combining.....                         | 70  |
| 5.2.1 | Two laser coherent combining.....               | 71  |
| 5.2.2 | Polarization properties .....                   | 75  |
| 5.2.3 | Spatial characteristics.....                    | 79  |
| 5.2.4 | Conclusions.....                                | 85  |
| 5.3   | Incoherent Combining .....                      | 86  |
| 5.3.1 | Independent excitation.....                     | 88  |
| 5.3.2 | Spatial Overlap.....                            | 94  |
| 5.3.3 | Spatial coherence .....                         | 98  |
| 5.3.4 | Conclusions.....                                | 101 |
| 6.    | SBS Beam Cleanup and Combining Limitations..... | 103 |
| 6.1   | Multiple Beam Combining .....                   | 103 |
| 6.2   | Second Order Threshold .....                    | 109 |
| 6.2.1 | Experimental Setup.....                         | 110 |
| 6.2.2 | Modeling.....                                   | 114 |
| 6.2.3 | Conclusions.....                                | 121 |
| 6.3   | SRS Beam Cleanup and Combining .....            | 122 |
| 6.3.1 | Experimental Setup.....                         | 124 |
| 6.3.2 | Results.....                                    | 126 |
| 6.3.3 | Conclusions.....                                | 130 |

|  |     |
|--|-----|
| 7. SRS Reduction Using Intercavity Dopants.....  | 133 |
| 7.1 Background.....                              | 133 |
| 7.2 Theory.....                                  | 140 |
| 7.2.1 Dopant Characterization .....              | 140 |
| 7.2.2 Threshold Calculation.....                 | 142 |
| 7.3 Conclusions.....                             | 144 |
| 8. SRS Reduction Using Long Period Gratings..... | 147 |
| 8.1 Raman Spectrum Measurement .....             | 148 |
| 8.1.1 Experimental Setup.....                    | 148 |
| 8.1.2 Results.....                               | 150 |
| 8.2 Long Period Grating Design .....             | 152 |
| 8.2.1 Theory.....                                | 152 |
| 8.2.2 Results.....                               | 157 |
| 8.3 Conclusions.....                             | 159 |
| 9. Conclusions.....                              | 161 |
| 9.1 Technical achievements .....                 | 161 |
| 9.2 Research impact.....                         | 164 |
| 9.2.1 Laser Cleanup and Combining.....           | 165 |
| 9.2.2 SRS Reduction.....                         | 167 |
| Appendix A. Fiber Cladding Modes.....            | 168 |
| Appendix B. Local Effective Brillouin Gain ..... | 174 |
| Bibliography .....                               | 177 |

## *List of Figures*

|  | Page |
|--|------|
| Figure 1: Normalized propagation constant for the modes of a fiber optic waveguide, with $V = 5$ .....   | 13   |
| Figure 2: The first four transverse mode patterns of a fiber optic waveguide .....   | 13   |
| Figure 3: (a,b) The transverse electric field pattern of the $LP_{01}$ and $LP_{11}$ modes at the front end of a representative 50 micron fiber. (c) The intensity distribution due to a superposition of the modes in (a,b). (d,e) The transverse electric field pattern of the $LP_{01}$ and $LP_{11}$ modes at a distance of $\pi/(k_{c01} - k_{c11})$ into the fiber. (f) The intensity distribution due to a superposition of the modes in (d,e)..... | 14   |
| Figure 4: Cladding mode dispersion relation.....   | 17   |
| Figure 5: (Top and Bottom Left) Cladding mode intensity distributions. Odd modes have a local maximum centered in the fiber core. Even modes have a local minimum in the fiber core. (Bottom Right) The lowest order core guided mode.....   | 18   |
| Figure 6: Raman gain spectrum .....  | 26   |
| Figure 7: Relative effective gain along the length of the fiber. (a) is the calculated value. (b) is the calculated value when the high frequency fluctuations are averaged out .....  | 33   |
| Figure 8: (a) Average phase conjugate fraction as a function of the fiber length. (b) Percentage of pump modes that lead to the excitation of the $LP_{01}$ Stokes mode versus the fiber length. ....  | 35   |
| Figure 9: Schematic of experiment used to examine beam cleanup.....  | 41   |
| Figure 10: Schematic depicting the experimental setup to investigate the dependence of pumping conditions on the efficiency.....   | 42   |
| Figure 11: Power in the Stokes beam as a function of the pump beam. The slope efficiency is 52.4% and the threshold is 420 mW.....   | 43   |

|  |    |
|--|----|
| Figure 12: (a) Pump beam shape, (b) Stokes beam shape, (c) Transmitted beam shape.....   | 43 |
| Figure 13: The Stokes beam does not significantly move as the input beam position is varied from the upper right to the lower left.....  | 46 |
| Figure 14: Transmission through (a) and Brillouin reflection from (b) an optical fiber as a function of pump power and pump beam position from one edge of the fiber core to the other.....  | 47 |
| Figure 15: Transmission of the pump beam through a 50-micron fiber versus pump beam position at various pump power levels. (a) Low power transmission below SBS threshold. (b-c) Transmission above threshold. (d) Effective cleanup diameter as a function of the pump power.....   | 49 |
| Figure 16: Schematic diagram of polarization characterization experiment.....  | 50 |
| Figure 17: Reflected pump (solid) and Stokes (dashed) power as a function of the analyzer angle. The two are out of phase by 90° showing that the polarization of the Stokes beam is orthogonal to that of the reflected pump.....   | 51 |
| Figure 18: Modal dispersion limits the fiber length if a polarized Stokes output is desired. The allowed fiber length is shown as a function of the pump beam fiber mode. The Stokes beam is assumed to propagate in the LP <sub>01</sub> mode.....  | 57 |
| Figure 19: Multimode Stokes beam experimental schematic.....   | 58 |
| Figure 20: (a) The intensity pattern of the Stokes beam generated by laser 1. (b) The intensity pattern of the Stokes beam generated by laser 2. (c) The intensity pattern of the Stokes beam generated when both lasers pump the fiber simultaneously at the same frequency. (d) The intensity pattern of the Stokes beam generated when both lasers pump the fiber simultaneously at different frequencies ..... | 60 |
| Figure 21: Ring cavity SBS beam cleanup experiment .....   | 62 |
| Figure 22: Stokes beam shapes at various levels of Stokes coupling into the back end of the fiber.....   | 64 |
| Figure 23: Stokes output at various levels of Stokes coupling into the back end of the fiber .....   | 65 |

|   |    |
|---|----|
| Figure 24: Beam shape of the coupled Stokes power in the ring cavity setup. ....  | 66 |
| Figure 25: Two beam coherent combining schematic. ....  | 72 |
| Figure 26: (Top) Scanning Fabry-Perot interferometer output when the pump beams are separated by more than the Brillouin gain bandwidth. Relative peak output of the Stokes beams is ~30. (Bottom) Interferometer output when the pump beams are tuned to the same frequency. Peak relative output is 100, more than twice that of each laser alone. .... | 73 |
| Figure 27: Stokes power as a function of the pump powers. ....  | 74 |
| Figure 28: Stokes power generated along the bold path shown in Figure 27.....   | 75 |
| Figure 29: Polarization analysis setup. ....  | 76 |
| Figure 30: (solid) Total Stokes power as a function of the pump power along the path indicated in bold on Figure 27. (dotted) Horizontally polarized Stokes power as a function of pump power. (dashed) Vertically polarized Stokes power as a function of pump power.....  | 77 |
| Figure 31: The degree of polarization (solid line) falls off rapidly as the second laser begins to pump the fiber, contributing to the overall Stokes output. This is relatively consistent with the predicted degree of polarization of an idealized pump beam (dotted line).....  | 79 |
| Figure 32: Two beam coherent combining schematic. ....  | 81 |
| Figure 33: Images of the pump beams from each path. a) The pump beam from path 1 (high intensities are indicated by dark regions). b) The pump beam from path 2 (high intensities are indicated by bright regions. c) Image of both pump beams. ....  | 83 |
| Figure 34: Images of the transmitted beams from each path. a) The transmitted beam from path 1 (high intensities are indicated by dark regions). b) The transmitted beam from path 2 (high intensities are indicated by bright regions. c) Image of both transmitted beams. ....  | 83 |
| Figure 35: Images of the Stokes beams from each path. a) The Stokes beam from path 1 (high intensities are indicated by dark  |    |

|  |     |
|--|-----|
| regions). b) The Stokes beam from path 2 (high intensities are indicated by bright regions. c) Image of both Stokes beams. ....  | 83  |
| Figure 36: (Top) Stokes beam (black) as a function of the position of the path-two pump (white). (Bottom) Relative SBS efficiency as a function of the path-two beam position. The power coupled into the fiber is shown by the solid line. ....   | 85  |
| Figure 37: Two beam incoherent combination experimental setup using a multimode fiber.....   | 89  |
| Figure 38: Polarimetric Stokes Power vs. Pump Power in mW. (a) SBS Power reflected into a horizontally polarized beam. (b) SBS Power reflected into a vertically polarized beam. (c) Total SBS Power. ....   | 91  |
| Figure 39: The indicated path of Figure 38(c) shows that the two input beams must each overcome a threshold before contributing to the Stokes beam. ....   | 91  |
| Figure 40: Slices through Figure 38(c) at different values of laser B (A) and laser A (B). Each slice is normalized at the left side. The similarity of each curve indicates that the lasers produce independent Stokes beams. ....  | 93  |
| Figure 41: Dual pump and SBS spectrum generated from a Fabry-Perot interferometer with a free spectral range of 8 GHz. ....  | 93  |
| Figure 42: Reflected beam overlap. (a) Image of Laser A. Lighter shades indicate higher intensity. (b) Image of Laser B. Darker shades indicate higher intensity. (c) Combined laser beams showing significant mismatch between the reflected positions of laser A and laser B. ....     | 96  |
| Figure 43: Transmitted beam overlap. (a) Image of Laser A. Lighter shades indicate higher intensity. (b) Image of Laser B. Darker shades indicate higher intensity. (c) Combined laser beams showing significant mismatch between the transmitted positions of laser A and laser B. .... | 96  |
| Figure 44: SBS beam overlap. (a) Image of Laser A. Lighter shades indicate higher intensity. (b) Image of Laser B. Darker shades indicate higher intensity. (c) Combined laser beams showing the two SBS beams are nearly coaxial. ....  | 96  |
| Figure 45: Experimental setup for spatial coherence measurement. ....  | 100 |

|   |     |
|---|-----|
| Figure 46: Interference patterns of the Stokes beam demonstrating its spatial coherence.....  | 101 |
| Figure 47: Multi-beam coupling for beam combining.....  | 105 |
| Figure 48: Fiber bundle multiple beam combining schematic diagram. ....   | 105 |
| Figure 49: Definition of beam size variables.....   | 107 |
| Figure 50: Tapered fiber bundle designed by Lucent Technologies [53].....   | 109 |
| Figure 51: Schematic of the experimental setup used to measure the second order Stokes threshold. ....  | 111 |
| Figure 52: Transmitted spectrum through a long fiber above second order threshold.....  | 111 |
| Figure 53: (a-c) Power transmitted through the SMF-28 fiber as a function of the input power at the pump, Stokes and second order Stokes frequencies. The solid lines indicate the best theoretical fit. The dashed lines show the best fit ignoring either second order SBS contributions or four wave mixing effects. (d) The first Stokes power as a function of input power.....  | 113 |
| Figure 54: (a-c) Power transmitted through the SMF-28 fiber as a function of the input power at the pump, Stokes and second order Stokes frequencies when the front fiber facet was cleaved at an angle. The solid lines indicate the best theoretical fit. The dashed lines show the best fit ignoring either second order SBS contributions or four wave mixing effects. (d) The first Stokes power as a function of input power..... | 114 |
| Figure 55: (a) Relative Stokes power distribution in a fiber for a 20 mW pump beam (solid) and a 800 mW pump beam (dashed). (b) Second-order effective length as a function of input power for a 4.4 km fiber.....  | 121 |
| Figure 56: Schematic diagram of stimulated Raman scattering beam cleanup.....   | 125 |
| Figure 57: Near- and Far-field images of the pump and Stokes beams transmitted through a 300 m multimode fiber. ....  | 127 |
| Figure 58: Circles (squares) indicate the measured size of the Stokes (pump) beam at various distances from the lens. The solid lines show the best fit to the data points. ....  | 128 |

|  |     |
|--|-----|
| Figure 59: (Top) The spectrum of the beam transmitted through the fiber.<br>(Bottom) The spectrally dispersed near-field image of the<br>transmitted beam.....   | 129 |
| Figure 60: (a) Spot size of the pump (circles) and first order Stokes<br>(squares) beams at the fiber facet. (b,c) Pump (left) and<br>Stokes (right) intensity distributions for a 300 m and 75 m fiber<br>respectively.....   | 130 |
| Figure 61: Double clad fiber.....  | 133 |
| Figure 62: Emission Spectrum of Nd in a crystal and in glass [11]. .....   | 135 |
| Figure 63: Absorption of typical optical fiber [13].....   | 138 |
| Figure 64: Transmission of a 5mm thick silicate glass window doped with<br>2 mol% of Ho. The dashed line indicates the location of a<br>typical laser pump, the solid line shows the wavelength of the<br>laser, and the dotted line represents the first order Stokes beam.....                     | 141 |
| Figure 65: Holmium absorption in silicate glass (dotted line) along with<br>the Raman gain (solid line) as a function of the frequency shift<br>from a neodymium pump beam at 1.064 microns (a) and as a<br>function of the frequency shift from a ytterbium pump beam at<br>1.094 microns (b). .... | 142 |
| Figure 66: The threshold for SRS generation pumped at 1.064 microns<br>(dashed line) and at 1.09 microns (solid line) calculated versus<br>the molar % of holmium doped into the fiber.....  | 144 |
| Figure 67: A long period grating couples light out of the core and into the<br>fiber cladding where high losses account for the reduction in<br>transmission. ....   | 147 |
| Figure 68: Schematic for Raman spectrum measurement.....   | 149 |
| Figure 69: Stokes spectra at different pump power levels in (a) a 0.5 m<br>fiber, (b) a 1 m fiber, and (c) a 200 m fiber. The dashed lines<br>in (a) and (b) indicate the transmission spectrum of the Raman<br>notch filter used in those experimental setups to attenuate the<br>pump beam.....    | 150 |
| Figure 70: Raman gain spectrum for various types and concentrations of<br>dopants [83]. .....  | 151 |
| Figure 71: Proportionality constant for the efficiency of the coupling<br>between the LP <sub>01</sub> and cladding modes [12]. The odd cladding   |     |

modes are designated with triangles. The even cladding modes  
are designated with squares.....154

Figure 72: LPG transmission (solid) and Raman gain (dashed) as a  
function of the frequency difference from the pump beam at  
1.064 microns. (a) A single long period grating with the HE<sub>13</sub>  
mode centered at 440 cm<sup>-1</sup>. (b) A single grating design placed  
at three points in the fiber. (c) One set of three different  
gratings. (d) Three sets of three different gratings.....157

### *List of Tables*

|   | Page |
|---|------|
| Table 1: Beam quality factors for beam cleanup experiment .....         | 45   |
| Table 2: Beam quality factors for ring cavity SBS experiment. ....      | 64   |
| Table 3: Measured polarization components. ....                         | 76   |
| Table 4: Conversion from the measured values to Stokes parameters. .... | 76   |
| Table 5: Misalignment calculation.....                                  | 84   |
| Table 6: Quantitative measure of beam overlap .....                     | 98   |
| Table 7: Fit parameters for second order Stokes threshold model.....    | 116  |
| Table 8: Critical parameters for several LPG designs. ....              | 158  |

## ***List of Publications***

### Peer Reviewed Journals

Russell, T.H., W.B. Roh, and J.R. Marciante, *Incoherent beam combining using stimulated Brillouin scattering in multimode fibers*. Optics Express, 2001. **8**(4): p. 246-254. - This paper became the subject of a full-page World News story in Laser Focus World magazine in the April 2001 Issue, pp 42-44.

### Conferences and Conference Proceedings

Russell, T.H. and W.B. Roh. *Threshold of the Second Stokes Scattering in a Fiber Stimulated Brillouin Scattering Beam Combiner*. in *IEEE/LEOS Annual Meeting (LEOS-2001)*. 2001. La Jolla, San Diego, CA.

Russell, T.H. and W.B. Roh. *SBS Fiber Beam Combiner: the threshold of the second Stokes excitation*. in *Solid State and Diode Laser Technology Review*. 2001. Albuquerque, New Mexico.

Russell, T.H., W.B. Roh, and J.R. Marciante. *Incoherent Laser Beam Combining via Stimulated Brillouin Scattering in Multi-mode Fibers*. in *IEEE/LEOS Annual Meeting (LEOS-2000)*. 2000. Rio Grande, Puerto Rico.

Russell, T.H., W.B. Roh, and J.R. Marciante. *Incoherent laser beam combining using stimulated Brillouin scattering in multimode fibers*. in *Solid State and Diode Laser Technology Review*. 2000. Albuquerque, New Mexico.

Rodgers, B.C., T.H. Russell, and W.B. Roh. *Coherent and Incoherent Beam Combining and Cleanup via Stimulated Brillouin Scattering in Multi-mode fiber*. in *CLEO-Pacific Rim '99*. 1999. Seoul, Korea.

### Future Publication Titles

“Threshold of the second-order Stokes stimulated Brillouin scattering in optical fiber.”

“Intensity Scaling Using Fiber Based Raman Beam Cleanup.”

*Abstract*

The influence of stimulated scattering on laser intensity in fiber optic waveguides is examined. Stimulated Brillouin scattering (SBS) in long, multimode optical waveguides is found to generate a Stokes beam that propagates in the fiber LP<sub>01</sub> mode. This characteristic of the Stokes beam was first applied to beam cleanup, where an aberrated pump generated a Gaussian-like Stokes beam.

Additionally, the same process is found to combine multiple laser beams into a single spatially coherent source. The mean square difference between the two beams was used to measure the degree of spatial overlap, demonstrating spatial coherence between the Stokes beams even when the pump beams are not spatially correlated. This result is obtained regardless of whether the pump beams are at the same or different frequencies, producing two temporally coherent or incoherent Stokes beams respectively.

Limitations in beam cleanup and combining are also examined to identify ways to overcome them. Output couplers are designed that could be used to spatially filter the Stokes beam from the pump, thus increasing the number of beams that could be combined. The combined power restriction induced by second order Stokes threshold is examined experimentally and theoretically and is not found to be a significant limitation. Finally, stimulated Raman scattering (SRS) beam cleanup, which would relax the stringent spectral requirements on the pump beams, was also investigated.

The last portion of the dissertation theoretically examines suppression of stimulated Raman scattering in fibers to eliminate the restriction this imposes on the power of a fiber

laser or amplifier. The suppression was modeled using both a holmium dopant and adding a long period grating to the fiber. Both methods were shown to have a significant effect on the SRS threshold.

# LASER INTENSITY SCALING THROUGH STIMULATED SCATTERING IN OPTICAL FIBERS

## *1. Introduction*

### 1.1. Motivation

The department of defense has identified laser systems as critical to the modern military [1]. They are used for numerous applications including detection, targeting, laser radar, remote sensing, munitions guidance, and even as weapons in their own right. To be effective most of these applications require high intensity illumination of the target. In laser radar, for example, a laser pulse is sent from the sensor to a target. The sensor then images the scattered light and measures the time of flight of the light pulse to collect a 3-D image of the target. Since an aberrated laser beam diverges faster than a Gaussian beam, any laser aberrations reduce image resolution and lower the intensity on target, limiting the sensor operational range. For these reasons, great care is taken to ensure high quality laser beams are used. Unfortunately, high power solid lasers tend to be highly aberrated [2], thus novel concepts must be developed to improve the beam quality of high power systems.

Stimulated Brillouin scattering (SBS) in long optical fibers is one way to generate a high quality laser beam. This method has many benefits including a low threshold, a high operational dynamic range, its simplicity, and its scalability to multiple laser beams.

A low threshold is critical. The threshold represents light that is lost and the higher the threshold, the lower the overall efficiency of the system. SBS is typically one of the first nonlinear processes to appear in fibers. Silica fibers do not have a high third order nonlinear coefficient, but the guiding nature of the fiber allows for extremely long interaction lengths resulting in very low thresholds [3].

Several factors can limit the dynamic range of an SBS system. One of these is the second order threshold. This is the power level at which the beam generated through SBS (Stokes beam) is strong enough to excite a second Stokes beam. The reasons stated above may lead one to deduce that the second order threshold will be very low. Fortunately, however, the first order Stokes beam grows nearly exponentially in the fiber. Thus, there is only a strong interaction near the front end of the fiber, resulting in a short interaction length and a high second order threshold. For this reason, the second order Stokes threshold is not a significant limiting factor in the generation of a high-power, high-quality beam.

The simplicity with which SBS can generate a high-quality beam is one of its greatest advantages. It only requires that the aberrated beam be coupled into a long optical fiber. The resulting Stokes beam will be Gaussian-like regardless of any fluctuations in the transverse mode distribution of the source. Methods to produce a high quality beam through phase conjugation can be more difficult to implement since phase conjugation merely allows one to recreate the source transverse profile after traveling through an aberrating medium [4-8]. If the source is not diffraction limited, the phase conjugate beam will not be diffraction limited.

Finally, the generation of a Gaussian-like beam from an aberrated source through SBS is easily expandable to combine multiple lasers. Multiple sources at the same frequency merely appear as a highly aberrated beam coupled into the fiber and combine to form a single, high-power, Gaussian beam [9]. Multiple sources at different frequencies independently generate Stokes beams, each having nearly identical Gaussian profiles.

Fiber lasers offer a second method to generate a Gaussian-like beam. Unlike their bulk counterparts, the confinement of the light in a single-mode core guarantees high spatial quality output over a wide power range [10]. Because they have long interaction lengths and low losses, fiber lasers can have very low thresholds. Often, the fiber ends are used as the cavity mirrors, thus fiber laser devices have potential for excellent mechanical stability. In addition, the small cross section can reduce thermal loading on the fiber [11], eliminating much of the need for cooling.

Unfortunately, nonlinear effects can be devastating for fiber lasers. Although most fiber lasers have a wide spectral bandwidth, which eliminates SBS as a power-limiting factor, stimulated Raman scattering (SRS) becomes a problem with relatively modest average powers in pulsed laser systems. SRS increases the wavelength of the source as well as heats up the fiber. At higher laser powers, eliminating or reducing SRS becomes increasingly important.

## 1.2. Overview

The main objective of this dissertation research was to investigate methods to increase laser intensity through the manipulation of stimulated scattering. The research

was broken into two parts. The first was beam cleanup in optical fibers. Beam cleanup is the process described above where stimulated Brillouin scattering converts an aberrated input pump beam into a Gaussian-like output Stokes beam. The second phase of the research was aimed at reducing stimulated Raman scattering in fiber lasers.

The investigation into beam cleanup began experimentally. A laser beam was aberrated with an etched glass plate and coupled into a fiber. The fiber output was monitored to determine how well it fit a Gaussian as well as to determine its polarization properties and measure the efficiency of the cleanup process. This was followed by an attempt to reduce threshold by feeding a portion of the Stokes output back into the fiber and again measuring the ability of the fiber to clean the pump beam.

The study continued with an investigation into beam combining. Essentially this is the simultaneous cleanup of two pump beams in a single fiber. Experiments showed that two pump beams generated a spatially coherent Stokes beam regardless of the spatial or spectral characteristics of the pump beams.

The experimental exploration of beam cleanup and beam combining was completed with an investigation into some of their limitations. In this segment, ideas are presented that would enable beam combining of more than the two sources as well as an increased collection efficiency of the scattered radiation. Additionally, the second order threshold was measured to determine the useful power range for beam combining or cleanup. Finally, the possibility of using stimulated Raman scattering instead of stimulated Brillouin scattering was investigated in the hope that the requirements on the spectral quality of the laser beam could be relaxed.

A theoretical analysis mirrored the experimental research. The process of beam cleanup was modeled through an investigation of the relative gain experienced by different fiber modes for a given pump beam transverse spatial distribution. This sheds light upon the physical mechanism responsible for beam cleanup and demonstrated some limitations to beam cleanup that could not be demonstrated experimentally. Furthermore, an unexpected polarization property of the Stokes beams formed through beam cleanup and beam combining was explained theoretically. Finally, the second order threshold for stimulated Brillouin scattering was modeled allowing for an estimated threshold under circumstances other than those of the experiment and leading to a method to increase the second order threshold to more than 80 W.

The second phase of the research was designed to reduce stimulated Raman scattering in fiber lasers. Two methods were proposed to limit the growth of the Stokes beam. First, absorb the Stokes beam with an intercavity dopant. Second, couple the Stokes beam out of the fiber using a long period grating.

The investigation into an intra-cavity dopant to increase SRS threshold was completed theoretically. The dopant, holmium, was chosen based upon the existence of a strong absorption near the Stokes frequency and little absorption near the laser frequency. The absorption curve of holmium in a silicate glass window was measured using an FTIR spectrometer. The expected Stokes threshold was then modeled as a function of the dopant level in a single-pass geometry.

Long period gratings (LPGs) are similar to Bragg gratings in that they are periodic structures created in a photosensitive fiber. The result, however, is that instead of a

spectrally narrow reflection ( $\sim 1$  nm), the grading couples light from core-guided fiber modes into cladding-guided modes. The cladding modes of a fiber are typically very lossy so the light in these modes is rapidly attenuated and does not contribute to the exponential growth of the Stokes beam. The investigation into this began by measuring the Raman gain curve of the fiber, then designing an appropriate LPG to eliminate the Stokes beam from the fiber. The SRS threshold was then theoretically modeled to determine the effect the LPG had.

### **1.3. Document Organization**

The research presented throughout this document is original. Some of the significant accomplishments are:

1. SBS Beam cleanup in a 50-micron, multimode, graded-index fiber.
2. SBS Coherent beam combining in a 50-micron, multimode, graded-index fiber with two independent laser sources.
3. SBS Incoherent beam combining in an 8.2-micron, multimode, step-index fiber.
4. SBS second order Stokes modeling to include second order Stokes seeding by four-wave mixing.
5. SRS beam cleanup in a 50-micron, multimode, graded-index fiber.
6. Modeling of SRS suppression using an intercavity holmium dopant in a silicate fiber.
7. Modeling of SRS suppression using a long period grating in a germanium enriched fiber.

These research efforts are explained in detail after the introductory background found in Chapters 2 and 3. These two chapters outline the tools required for the rest of the dissertation. Chapter 4 describes the experimental and theoretical research into stimulated Brillouin scattering beam cleanup. Beam combining is thoroughly examined

in Chapter 5. The limitations to beam combining and beam cleanup are investigated in Chapter 6. Chapters 7 and 8 describe the experiments designed to modify the threshold of SRS in optical fibers using an intercavity dopant or long period grating respectively. Final conclusions are made in Chapter 9.

## **2. Propagation of Light in Optical Fibers**

### **2.1. Core Guided Fiber Modes**

When an electromagnetic field travels through an optical fiber, it is constrained by boundary conditions at the core-cladding interface. Only special field distributions meet these boundary conditions and can propagate efficiently through a fiber. These field distributions, called optical modes, form the basis of much of the research that is presented in this dissertation. An understanding of their origin and characteristics is critical to the remaining chapters. This chapter presents the derivation of the optical modes that propagate in step-index optical fibers. Similar derivations are found in most texts about optical waveguides [12, 13]. While graded-index fibers are also used in the experiments described in this document, the derivation of the modes is not described here.

The optical fibers used in the experiments described in this dissertation are made of doped SiO<sub>2</sub>, a dielectric material that is nonmagnetic and has no free charges or currents. In this fiber, Maxwell's equations and the constitutive relations reduce to

$$\nabla \times \vec{E} = -\frac{\partial \vec{B}}{\partial t} \quad (2.1)$$

$$\nabla \times \vec{B} = \mu_0 \frac{\partial \vec{D}}{\partial t} \quad (2.2)$$

$$\nabla \cdot \vec{D} = 0 \quad (2.3)$$

$$\nabla \cdot \vec{B} = 0 \quad (2.4)$$

$$\bar{D} = \epsilon_0 \bar{E} + \bar{P} \quad (2.5)$$

In order to decouple the equations for the magnetic and electric fields, take the curl of Equation (2.1) and substitute Equation (2.2) in the right hand side. Apply the identity

$$\nabla x \nabla x \bar{E} = \nabla (\nabla \cdot \bar{E}) - \nabla^2 \bar{E} \quad (2.6)$$

and use Equation (2.5) for the final result of

$$\nabla^2 \bar{E} - \mu_0 \frac{\partial^2}{\partial t^2} (\epsilon_0 \bar{E} + \bar{P}) = 0. \quad (2.7)$$

The bulk of this paper will describe the effects of the nonlinear aspect of the fiber optic waveguide, but in order to analytically calculate the electric field associated with different fiber modes, it is necessary to assume the fiber is linear and isotropic. This assumption allows Equation (2.7) to be simplified to

$$\nabla^2 \bar{E} - \left( \frac{n}{c} \right)^2 \frac{\partial^2}{\partial t^2} \bar{E} = 0. \quad (2.8)$$

We are looking for solutions that propagate along the fiber axis, thus we can assume a solution to the electric field that has the form:

$$\bar{E} = E_r(r) E_\theta(\theta) \exp[i(k_g z - \omega t)] \hat{e} \quad (2.9)$$

where  $k_g$  is the guided wavenumber. In cylindrical coordinates Equation (2.8) becomes

$$\frac{r}{E_r(r)} \frac{\partial}{\partial r} \left( r \frac{\partial}{\partial r} E_r(r) \right) + \frac{1}{E_\theta(\theta)} \frac{\partial^2}{\partial \theta^2} E_\theta(\theta) = \left( k_g^2 - \left( \frac{n}{c} \omega \right)^2 \right) r^2. \quad (2.10)$$

This equation can be separated into a function of  $\theta$  alone and a function of  $r$  alone using a separation constant, the square of  $m$ . This results in an azimuthal field dependence given by  $E_\theta(\theta) = \exp[im\theta]$ . The boundary condition for this equation,  $E_\theta(\theta) = E_\theta(\theta + 2\pi)$ , forces  $m$  to be an integer.

The azimuthal and longitudinal equations are simple to solve, reflecting the fact that the fiber properties do not vary along these two axes. Along the radial direction, however, the fiber appears as a series of three steps. The core of the fiber is a perfect cylinder with a high index of refraction. The cladding covers the core and has a slightly lower index. A protective jacket typically surrounds the cladding. Each of these regions is critical in the solution to the radial equation.

For efficient propagation of light through the waveguide, it must be totally internally reflected at either the core-cladding interface or the cladding-jacket interface. If the total internal reflection occurs at the core-cladding interface, the light propagates in a core-guided mode. If the total internal reflection occurs at the cladding-jacket interface, the light propagates in a cladding-guided mode. It is convenient to initially solve for the core-guided modes, assuming that the cladding is infinite. With these solutions, the cladding-guided mode is easier to solve.

A core-guided mode is only possible if the light rays are incident upon the core-cladding interface at an angle greater than the critical angle,  $\sin(\theta_c) = \frac{n_{cladding}}{n_{core}}$ . This restricts the  $z$ -component of the wavevector to  $n_{cladding} \frac{\omega}{c} \leq k_g \leq n_{core} \frac{\omega}{c}$ . Therefore, the radial part of the function will be different depending on if it is solved in the core or in

the cladding. If  $a$  is the radius of the core and we define  $k_c$  and  $\gamma$  by

$$k_c^2 = \left(\frac{n_{core}}{c}\omega\right)^2 - k_g^2, \quad \gamma^2 = k_g^2 - \left(\frac{n_{cladding}}{c}\omega\right)^2, \text{ then the radial component of the field is}$$

$$\begin{aligned} r \frac{\partial}{\partial r} E_r(r) + r^2 \left( \frac{\partial^2}{\partial r^2} E_r(r) \right) + [r^2 k_c^2 - m^2] E_r(r) &= 0 \quad r < a \\ r \frac{\partial}{\partial r} E_r(r) + r^2 \left( \frac{\partial^2}{\partial r^2} E_r(r) \right) - [r^2 \gamma^2 + m^2] E_r(r) &= 0 \quad r > a \end{aligned} . \quad (2.11)$$

The equations describing the field amplitude in the fiber core and cladding are Bessel's equation and the modified Bessel equation respectively. The solutions are given in [14] and consist of a linear combination of Bessel functions, Weber functions, and modified Bessel functions. By forcing the field amplitude to remain finite at both  $r = 0$  and  $r = \infty$ , the solution is simplifies to:

$$E_r(r) = \begin{cases} C_m J_m(k_c r) & r < a \\ D_m K_m(\gamma r) & r > a \end{cases} \quad (2.12)$$

where  $J_m$ , and  $K_m$  are the  $m^{\text{th}}$  order Bessel functions and modified Bessel functions respectively and  $C_m$  and  $D_m$  are constants controlling the power in the  $m^{\text{th}}$  fiber mode.

The radial components of the electric displacement and magnetic induction must be continuous across the core-cladding interface to satisfy the boundary condition. A considerable simplification can be made in weakly guiding fibers such that

$n_{core} - n_{cladding} \ll 1$ . In this approximation, the boundary conditions can be rephrased as

$$E_r(r)|_{r=a^-} = E_r(r)|_{r=a^+} \text{ and } \left. \frac{\partial E_r(r)}{\partial r} \right|_{r=a^-} = \left. \frac{\partial E_r(r)}{\partial r} \right|_{r=a^+}. \text{ This approximation will result in}$$

linearly polarized fiber modes [15]. These boundary conditions require that

$D_m = C_m \frac{J_m(k_c a)}{K_m(\gamma a)}$  and give rise to the dispersion relation

$$-ak_c \frac{J_{m-1}(k_c a)}{J_m(k_c a)} = \gamma \frac{K_{m-1}(\gamma a)}{K_m(\gamma a)}. \quad (2.13)$$

To simplify this equation, we define the fiber parameter, or  $V$  parameter.

$$V = \sqrt{(k_c a)^2 + (\gamma a)^2} = k_0 a \sqrt{n_{core}^2 - n_{cladding}^2} \quad (2.14)$$

For each fiber, this term is a constant at a given wavelength and is used to relate  $k_c$  to  $\gamma$ .

When the fiber parameter is used along with a short-hand notation,  $X = k_c a$ , Equation (2.13) becomes

$$-X \frac{J_{m-1}(X)}{J_m(X)} = \sqrt{V^2 - X^2} \frac{K_{m-1}(\sqrt{V^2 - X^2})}{K_m(\sqrt{V^2 - X^2})}. \quad (2.15)$$

For a given fiber parameter, each  $m$  results in several fiber modes. A sample is shown in Figure 1. This figure represents the right and left hand sides of Equation (2.15) when  $V = 5$ . As this figure shows, there are several intersections, each of which represents a mode of the waveguide. These modes are labeled by an integer representing the azimuthal dependence of the field,  $m$ , and an integer that represents which intersection is to be used (a one represents the intersection closest to  $X = 0$ ). The second number is a measure of the number of zeros in the radial field distribution. The intensity patterns of the modes represented by Figure 1 are shown in Figure 2.

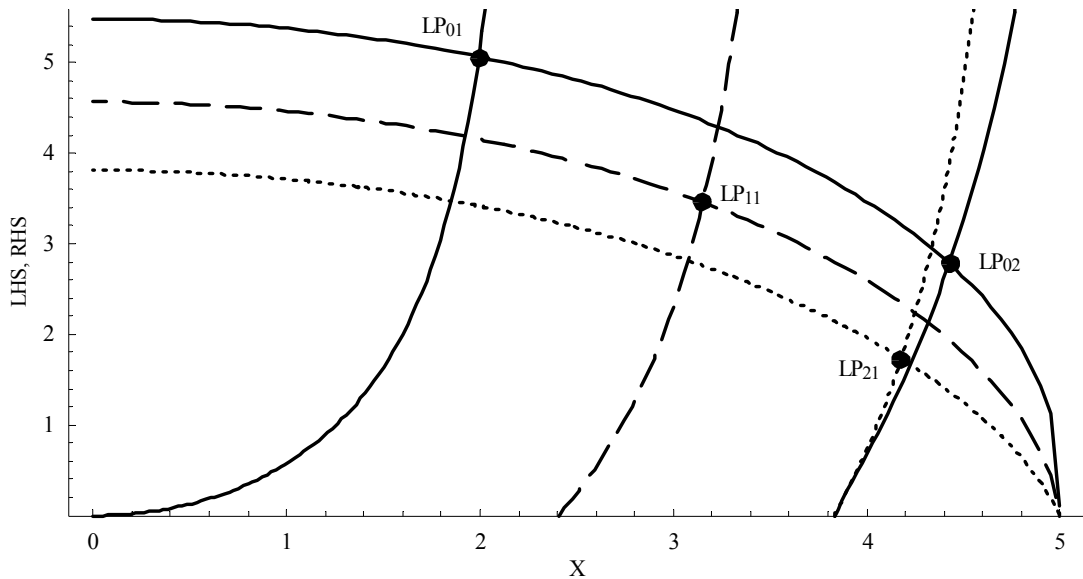


Figure 1: Normalized propagation constant for the modes of a fiber optic waveguide, with  $V = 5$ .

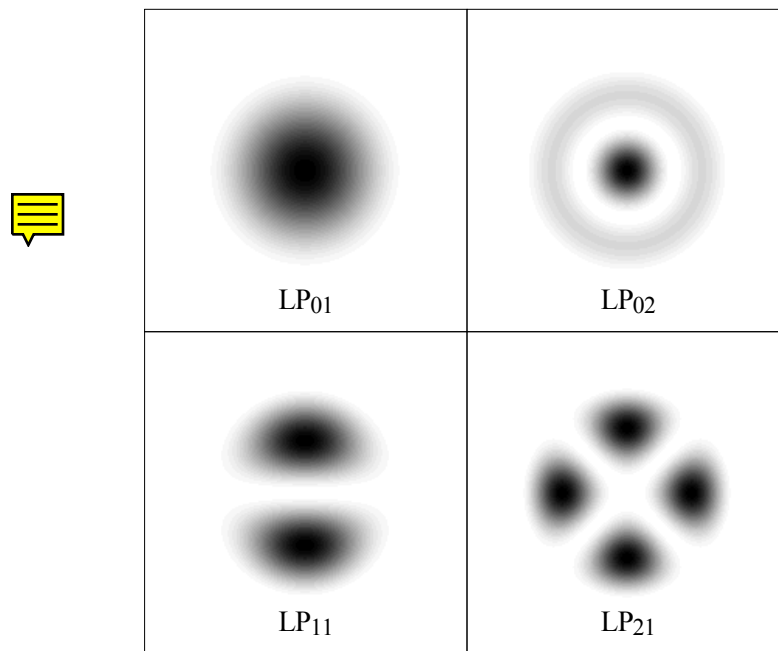


Figure 2: The first four transverse mode patterns of a fiber optic waveguide.

When light travels in a pure fiber mode, the cross sectional intensity distribution in the fiber is constant along the length of the fiber. On the other hand, if the light travels in a linear combination of modes, beating between the modes leads to a changing intensity



distribution along the length of the fiber. To illustrate this point, Figure 3 shows the electric field distribution of the pure LP<sub>01</sub> and LP<sub>11</sub> modes (a and b respectively) along with the transverse intensity distribution of the superposition of the two modes (c) at the front end of a representative 50-micron fiber. Half the beat length further down the fiber,  $\pi/(k_{c01} - k_{c11})$ , the relative phases between the two modes will shift by 180 degrees. Figure 3(d-f) represents this case. The peak intensity within the fiber has moved from the right side of the fiber to the left.

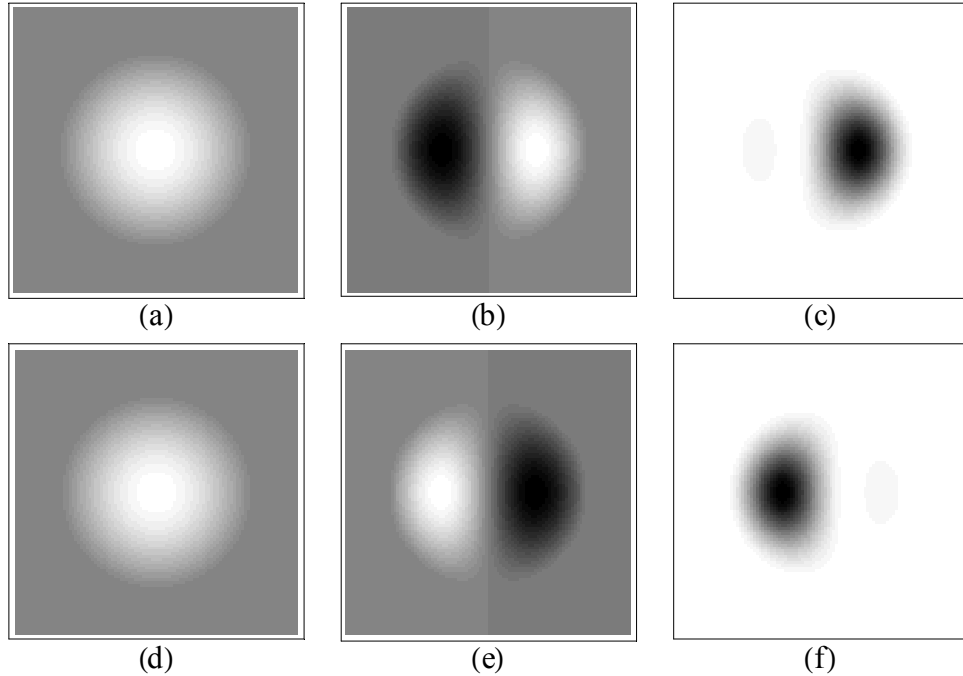


Figure 3: (a,b) The transverse electric field pattern of the LP<sub>01</sub> and LP<sub>11</sub> modes at the front end of a representative 50 micron fiber. (c) The intensity distribution due to a superposition of the modes in (a,b). (d,e) The transverse electric field pattern of the LP<sub>01</sub> and LP<sub>11</sub> modes at a distance of  $\pi/(k_{c01} - k_{c11})$  into the fiber. (f) The intensity distribution due to a superposition of the modes in (d,e).

The V parameter, Equation (2.14), is not only important in determining the intensity distribution of the modes, it is also critical in determining the number of modes that can



propagate down the fiber. In the above example, four different mode patterns are supported. Each of these patterns results from at least two, and more commonly four, orthogonal polarization modes. Thus in the above example, 12 modes are supported by the fiber, two polarization modes in each of the LP<sub>01</sub> and LP<sub>02</sub> modes and four in each of the LP<sub>11</sub> and LP<sub>21</sub> modes.

Short of using a graph such as Figure 1, there is no exact method to calculate the number of modes supported by the fiber, yet it is very important to know what modes are supported. This is the only way to ensure that, if one is transmitting light, the energy can be carried by the fiber or, if one is generating light, the output pattern is acceptable. Two limits are described here. First is the case where only a single mode is desired. As shown in Figure 1, for all values of  $n$ , the right hand side of Equation (2.15) terminates when  $X = V$ . Therefore, when  $V < 2.405$ , Equation (2.15) will only be satisfied for one value of  $X$ . Although there are two orthogonal polarization modes associated with this value of  $X$ , the fiber is considered single mode since only the fundamental Gaussian-like LP<sub>01</sub> intensity distribution is supported.

The opposite extreme, when  $V$  is large, is also significant and the number of modes that can propagate in a fiber can be approximated as described below. In this limit, the left hand side of Equation (2.15) can be approximated as shown in Equation (2.16) [14].

$$\sqrt{\frac{8X}{\pi}} \frac{\sin\left(X - \frac{\pi}{4}(1+2m)\right)}{J_m(X)} \quad (2.16)$$

This function is zero when  $X - \frac{\pi}{4}(1 + 2m) = n\pi$  where n is any integer and each of these zeros can be associated with a mode pattern as long as the right hand side of Equation (2.15) is real. So by counting the number of zeros between  $X = 0$  and  $X = V$ , the number of allowed modes for any given m can be estimated. Then allowing for different polarizations for each m and summing over  $m$ , the number of modes is [13]

$$N \approx \frac{4}{\pi^2} V^2. \quad (2.17)$$

This number is critical in the demonstration of beam cleanup. If the number of supported modes is small, a beam will be spatially filtered before entering the fiber. Thus beam cleanup using stimulated scattering cannot be investigated. Only when a large number of modes are supported by the fiber can beam cleanup be attributed with confidence to stimulated scattering.

## 2.2. Cladding-Guided Fiber Modes

In the above analysis, we assumed an infinite cladding, but it was also mentioned that modes guided by the cladding-jacket interface could also propagate in the fiber. This will only occur if there is total internal reflection at the cladding-jacket border. Physically, this requirement on the propagation constant is

$$n_{jacket} \frac{\omega}{c} \leq k_{gcl} \leq n_{cladding} \frac{\omega}{c}. \quad (2.18)$$

The solution to the electric field intensities is found using the same method as described for the core-guided modes with the exception that the radial portion of Equation (2.10) is solved using boundary conditions at the core-cladding and at the cladding-jacket

interface. Because the index step between the cladding and the jacket is relatively large, the LP mode approximation cannot be used and the more exact forms for the fields, the HE and EH modes, must be used. This leads to a dispersion relation that is much more complicated than the infinite cladding case. Erdogan derived the form of the dispersion relation, the final result of which is given in Appendix A [12, 16]. The right and left hand sides of the equation are plotted below.

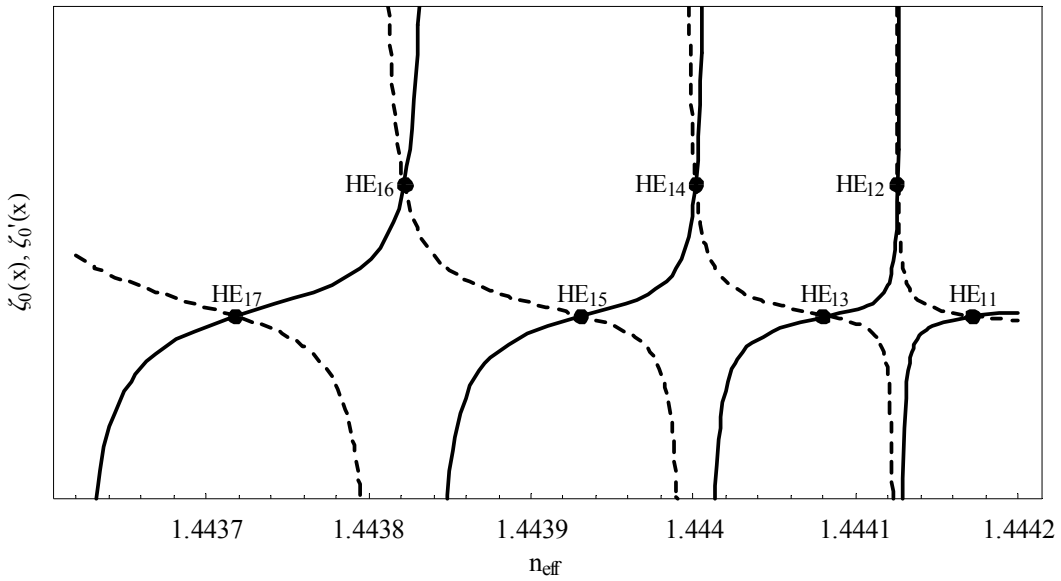


Figure 4: Cladding mode dispersion relation.

The cladding-mode intensity distributions are calculated from the effective indices in the same way that the core-guided intensity distributions were found (see Appendix A). Figure 5 shows the first three circularly symmetric cladding modes. The lowest order core-guided mode is shown for comparison.



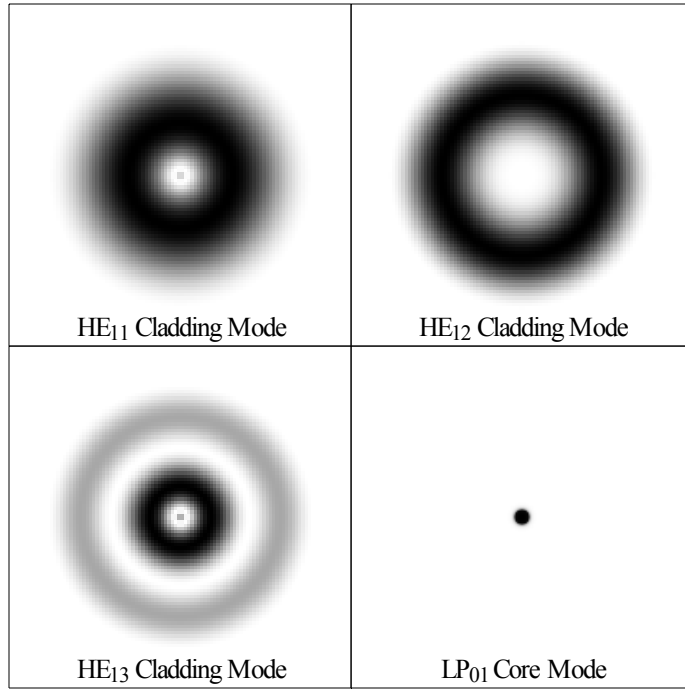


Figure 5: (Top and Bottom Left) Cladding mode intensity distributions. Odd modes have a local maximum centered in the fiber core. Even modes have a local minimum in the fiber core. (Bottom Right) The lowest order core guided mode.



### 3. Stimulated Scattering in Optical Fibers

Equation (2.8) of the preceding chapter neglects the contribution of the nonlinear electric susceptibility to the electric field. This simplification is valid for low electric field strengths, but it is not in the realm of interest for the rest of this dissertation. In situations where the incident light is intense enough, stimulated scattering is observed. Stimulated scattering is a nonlinear effect in which the energy in a pump photon is redistributed such that a lower energy photon and a phonon are emitted. The origin of this effect is examined in this chapter along with critical features that will be applied to different situations throughout the rest of this document.

Equation (2.7) provides a starting point to derive the equations governing the coupling between the pump and Stokes beams. The polarization term in this equation can be accounted for by expanding it in a power series of the electric field

$$\bar{P} = \epsilon_0 \left( \chi^{(1)} \cdot \bar{E} + \chi^{(2)} : \bar{E} \bar{E} + \chi^{(3)} : : \bar{E} \bar{E} \bar{E} + \dots \right) \quad (3.1)$$

where  $\epsilon_0$  is the permittivity of free space and the symbols  $\cdot$ ,  $:$ ,  $: :$  represent the product between the susceptibility tensor and the electric field (e.g. the  $i^{\text{th}}$  component of the product between the third order susceptibility and the electric field is given by

$$(\chi^{(3)} : : \bar{E} \bar{E} \bar{E})_i = \sum_{j,k,l} \chi_{i,j,k,l}^{(3)} E_j E_k E_l .$$

The third order nonlinear susceptibility,  $\chi^{(3)}$ , is responsible for stimulated scattering. Although higher order terms exist, under the conditions examined in this document, they are negligible. Thus the series can be truncated after the terms shown in Equation (3.1).

The expansion coefficients  $\chi^{(1)}$ ,  $\chi^{(2)}$ , and  $\chi^{(3)}$  are 1<sup>st</sup>, 2<sup>nd</sup>, and 3<sup>rd</sup> order frequency dependent susceptibility tensors, respectively.

In an isotropic material such as glass, any rotation or inversion of the material should result in the same polarization response. Application of this requirement to the nonlinear susceptibility reduces  $\chi^{(1)}$  to a scalar, requires  $\chi^{(2)}$  to be identically zero, and reduces the 81 elements that make up the 4<sup>th</sup> rank tensor  $\chi^{(3)}$  to 3 independent elements [17]

$$\begin{aligned}\chi^{(3)}_{xxxx} &= \chi^{(3)}_{yyyy} = \chi^{(3)}_{zzzz} = \chi^{(3)}_{xxyy} + \chi^{(3)}_{xyxy} + \chi^{(3)}_{xyyx} \\ \chi^{(3)}_{yyzz} &= \chi^{(3)}_{zzyy} = \chi^{(3)}_{zzxx} = \chi^{(3)}_{xxzz} = \chi^{(3)}_{xxyy} = \chi^{(3)}_{yyxx} \\ \chi^{(3)}_{yzyz} &= \chi^{(3)}_{zyzy} = \chi^{(3)}_{zxzx} = \chi^{(3)}_{xzxz} = \chi^{(3)}_{xyxy} = \chi^{(3)}_{yxyx} \\ \chi^{(3)}_{yzyy} &= \chi^{(3)}_{zyyz} = \chi^{(3)}_{zxzx} = \chi^{(3)}_{xzxz} = \chi^{(3)}_{xyyx} = \chi^{(3)}_{yxyy}\end{aligned}\quad (3.2)$$

Thus in fiber optic waveguides made of SiO<sub>2</sub>, the wave equation becomes

$$\nabla^2 \vec{E} - \mu_0 \epsilon_0 \frac{\partial^2}{\partial t^2} \left( (1 + \chi^{(1)}) \vec{E} + \chi^{(3)} : \vec{E} \vec{E} \vec{E} \right). \quad (3.3)$$

Since we are looking for the interaction of a pump beam and the Stokes beam, the electric field can be represented by

$$\vec{E} = \hat{e}_p A_p(z) \exp \left[ i(k_p z - \omega_p t) \right] + \hat{e}_s A_s(z) \exp \left[ i(\pm k_s z - \omega_s t) \right] + c.c. \quad (3.4)$$

where c.c. represents the complex conjugate of the previous terms,  $k_p$  ( $k_s$ ) is the wavenumber of the pump (Stokes) field,  $\omega_p$  ( $\omega_s$ ) is the frequency of the pump (Stokes) field,  $A_p(z)$  ( $A_s(z)$ ) is the complex pump (Stokes) field amplitude, and  $\hat{e}_p$  ( $\hat{e}_s$ ) is the complex polarization unit vector of the pump (Stokes) field. The  $\pm$  before the wavevector in the Stokes term integrates the effect of the direction of the Stokes wave

into the equations. This representation of the electric field ignores all transverse (x and y) dependence of the field amplitude. The transverse term is associated with the fiber modes and has already been investigated in Chapter 2.

Equation (3.4) is a vector equation that describes the electric field in the fiber and its propagation down the fiber axis. However, the equation is difficult to work with in its current form. For the remainder of the derivation, a specific polarization of the field will be assumed, reducing the above to a scalar equation.

The wave equation contains the third power of the electric field which, when expanded, results in many terms. In order for the equation to hold at all times, the terms that oscillate at like frequencies can be set equal to each other. The terms of interest in stimulated Raman scattering are those that oscillate at  $\omega_p$  and  $\omega_s$ . These terms result in the equation shown below.

$$\nabla^2 \left[ A_{p,s}(z) \exp \left[ i(k_{p,\pm s} z - \omega_{p,s} t) \right] \right] - \mu_0 \epsilon_0 \frac{\partial^2}{\partial t^2} \left\{ A_{p,s}(z) \exp \left[ i(k_{p,\pm s} z - \omega_{p,s} t) \right] [1 + \chi^{(1)}(\omega_{p,s}) + 3\chi^{(3)}(\omega_{p,s}, -\omega_{p,s}, \omega_{p,s}) |A_{p,s}|^2 + 6\chi^{(3)}(\omega_{s,p}, -\omega_{s,p}, \omega_{p,s}) |A_{s,p}|^2] \right\} \quad (3.5)$$

Another term taking four-wave mixing into account must be added to this equation if the Stokes beam propagates in the same direction as the pump beam. While not critical to this derivation, it becomes very important when second order SBS is analyzed in Chapter 6.

Since the  $x$ - and  $y$ -variation in the electric field was ignored, the Laplacian operator reduces to the second derivative with respect to  $z$ . In nearly all applicable situations, the variation in the amplitude of the electric field will be small in comparison to the variation

of the exponential portion of the field. Assuming that  $\left| \frac{\partial^2}{\partial z^2} A(z) \right| \ll \left| k \frac{\partial}{\partial z} A(z) \right|$ , evaluating the Laplacian, the time derivative, and canceling the exponent on both sides results in

$$2ik_{p,\pm s} \frac{\partial A_{p,s}}{\partial z} - A_{p,s} k_{p,\pm s}^2 + \mu_0 \epsilon_0 \omega_{p,s}^2 A_{p,s} \left\{ 1 + \chi^{(1)}(\omega_{p,s}) + \dots + 3\chi^{(3)}(\omega_{s,p}, -\omega_{s,p}, \omega_{p,s}) |A_{p,s}|^2 + 6\chi^{(3)}(\omega_{s,p}, -\omega_{s,p}, \omega_{p,s}) |A_{s,p}|^2 \right\} = 0. \quad (3.6)$$

The functional form of the third order nonlinear susceptibility is such that the magnitude of  $\chi^{(3)}(\omega_{s,p}, -\omega_{s,p}, \omega_{p,s})$  will be greatest when there is an excited energy level that is precisely  $\hbar(\omega_p - \omega_s)$  above the ground state. Likewise, there will be a resonance for  $\chi^{(3)}(\omega_{p,s}, -\omega_{p,s}, \omega_{p,s})$  (the susceptibility associated with two-photon absorption [17]), when there is an energy level that is exactly  $2\hbar\omega_{p,s}$  above the ground state. We have specifically chosen  $\omega_s$  such that the first condition is true (in silica fibers this corresponds to a frequency separation of about 13.2 THz for SRS and 16 GHz for SBS), thus it is unlikely that the second condition will also hold. The two-photon absorption term will therefore be negligible compared to the stimulated Raman scattering term. To further simplify the equation, multiply Equation (3.6) by  $-iA_{p,s}^*$  and add the complex conjugate of the resulting equation. Noting that  $\frac{\partial |A_{p,s}|^2}{\partial z} = A_{p,s}^* \frac{\partial A_{p,s}}{\partial z} + A_{p,s} \frac{\partial A_{p,s}^*}{\partial z}$ , this yields:

$$k_{p,\pm s} \frac{\partial |A_{p,s}|^2}{\partial z} + \frac{\omega_{p,s}^2 |A_{p,s}|^2}{c^2} \left\{ \text{Im} \left[ \chi^{(1)}(\omega_{p,s}) \right] + 6 \text{Im} \left[ \chi^{(3)}(\omega_{s,p}, -\omega_{s,p}, \omega_{p,s}) \right] |A_{s,p}|^2 \right\} = 0. \quad (3.7)$$

Finally it should be noted that the imaginary part of the linear susceptibility is responsible for absorption [3]. The gain coefficient,  $g$ , is due to the imaginary part of the third order susceptibility [17], the intensity of the pump and Stokes beams is proportional to the amplitude of the E-field squared, and the imaginary part of the third order susceptibility is an odd function of detuning between the frequency components [17].

$$\alpha_{p,s} = \frac{\omega_{p,s}}{n_{p,s}c} \text{Im} \left[ \chi^{(1)}(\omega_{p,s}) \right] \quad (3.8)$$

$$g = -\frac{3\omega_s}{\epsilon_0 c^2 n_s n_p} \text{Im} \left[ \chi^{(3)}(\omega_p, -\omega_p, \omega_s) \right] \quad (3.9)$$

$$I_{p,s} = 2\epsilon_0 c n_{p,s} |A_{p,s}|^2 \quad (3.10)$$

$$\text{Im} \left[ \chi^{(3)}(\omega_p, -\omega_p, \omega_s) \right] = -\text{Im} \left[ \chi^{(3)}(\omega_s, -\omega_s, \omega_p) \right] \quad (3.11)$$

Where  $\alpha$  is the absorption coefficient, and  $I_{p,s}$  is the intensity of the pump or Stokes beam. Thus the intensity of the Stokes beam in a fiber is given by the following set of coupled equations [3]

$$\begin{aligned} \frac{\partial I_s}{\partial z} &= \pm \left( g I_p I_s - \alpha_s I_s \right) \\ \frac{\partial I_p}{\partial z} &= -\frac{\omega_p}{\omega_s} g I_p I_s - \alpha_p I_p \end{aligned} . \quad (3.12)$$

Near threshold, when the pump power is much greater than the Stokes power, it can be assumed that there is no pump depletion due to stimulated scattering. While this violates the law of conservation of energy, it allows for an analytical solution to the

above system of equations. Under this approximation, the solution for the intensity of the Stokes beam as a function of  $z$  is

$$I_s(z) = I_{s0} \exp \left\{ \pm \left( g_r I_{p0} \frac{1}{\alpha_p} [1 - \exp(-\alpha_p z)] - \alpha_s z \right) \right\}. \quad (3.13)$$

where  $I_{s0}$  is the intensity of the Stokes beam incident on the fiber face. If the Stokes beam is traveling in the opposite direction as the pump beam, then  $I_{s0}$  is the intensity incident upon the rear face of the fiber. If the Stokes beam is propagating in the same direction as the pump beam, then  $I_{s0}$  is the intensity incident upon the front face of the fiber. The direction of the traveling beam is chosen by the selection of either the plus or minus in the equation for the Stokes intensity. The plus corresponds to a wave traveling in the same direction as the pump beam.

This result demonstrates the obvious complication that SRS can impose on a laser system. The exponential increase in Stokes power will quickly deplete the energy in the pump and significantly reduce the laser efficiency. By their nature, the cavity of a laser system will have extremely high intensities, thus even when there is no injected Stokes beam, the spontaneous emission of light through blackbody radiation or spontaneous Raman scattering can be strong enough to start the stimulated scattering process and reduce the laser power significantly.

For stimulated Raman scattering to have a significant effect, the amount of power at the Stokes beam must be above threshold. Experimentally, the threshold is easily observed as a sharp knee in the Stokes output, above which, the Stokes power increases

linearly. Theoretically, it is much more difficult to identify the threshold criteria. Smith defines it as the pump power that predicts an equivalent Stokes output based upon the undepleted pump approximation of Equation (3.13) [18]. Although the no pump depletion approximation is obviously invalid at this point, the error is relatively small when estimating the threshold.

Based on Equation (3.13) the amount of Stokes power at the exit end of the fiber is directly proportional to the amount at the input end of the fiber. Typically, however, the Stokes power builds from noise. For long fiber lengths, when  $\alpha_s \approx \alpha_p$ , the noise can be modeled by injecting a fictitious photon at a certain location in the fiber [18]. For forward scattering, the photon should be injected at the front end,  $L = 0$ . For backward scattering processes, this photon should be injected at  $L = \frac{1}{\alpha_p} \ln(g_r I_p / \alpha_s)$ .

To calculate the total power in the Stokes beam, the Stokes power at every wavelength component must be integrated together. In the forward scattering case this integral becomes

$$P_s(L) = \int \left\{ \hbar \omega \exp \left[ g_r(\omega) \frac{P_p(0)}{A_{eff} \alpha_p} [1 - \exp(-\alpha_p L)] - \alpha_s L \right] \right\} d\omega, \quad (3.14)$$

where the integration is performed over the Raman gain bandwidth and the pump is assumed to be monochromatic.

In order to solve the above integral, it is necessary to have some knowledge of the functional form of the gain coefficient. The Raman gain spectrum will have a predominant peak associated with a vibrational state in the material. The spectrum is

typically a complicated function of the frequency difference as shown for SiO<sub>2</sub> in Figure 6. It would be extremely difficult to solve Equation (3.14) analytically if the exact form of the Raman gain was used.

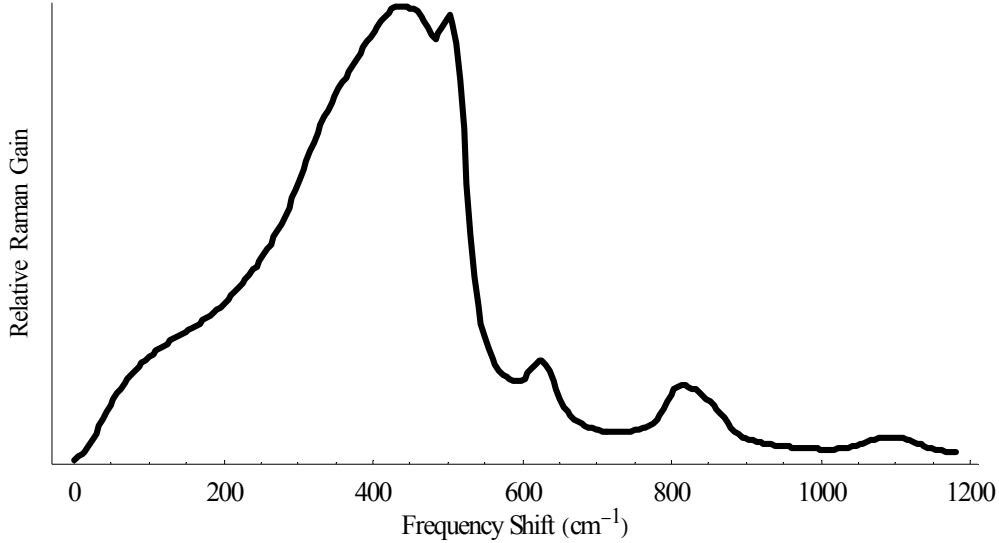


Figure 6: Raman gain spectrum [19]

Assuming a Lorentzian gain profile, equal absorption at the pump and Stokes wavelengths, and long fibers, the forward stimulated Raman scattering threshold is approximated by [17, 18, 20]:

$$P_{th} \approx 16 \frac{A_{eff}}{g_{r0} L_{eff}}. \quad (3.15)$$

Where  $L_{eff} = \frac{1}{\alpha_p} [1 - \exp(-\alpha_p L)]$  is the effective length of the fiber. The result for backward scattering is slightly different because the Stokes photon that is introduced to simulate spontaneous emission is not injected at the end of the fiber. For stimulated Raman scattering, the backward scattering threshold is approximately

$$P_{th} \approx 20 \frac{A_{eff}}{g_{r0} L_{eff}}. \quad (3.16)$$

From these two equations, it is apparent that forward stimulated Raman scattering will reach threshold before backward SRS and is much more likely to be the dominant effect.

Stimulated Brillouin scattering on the other hand is only possible in the backward direction. The threshold for this process is

$$P_{th} \approx 21 \frac{A_{eff}}{g_{r0} L_{eff}}. \quad (3.17)$$

These equations are approximate and can change under different conditions. If the absorption at the Stokes and pump wavelengths are different, the fiber is not long enough to force  $\alpha_p L \gg 1$ , or the effective length of the fiber is different at the Stokes wavelength and the pump wavelength, the derivation may break down. These situations will be investigated in the experiments described in Chapters 7 and 8.

## **4. SBS Beam Cleanup**

### **4.1. Background**

Recent scientific literature describes many methods to clean laser beams through stimulated Brillouin scattering. Typically, however, they refer to the process of eliminating the aberrating effects of an optical component such as an amplifier. In these experiments, after the beam travels through the aberrating element, it is phase conjugated using SBS and sent back through the aberrator [21]. This second pass removes the phase aberrations from the wavefront and the beam returns to its original shape.

Beam cleanup as discussed in this dissertation is significantly different in that it refers to exciting an  $LP_{01}$  fiber mode through SBS using an aberrated laser beam. The fundamental difference is that this method can clean any aberrated beam, whereas the phase conjugation experiments described above cannot clean the aberrations inherent to the laser.

The process of exciting low order fiber modes from aberrated sources through nonlinear processes is not a new concept. In 1981, Nesterova *et al.* showed that the transverse Stokes power in an optical fiber was redistributed through stimulated Raman scattering from the highly aberrated pump beam into low order fiber modes [22]. Similar results were reported by Baldeck *et al.* in 1987, when they noted that an aberrated pump produced a ring-like Stokes beam [23]. In 1988, Grundinin *et al.* found that solitons generated from SRS in multimode fibers propagated in the fundamental mode [24]. Furthermore, in 1992, Chiang noticed that when multiple Stokes modes were excited

through SRS in fiber waveguides, that subsequent higher order Stokes beams propagated in fewer optical modes than the previous one [25].

In 1993, Brusselbach reported similar effects using stimulated Brillouin scattering [26]. Later, Rodgers *et al.* showed how the process is useful for beam cleanup and beam combining [27]. Rodgers demonstrated SBS beam cleanup by transmitting a beam through a microscope slide etched in acid and efficiently cleaning the beam through stimulated Brillouin scattering in a multimode optical fiber.

This chapter further examines the phenomenon of stimulated Brillouin scattering beam cleanup. Section 4.2 studies the theoretical source of beam cleanup. Section 4.3 experimentally examines the properties of the Stokes beam. Conclusions are made in Section 4.4.

## 4.2. Theoretical Beam Cleanup

As described in Chapter 3, the interaction of the pump beam and the Stokes beam through stimulated Brillouin scattering lead to a set of coupled differential equations given by Equation (3.12). These are repeated here with the approximation that  $\omega_p / \omega_s \approx 1$  and explicitly stating the dependence of the intensity on  $z$  and the transverse dimensions  $r_\perp$ .

$$\begin{aligned} \frac{\partial I_s(r_\perp, z)}{\partial z} &= -g_B I_s(r_\perp, z) I_p(r_\perp, z) + \alpha_s I_s(r_\perp, z) \\ \frac{\partial I_p(r_\perp, z)}{\partial z} &= -g_B I_s(r_\perp, z) I_p(r_\perp, z) - \alpha_p I_p(r_\perp, z) \end{aligned} \quad (4.1)$$

Integrating Equations (4.1) over the transverse dimensions and letting

$P(z) = \int I(r_\perp, z) \partial r_\perp$  be the power flowing through the fiber at point  $z$  yields:

$$\begin{aligned} \frac{\partial P_s(z)}{\partial z} &= -g_{B_{eff}}(z) P_s(z) P_p(z) + \alpha_s P_s(z) \\ \frac{\partial P_p(z)}{\partial z} &= -g_{B_{eff}}(z) P_s(z) P_p(z) - \alpha_p P_p(z) \end{aligned} \quad (4.2)$$

$$g_{B_{eff}}(z) = g_B \frac{\int I_s(r_\perp, z) I_p(r_\perp, z) \partial r_\perp}{P_s(z) P_p(z)}. \quad (4.3)$$

Equation (4.3) defines the effective gain and clearly shows its dependence on the overlap of the Stokes and pump beams.

The pump and Stokes electric fields can be expanded in terms of the fiber modes described in Chapter 2. After a little algebra (see Appendix B), the effective Brillouin gain becomes

$$\begin{aligned} g_{B_{eff}}(z) &= \frac{g_B (4\epsilon_0 c n)^2}{P_s(z) P_p(z)} \left\{ \sum_{m,j} A_{sm,sq,pj,pj}(z) \gamma_{sm,sm,pj,pj} + \dots \right. \\ &\quad 2 \sum_{m,q < m, j} A_{sm,sq,pj,pj}(z) \gamma_{sm,sq,pj,pj} \cos(\Delta k_{smq} z + \Delta \phi_{smq}) + \dots \\ &\quad 2 \sum_{m,j,v < j} A_{sm,sm,pj,pv}(z) \gamma_{sm,sm,pj,pv} \cos(\Delta k_{pjv} z + \Delta \phi_{pjv}) + \dots \\ &\quad 2 \sum_{m,q < m, j, v < j} A_{sm,sq,pj,pv}(z) \gamma_{sm,sq,pj,pv} \cos((\Delta k_{pjv} - \Delta k_{smq}) z + (\Delta \phi_{pjv} - \Delta \phi_{smq})) + \dots \\ &\quad \left. 2 \sum_{m,q < m, j, v < j} A_{sm,sq,pj,pv}(z) \gamma_{sm,sq,pj,pv} \cos((\Delta k_{pjv} + \Delta k_{smq}) z + (\Delta \phi_{pjv} + \Delta \phi_{smq})) \right\} \end{aligned} \quad (4.4)$$

$$\begin{aligned}
\gamma_{sm,sq,pj,pv} &= \int \left\{ \psi_{sm}(r_\perp) \psi_{sq}(r_\perp) \psi_{pj}(r_\perp) \psi_{pv}(r_\perp) \right\} dr_\perp \\
A_{sm,sq,pj,pv}(z) &= A_{sm}(z) A_{sq}(z) A_{pj}(z) A_{pv}(z) \\
\Delta k_{pjv} &= k_{pcj} - k_{pcv} \\
\Delta k_{smq} &= k_{scm} - k_{scq} \\
\Delta \phi_{pjv} &= \phi_{pcj} - \phi_{pcv} \\
\Delta \phi_{smq} &= \phi_{scm} - \phi_{scq}
\end{aligned} \tag{4.5}$$

where the summations are over all fiber modes and the  $m^{\text{th}}$  mode has a transverse distribution,  $\psi_m(r_\perp)$ , an amplitude,  $A_m(z)$ , a propagation constant,  $k_{cm}$ , and a phase,  $\phi_m$ . Unfortunately, the  $z$ -dependence of the modal amplitude coefficients is dependent upon the effective Brillouin gain so Equation (4.4) does not immediately reveal the mode that will produce the greatest gain. If, however, it is assumed that all pump modes decay in the positive  $z$ -direction at the rate  $d_p(z)$ , and all Stokes modes decay in the positive  $z$ -direction at the rate,  $d_s(z)$ , the field amplitude can be written as a product of a constant and the decay function. This assumption is only valid for low pump powers, where the Stokes gain is minimal. Above threshold, experimental evidence shows that the Stokes LP<sub>01</sub> modal amplitude grows much faster than the others. This analysis, however, still conveys insight into the increased gain of the LP<sub>01</sub> mode over other intensity distributions. With this assumption the modal amplitude is written as

$A_{sm,sq,pj,pj}(z) = d_s(z)^2 d_p(z)^2 \mathcal{A}_{sm,sq,pj,pj}$  and the product of the Stokes and pump power becomes  $P_s(z) P_p(z) = d_s(z)^2 d_p(z)^2 P_s(0) P_p(0)$ . Substituting this into Equation (4.4) reduces all  $z$ -dependence in the gain to the cosine terms.

$$\begin{aligned}
g_{B_{eff}}(z) = & \frac{g_B (4\varepsilon_0 c n)^2}{P_s(0) P_p(0)} \left\{ \sum_{m,j} \mathcal{A}_{sm,sm,pj,pj} \gamma_{sm,sm,pj,pj} + \dots \right. \\
& 2 \sum_{m,q < m,j} \mathcal{A}_{sm,sq,pj,pj} \gamma_{sm,sq,pj,pj} \cos(\Delta k_{smq} z + \Delta \phi_{smq}) + \dots \\
& 2 \sum_{m,j,v < j} \mathcal{A}_{sm,sm,pj,pv} \gamma_{sm,sm,pj,pv} \cos(\Delta k_{pjv} z + \Delta \phi_{pjv}) + \dots \\
& 2 \sum_{m,q < m,j,v < j} \mathcal{A}_{sm,sq,pj,pv} \gamma_{sm,sq,pj,pv} \cos((\Delta k_{pjv} - \Delta k_{smq}) z + (\Delta \phi_{pjv} - \Delta \phi_{smq})) + \dots \\
& \left. 2 \sum_{m,q < m,j,v < j} \mathcal{A}_{sm,sq,pj,pv} \gamma_{sm,sq,pj,pv} \cos((\Delta k_{pjv} + \Delta k_{smq}) z + (\Delta \phi_{pjv} + \Delta \phi_{smq})) \right\}
\end{aligned} \tag{4.6}$$

Figure 7(a) is a plot of the effective gain along the length of a fiber when the pump and Stokes beams are made of LP<sub>01</sub> and LP<sub>11</sub> modes. The rapid oscillations are due to the terms in Equation (4.6) fluctuating at spatial frequencies of  $\Delta k$  or greater. These fluctuations will quickly average to zero leaving only the slowly oscillating terms of Equation (4.7).

$$\begin{aligned}
g_{B_{eff}}(z) = & \frac{g_B (4\varepsilon_0 c n)^2}{P_s(0) P_p(0)} \left\{ \sum_{m,j} \mathcal{A}_{sm,sm,pj,pj} \gamma_{sm,sm,pj,pj} + \dots \right. \\
& \left. 2 \sum_{m,q < m,j,v < j} \mathcal{A}_{sm,sq,pj,pv} \gamma_{sm,sq,pj,pv} \cos((\Delta k_{pjv} - \Delta k_{smq}) z + (\Delta \phi_{pjv} - \Delta \phi_{smq})) \right\}
\end{aligned} \tag{4.7}$$

This is plotted with a solid line in Figure 7(b). These slow oscillations in the gain are due to modal dispersion. As described in Chapter 2, the transverse power distribution in a fiber changes along the fiber axis (see Figure 2). Because these oscillations are frequency dependent, if the pump and Stokes beams overlap well at the fiber front face, they will have a minimal overlap at some point  $\pi/(\Delta k_s - \Delta k_p)$  in the fiber. Pure fiber modes do not oscillate in the fiber, thus their overlap does not change along the fiber

length. The dashed line is the relative gain when the Stokes beam is in the LP<sub>01</sub> pure mode.

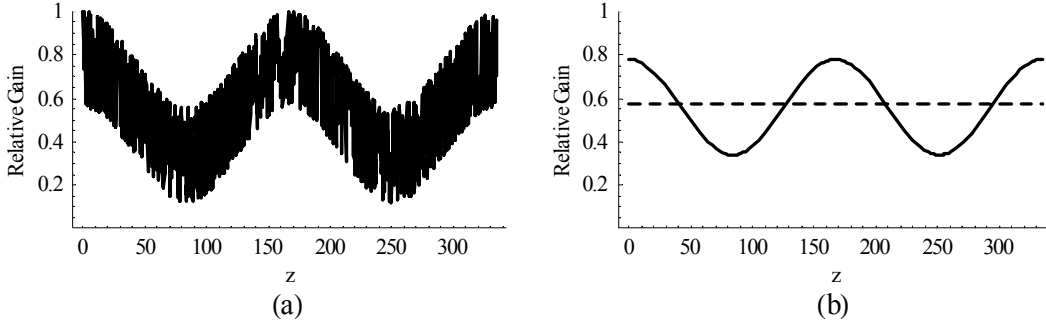


Figure 7: Relative effective gain along the length of the fiber. (a) is the calculated value.  
(b) is the calculated value when the high frequency fluctuations are averaged out.

Comparing the solid and dashed lines of Figure 7(b) sheds some light on the mechanism that is responsible for beam cleanup in long fibers. In a short fiber, the Stokes beam would propagate in the same linear combination of modes as the pump because of the greater gain. In a longer fiber however, the Stokes beam propagating in the LP<sub>01</sub> pure mode has a greater average gain.

Given Equation (4.7), the average gain over the fiber length is a simple computation.

$$g_{B_{eff\_ave}} = 2 \frac{g_B (4\epsilon_0 cn)^2}{P_s(0) P_p(0)} \left\{ \frac{1}{2} \sum_{m,j} \mathcal{A}_{sm,sm,pj,pj} \gamma_{sm,sm,pj,pj} + \dots \right. \\ \left. \sum_{m,q < m, j, v < j} \mathcal{A}_{sm,sq,pj,pv} \gamma_{sm,sq,pj,pv} \left[ \frac{\cos(\Delta\phi_{pjv} - \Delta\phi_{smq}) \operatorname{sinc}((\Delta k_{pjv} - \Delta k_{smq})L) + \dots}{(\Delta k_{pjv} - \Delta k_{smq})L} \right] \right\} \quad (4.8)$$

The Stokes mode that will be excited for a given pump can be predicted from this equation. The pump mode distribution fixes the values for all  $\mathcal{A}_{pj}$  and  $\phi_{pj}$ . Thus, the only variables left in the equation are the amplitudes and phases of the  $N$  Stokes modes excited in the fiber.

Solving for the Stokes field in this manner is computationally intensive. A typical 50-micron fiber will support more than 100 modes with a 1.064-micron pump, so there are hundreds of independent variables to determine. In order to cut down on the computation time, only four modes, LP<sub>01</sub>, LP<sub>11</sub>, LP<sub>21</sub>, and LP<sub>02</sub>, were allowed to propagate in the fiber and each mode was assumed to have a phase of zero.

The results of the analysis for an infinitely long fiber show that a pure mode was excited 100% of the time. In other words, when the input was a linear combination of all four modes, the Stokes beam had the strongest gain when it propagated in one of the pure fiber modes. The LP<sub>01</sub> mode had the greatest gain for more than 18% of the possible pump intensity distributions.

It has been demonstrated that short multimode fibers produce phase conjugate replicas of the pump beams [28-30]. Thus, in the limit that the fiber length approaches zero, Equation (4.8) should predict that the Stokes beam with the highest gain has the same modal power distribution as the pump beam. Over 200 equally spaced pump mode distributions were tested. The average phase conjugate fraction was 87%. The phase conjugate fraction is defined by Equation (4.9) where modal amplitudes are normalized such that the power in both the pump and Stokes beams has a magnitude of one. This

ensures a phase conjugate fraction of one when the Stokes beam has the same transverse intensity distribution as the pump regardless of the total power in the Stokes beam.

$$f_\phi = 1 - \frac{1}{2} \sum_j \left| \mathcal{A}_{pj}^2 - \mathcal{A}_{sj}^2 \right| \quad (4.9)$$

Figure 8(a) is a plot of the phase conjugate fraction as a function of fiber length. Figure 8(b) illustrates the percentage of the possible pump modes resulting in a Stokes beam in the LP<sub>01</sub> mode. Both of these plots show the expected trend of an increase in the beam cleanup and a reduction of the phase conjugate fraction as the fiber length increases.

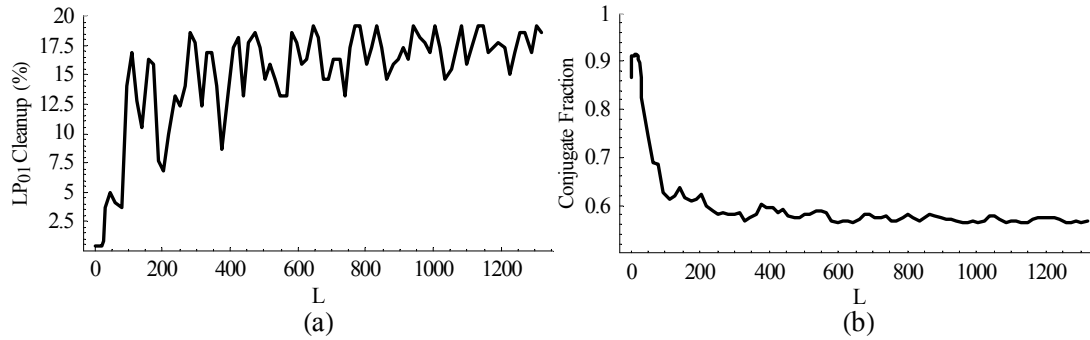


Figure 8: (a) Average phase conjugate fraction as a function of the fiber length. (b) Percentage of pump modes that lead to the excitation of the LP<sub>01</sub> Stokes mode versus the fiber length.

In practice, SBS beam cleanup in long fibers appears to be much more robust than predicted. As explained above, Equation (4.8) predicts that only 18% of the possible pump modes generate an LP<sub>01</sub> Stokes beam in an infinitely long fiber. In the laboratory, however, the LP<sub>01</sub> mode was excited almost 100% of the time as will be discussed in the remaining sections of this chapter. There are several possible reasons for this apparent disconnect.

First, it was assumed that the mode structure of the pump and Stokes beams would not evolve along the fiber length. Even ignoring the nonlinear mode coupling, power will flow between modes because the fiber is not a perfect cylinder. The fiber is wound around a spindle with an 8.5 cm radius of curvature, small imperfections in the index of refraction and the core concentricity are unavoidable in fabrication, and microbends all perturb the fiber [31-36]. Kutz analyzed these factors and found that the imperfections in the core concentricity are the leading cause of modal power diffusion [33]. He found that in a graded-index, multimode fiber, the power in each fiber mode obeys

$$\frac{dP_n}{dz} = \frac{\varepsilon^2}{2k} \sum_{m=1(m \neq n)}^N (n+1)(m+1) d_{nm} [P_m(z) - P_n(z)]. \quad (4.10)$$

where

$$d_{nm} = C(g\psi_n, \psi_m)^2 \exp\left[-(\omega_{nm}D/2)^2\right] \quad (4.11)$$

In Equations (4.10) and (4.11),  $n$  and  $m$  are mode numbers,  $\omega_{nm}$  is the difference in propagation constants between the two modes,  $P_n$  is the power in the  $n^{\text{th}}$  fiber mode,  $g$  is the transverse perturbation to the index of the fiber,  $D$  is related to the width of the Gaussian noise correlation function,  $C$  is a constant, and  $\varepsilon$  is the magnitude of the perturbation. Several features of Equation (4.10) are important in this analysis. First the coupling coefficient,  $d_{nm}$ , decays exponentially with the difference between the propagation constants of the two modes. In other words, the  $\text{LP}_{01}$  mode will not decay into the  $\text{LP}_{81}$  mode as quickly as it will decay into the  $\text{LP}_{11}$  mode. Secondly, the higher order modes will change more rapidly than the lower order modes due to the degeneracy

term in Equation (4.10),  $(n+1)(m+1)$ . Finally, assuming the coupling coefficient is nonzero, the steady state condition exists when power is uniformly shared between all fiber modes. In other words, a multimode pump beam will quickly distribute power throughout many fiber modes creating a uniform pump intensity along the fiber length. However, the Stokes beam that is generated in the  $LP_{01}$  mode will not couple to higher order modes for much greater distances. This asymmetry in the mode coupling can explain why much more than 18% of the pump intensity distributions result in beam cleanup, but it is highly dependent on the index distribution in the fiber [34, 35]. Mode mixing in step index fibers is strongest in low order modes, thus beam cleanup in these fibers may be more difficult to attain reliably.

Similarly, there will be a mixing of modes induced by the scattering process. In the beam cleanup analysis, it was assumed that all pump modes decayed at the same rate. In a physical fiber, however, the modes will not uniformly decay, but will change relative to each other since the Brillouin reflection is not uniform across the transverse fiber dimensions. One method to partially lift this restriction is to assume that the pump beam evolves through all possible mode distributions so quickly that it appears to be in all modes at once. In this manner, the Stokes mode with the greatest average overlap over all possible pump modes would dominate. The gain of a given Stokes mode in a long fiber under these conditions is shown in Equation (4.12), where  $V_{Ap}$  is the modal volume and the integral is over all possible combinations of pump modes,  $\mathcal{A}_p$ . Again only allowing four modes in the fiber and assuming the phase of each mode is zero, the  $LP_{01}$

pure mode will have a greater gain than any other mode distribution in an infinite fiber, regardless of the input.

$$g_{B\text{eff\_ave}} = 2 \frac{g_B (4\epsilon_0 c n)^2}{V_{Ap} P_s(0) P_p(0)} \int_{Ap} \left\{ \frac{1}{2} \sum_{m,j} \mathcal{A}_{sm,sm,pj,pj} \gamma_{sm,sm,pj,pj} + \dots \right. \\ \left. \sum_{m,q < m,j,v < j} \mathcal{A}_{sm,sq,pj,pv} \gamma_{sm,sq,pj,pv} \left[ \cos(\Delta\phi_{pjv} - \Delta\phi_{smq}) \text{sinc}((\Delta k_{pjv} - \Delta k_{smq})L) + \dots \right. \right. \\ \left. \left. \frac{\cos((\Delta k_{pjv} - \Delta k_{smq})L) \sin(\Delta\phi_{pjv} - \Delta\phi_{smq})}{(\Delta k_{pjv} - \Delta k_{smq})L} \right] \right\} \partial_{Ap}$$
(4.12)

Additionally, the Brillouin gain in the fiber was assumed to be constant. This is a relatively safe assumption along the transverse direction in a step-index fiber, but a graded-index fiber may behave remarkably different. The index is controlled by adjusting the concentration of dopants in the core of the cladding. For example, the addition of germanium to the core of a fiber increases the index of refraction relative to that of pure SiO<sub>2</sub>. To create a graded index fiber, the germanium content would drop from its highest value at the core center to the lowest value in the cladding. A side effect of this graduated doping level is that since the Brillouin gain coefficient is greater for GeO<sub>2</sub> than for SiO<sub>2</sub>, modes with higher intensities at the center of the fiber will be preferentially excited.

Finally, it was assumed that all fiber modes had the same attenuation. In reality, this is typically not true. The higher order modes have more power near the core-cladding interface and therefore typically have a higher scattering loss [35, 37, 38]. Since the Stokes beam grows exponentially in the fiber, even small differences in the loss can significantly change the overall distribution of power in the Stokes modes.

In summary, a theoretical model of Brillouin gain was presented. The power transmitted through the fiber was decomposed into the modal amplitudes and the gain for each Stokes mode and combination of modes was calculated. The modal distribution with the greatest average gain was assumed to be the dominant Stokes output. This analysis produced the trends seen in the laboratory. Short fibers reflected a phase conjugate replica of the pump whereas long fibers produced output in the pure fiber modes. The strength of beam cleanup was not fully predicted, but limits in the analysis were presented that could explain the differences between theory and experiment.

### **4.3. Experimental Beam Cleanup**

The properties of the cleaned Stokes beam generated in a multimode fiber are experimentally examined here. The experiments described in Section 4.3.1 verify that SBS beam cleanup is viable in a 50-micron multimode fiber. This is followed by an investigation into the polarization characteristics of the Stokes beam relative to the pump beam in Section 4.3.2. In this section, the polarization is found to be conserved upon Brillouin reflection both experimentally and theoretically. Section 4.3.3 examines the conditions in which higher order spatial modes are excited by SBS in the fiber. Finally, in Section 4.3.4 beam cleanup using a ring cavity is investigated.

#### *4.3.1. 50-micron Beam Cleanup*

Rodgers demonstrated SBS beam cleanup at ~830 nm using an 8.2-micron fiber [9]. The experiment clearly shows the viability of SBS beam cleanup. However it was limited by the fact that only 12 fiber modes could exist in the Corning SMF-28 fiber used. Because of this, the coupled energy in the fiber closely resembled the lowest order

fiber mode, indicating that some of the beam cleanup was due to spatial filtering rather than SBS. In order to increase the number of modes supported by the fiber and investigate the Stokes beam response, an experiment similar to Rodgers's was performed using a 50-micron fiber core. For such a large core, hundreds of fiber modes can be excited as predicted by Equation (2.17).

### Experimental Setup

The experimental setup used to demonstrate SBS beam cleanup is shown in Figure 9. The output of a cw Nd:YAG Lightwave Electronics laser operating at 1.064 microns was used as the pump beam. The laser had an instantaneous linewidth less than 5 kHz, far less than the SBS gain bandwidth,  $\sim$ 100 MHz. A four-pass amplifier was used to increase the beam power to greater than a watt. The output of the amplifier then passed through a microscope slide that had been etched for five minutes in hydrofluoric acid. The acid created random pits in the glass surface that aberrated the phase front of the pump beam. This aberrated beam was then transmitted through a Faraday rotator, an angled plane-parallel plate, and finally into the 4.4 km, 50-micron, graded-index fiber.

The backward traveling Stokes beam was collimated by the microscope objective and a small portion of the beam reflected off the back surface of the plane parallel plate and was coupled into a CCD camera. The remaining Stokes beam was coupled back through the Faraday rotator to be detected by a Fabry-Perot for spectral characterization and a power meter for a measurement of the SBS efficiency.

The CCD images were used to characterize the improvement in the quality of the Stokes beam over that of the pump beam. First, a set of images of the reflected beam was

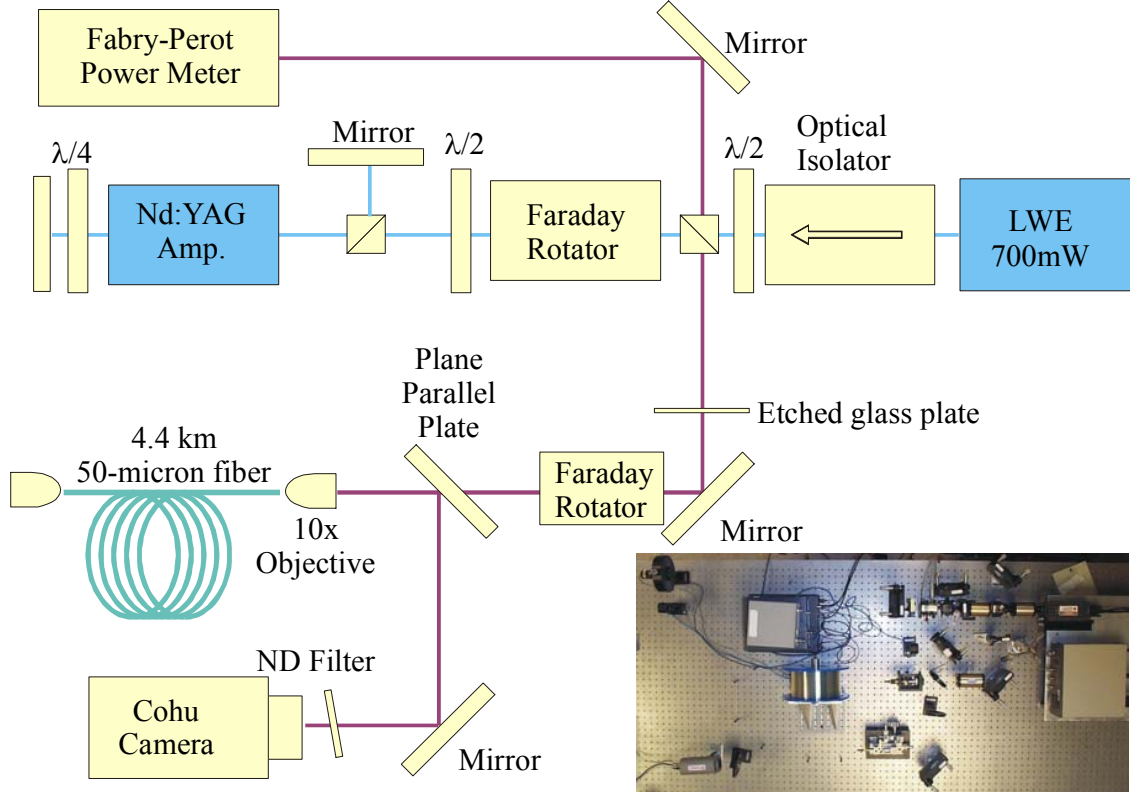


Figure 9: Schematic of experiment used to examine beam cleanup.

collected above SBS threshold that included the Fresnel reflection off the front fiber facet as well as the Brillouin reflected beam. Secondly, without adjusting the beam coupling, the fiber was cut about two meters beyond the front facet and another set of CCD images was collected. The reduction in fiber length increased SBS threshold well beyond the power generated by the laser and amplifier, thus the second image was purely due to the Fresnel reflection off the front fiber facet. Finally, a third group of images was collected of the transmitted pump beam at the end of the two-meter section of fiber. The power coupled into the fiber was also measured at this point to determine the coupling efficiency into the fiber.

The effect of the location of the pump beam on the position of the Stokes beam was also explored. To perform this experiment, the amplifier and phase aberrator were removed from the experimental setup and the pump beam was again coupled into a 4.4 km fiber. The pump beam position was controlled with the mirror indicated in Figure 10. At each mirror position, a set of images was collected showing the position of the pump and Stokes beam and the power of the transmitted pump and reflected Stokes beam was recorded.

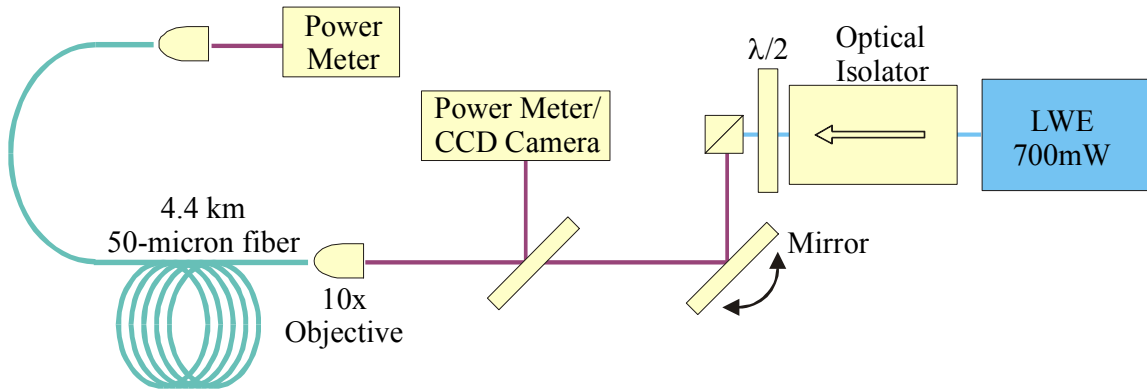


Figure 10: Schematic depicting the experimental setup to investigate the dependence of pumping conditions on the efficiency.

## Results

The measured power in the Stokes beam as a function of the power coupled into the fiber is shown in Figure 11. The solid line indicates the best fit to the data. It results in a threshold  of 420 mW and the slope efficiency of 52.4%.

The intensity distributions of the reflected pump, Stokes, and transmitted pump beams are shown in Figure 12(a-c) respectively. Part (a) clearly shows that a highly aberrated pump beam is incident on the front fiber facet. Part (b) demonstrates that the Stokes beam appears to be excited in a Gaussian-like beam. Finally, part (c) reveals

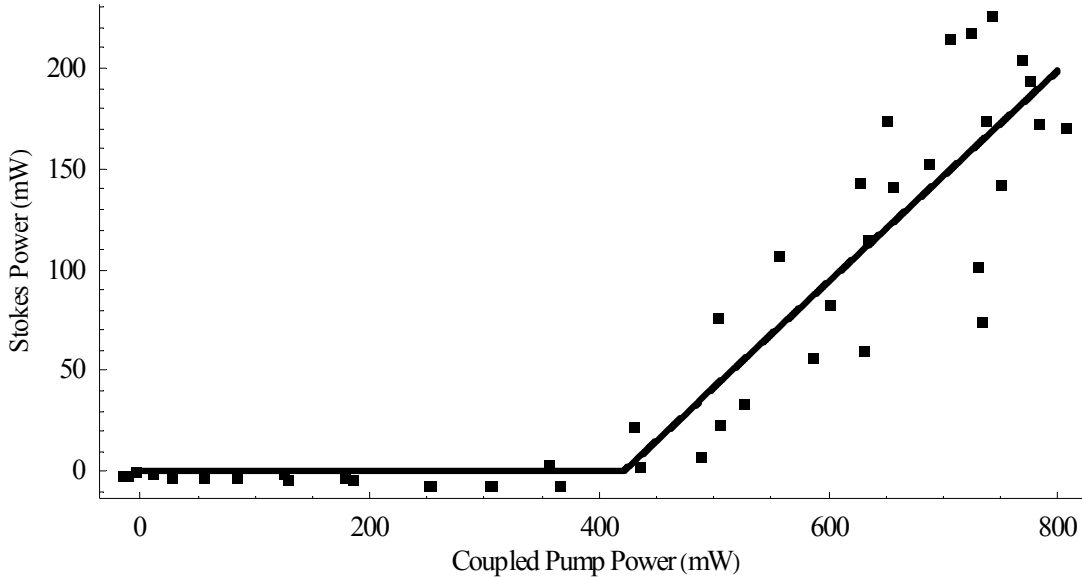


Figure 11: Power in the Stokes beam as a function of the pump beam. The slope efficiency is 52.4% and the threshold is 420 mW.

that the pump beam is coupled into many fiber modes, ensuring that the fiber did not spatially filter the pump beam.

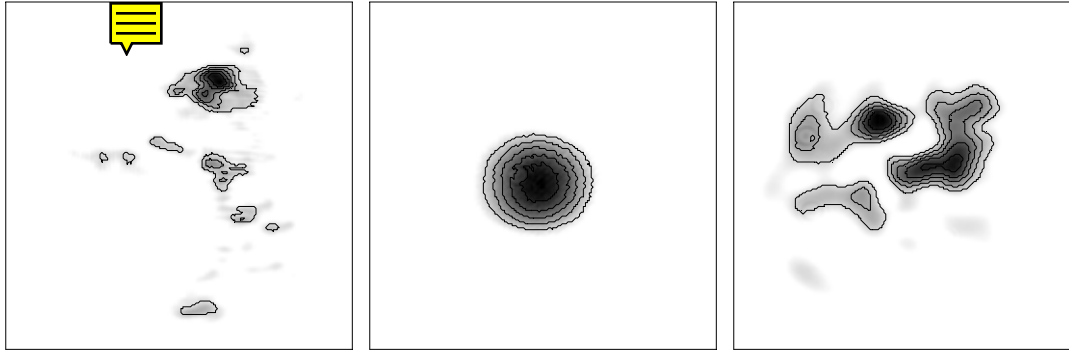


Figure 12: (a) Pump beam shape, (b) Stokes beam shape, (c) Transmitted beam shape

While qualitatively satisfying, Figure 12 does not give a quantitative measure of the beam cleanup. Thus, in order to complete the analysis, a measurement of beam quality had to be developed. Typical  $M^2$  measurements require beam stability over the time frame of experiment. This allows the beam width to be measured at several different

points as the beam passes through focus. By comparing the divergence of the beam with that of a perfect Gaussian with the same beam waist, the beam quality can be reduced to a single number. Unfortunately, due to instabilities in the experiment, this measurement could not be undertaken. There are a couple possible reasons the laser beam was unstable. First, since there is no feedback in a single pass SBS setup, the stimulated process must begin from spontaneous scattering, which is inherently random. Secondly, the power coupled into the fiber was measured and found to fluctuate by as much as 10%. This could be due to pointing instability in the laser or vibrations of the fiber end. In either case, the measurement of  $M^2$  was replaced by a simpler, but less robust method described below.

A perfect Gaussian beam is diffraction limited. Thus, how well a beam matches a Gaussian intensity distribution is a measure of its beam quality. This is the principle behind the beam quality measurements taken in this experiment. First, the area under each intensity distribution, was normalized to one. With the normalization complete, the nonlinear fit algorithm in Mathematica was used to fit the data to a Gaussian with the same area,

$$g(x, y) = \frac{1}{\pi b^2} \exp\left(-\frac{(x - x_0)^2 + (y - y_0)^2}{b^2}\right) \quad (4.13)$$

where  $b$  is the beam size and  $(x_0, y_0)$  is the beam center. This algorithm finds a local minimum in the least square error between the data and the fitting function. Since a local minimum, not a global minimum, is found, it is critical that a good estimate be used as a starting point for the search. The initial guess for the beam center was estimated by

finding the centroid of the intensity distribution. The beam diameter was then estimated by calculating the standard deviation of the intensity distribution from the centroid. If the beam was a perfect Gaussian, this would return the correct beam center and waist. For beams that are not Gaussian, it is a good starting point for a fit to the data.

The best-fit output was then compared to the actual data using the estimated variance,

$$\chi^2 = \frac{1}{N-3} \sum_{i,j} (g_{i,j} - I_{i,j})^2 . \quad (4.14)$$

In this equation  $g_{i,j}$  is the value of the Gaussian fit at point  $(i,j)$ ,  $I_{i,j}$  is the intensity of the beam at  $(i,j)$ , and  $N - 3$  is the number of degrees of freedom in the Gaussian fit.

This analysis results in the beam quality factors summarized in Table 1. These values confirm the qualitative analysis of Figure 12. The Stokes beam is found to have an intensity distribution that matches a Gaussian beam 18 times better than the pump input and more than 9 times better than the transmitted pump beam.

Table 1: Beam quality factors for beam cleanup experiment

|   | Pump Input     | Stokes Beam   | Coupled Beam   |
|---|----------------|---------------|----------------|
| Variance of Gaussian Fit ( $10^{-5}$ ) - $\chi$ | $32.7 \pm 1.6$ | $1.8 \pm 0.7$ | $16.4 \pm 0.3$ |
| Relative Fit                                    | 18.2           | 1             | 9.1            |

The effect of the location of the pump beam on the Stokes output was also monitored with the CCD camera. The results are shown in Figure 13. This data shows that as the pump beam is moved from the upper right to the lower right of the frame, the output position of the Stokes beam is constant. This unequivocally demonstrates that the Stokes

beam is not a phase conjugate replica of the pump beam. A phase conjugate beam would move along with the pump.

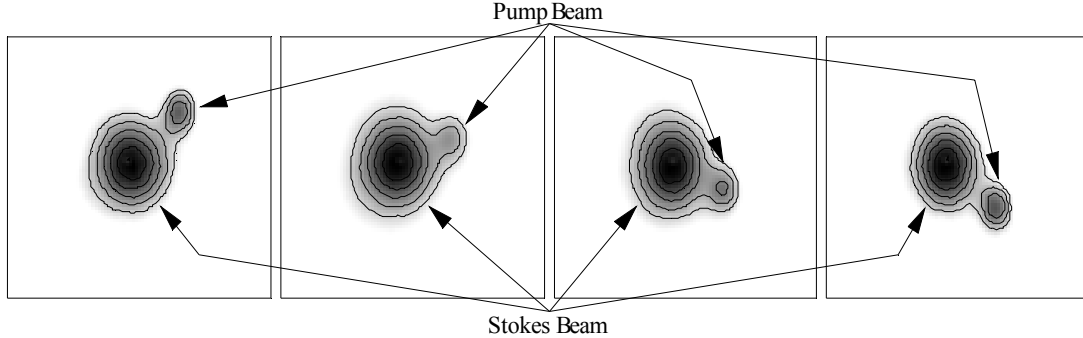


Figure 13: The Stokes beam does not significantly move as the input beam position is varied from the upper right to the lower left.

Although not as obvious, Figure 13 also hints that the efficiency of the Stokes reflection increases when the pump beam is coupled into the center of the fiber. The power of the reflected Stokes beam is constant in each frame. However, its intensity relative to that of the Stokes beam clearly changes. The contours in the second frame illustrate that the intensity of the Stokes beam is much greater than the intensity of the reflected pump beam. The first and last frames, however, show that the reflected pump beam intensity is nearly as strong as the Stokes beam.

This was further investigated by measuring the power that was transmitted through and reflected from the fiber. Figure 14(a) shows the relative transmission coefficient as a function of the pump power and the beam position. On the far edges, the transmission drops to zero because the beam is clipped by the edge of the fiber core. However, even when the beam is fully coupled into the fiber, the transmission above SBS threshold is lower near the center of the core than near the edge due to an increase in SBS efficiency.

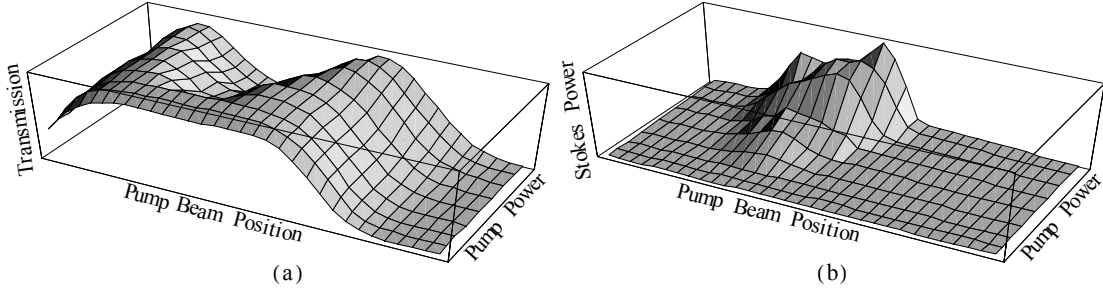


Figure 14: Transmission through (a) and Brillouin reflection from (b) an optical fiber as a function of pump power and pump beam position from one edge of the fiber core to the other.

The transmission curves have the advantage of clearly showing the physical edges of the fiber. However, the Stokes beam is the true signal. Figure 14(b) shows the measured Stokes signal, which demonstrates the same features as the transmitted beam. SBS is found to be most efficient near the center of the fiber. These results are consistent with the theory presented in Section 4.2. The effective Brillouin gain is proportional to the overlap of the pump and Stokes beams as given by Equation (4.3). Since the Stokes beam is consistently found in the  $LP_{01}$  mode, when the pump beam is coupled into the fiber edges, the overlap will be diminished and the effective Brillouin gain is lowered. Of course even a spot that is coupled into the edge of the core will evolve into a superposition of many fiber modes, thus the overlap of the  $LP_{01}$  mode and the pump beam at the front fiber facet will not necessarily approximate the overlap of the two beams along the entire fiber length.

On the other hand, the spatial extent in which SBS is observed in Figure 14 is a good measure of where the pump beam can be coupled into the fiber, while still contributing to the overall Stokes beam. To determine this spatial extent, the efficiency of the Brillouin reflection was assumed to be proportional to a Gaussian function concentric with the fiber core.

$$\eta(r) = \eta \exp\left(-\frac{r^2}{b_0^2}\right) \quad (4.15)$$

where  $\eta$  is the slope efficiency when the pump beam is coupled into the center of the fiber core and  $b_0$  is the radius of the Gaussian function. The efficiency affects the overall Stokes power in the following manner

$$P_s = \begin{cases} 0 & \eta(r)P_p < P_{th} \\ \eta(r)P_p - P_{th} & \eta(r)P_p > P_{th} \end{cases}. \quad (4.16)$$

This, in turn, can be used to estimate the transmission coefficient at various pump power levels and to find  $b_0$ .

Figure 15 shows several slices of the transmission surface at various power levels along with the best fit to them. In part (a), the transmission below threshold is shown. This was used to estimate the size of the pump beam on the front fiber facet. The plots shown in (b,c) demonstrate the transmission above threshold at two power levels. The best fits were found with different values for  $b_0$ . In (d), the size of  $b_0$  is plotted as a function of the pump power. Clearly, this is not a constant value and as the pump power increases, the edges of the fiber become increasingly valuable.

These results indicate that the efficiency of SBS beam cleanup will be a function of the pump beam spatial quality. For low beam quality, when much power is coupled into the edges of the fiber, the conversion efficiency will be low and threshold will be high. Once above threshold however, the entire pump beam will contribute to the Stokes beam.

This is unlike a spatial filter, which blocks the high spatial frequency components of the beam and thus has a very low efficiency for highly aberrated beams.

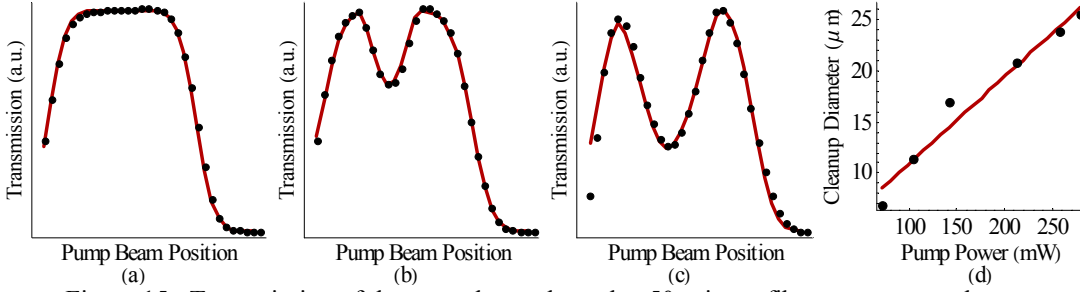


Figure 15: Transmission of the pump beam through a 50-micron fiber versus pump beam position at various pump power levels. (a) Low power transmission below SBS threshold. (b-c) Transmission above threshold. (d) Effective cleanup diameter as a function of the pump power.

#### 4.3.2. SBS Polarization Properties

Rodgers investigated the polarization properties of the Stokes beam generated through stimulated Brillouin scattering and found that it had the same polarization as the pump beam. This differs from a standard mirror in which a right-hand-circularly polarized incident wave is reflected into a left-hand-circularly polarized beam. It also contradicts the prediction of Zel'dovich [39], and therefore was investigated further.

#### Experimental Setup

Figure 16 shows a schematic of the experimental setup used to investigate the polarization properties of the Stokes beam. A diode laser operating above SBS threshold at 831 nm was transmitted through a quarter-wave plate thus converting the horizontally polarized pump beam to a right-hand-circularly polarized beam. The light was then coupled into an 8.2-micron step-index fiber. The reflected Stokes beam traveled back through the quarter-wave-plate. After this second pass through the quarter-wave-plate

portion of the reflected beam that was right (left)-hand-circularly polarized became vertically (horizontally) polarized. A portion of this beam was then reflected off an uncoated plane-parallel plate, transmitted through a Glan-Thompson polarization analyzer and detected by a Fabry-Perot. The relative power in the reflected pump and Stokes beam was measured by the Fabry-Perot trace and recorded at various analyzer angles.

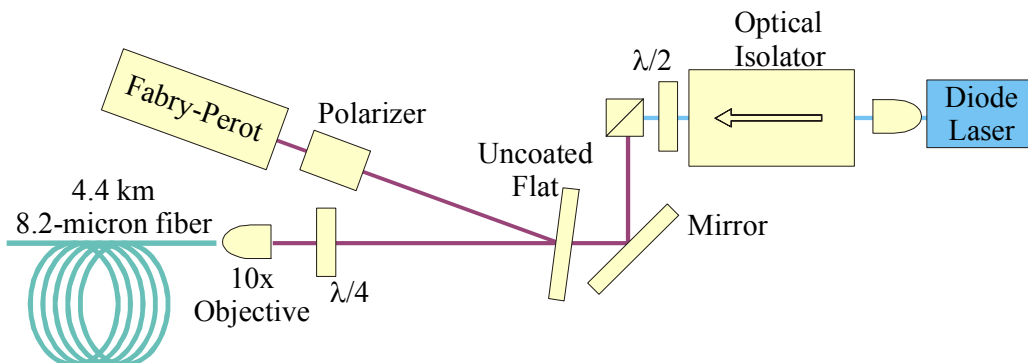


Figure 16: Schematic diagram of polarization characterization experiment.

## Results

Figure 17 shows the results of this measurement. The power in the reflected pump beam, represented by the solid line, is caused by the Fresnel reflection off the front fiber facet. Fresnel reflection is well known to reverse the handedness of the polarization. Conversely, the Stokes beam, represented by the dashed line, is found to have a polarization that is orthogonal to the pump, thus showing that the handedness of the polarization is conserved when the beam is reflected through stimulated Brillouin scattering.

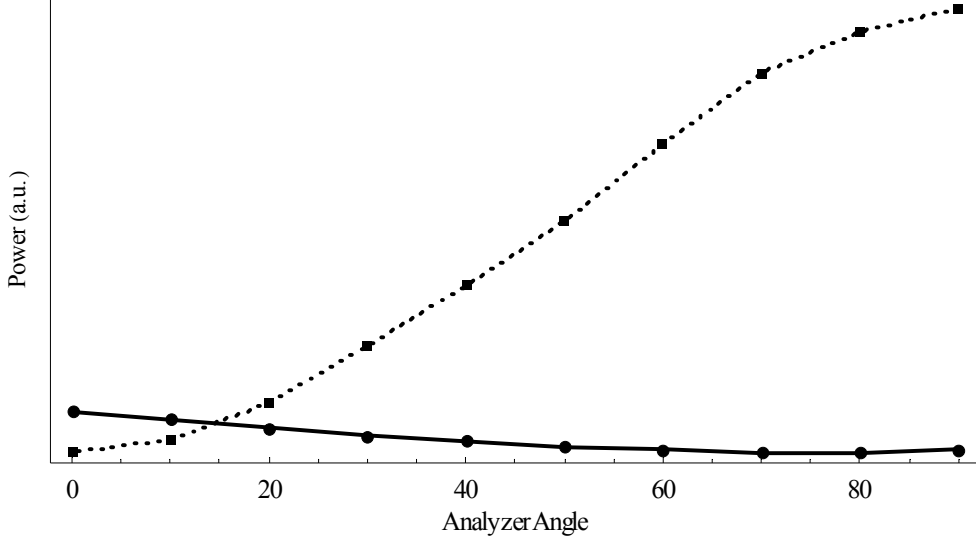


Figure 17: Reflected pump (solid) and Stokes (dashed) power as a function of the analyzer angle. The two are out of phase by  $90^\circ$  showing that the polarization of the Stokes beam is orthogonal to that of the reflected pump.

Although the observed polarization properties of the Stokes beam were not expected [39], they are easily explained by decomposing the pump and Stokes electric fields into  $x$  and  $y$  components and investigating how the Brillouin reflection affects the phase of each.

$$\begin{aligned} E_p &= A_{px} \exp[i(k_p z - \omega_p t + \phi_{px})] \hat{i} + A_{py} \exp[i(k_p z - \omega_p t + \phi_{py})] \hat{j} \\ E_s &= A_{sx} \exp[i(-k_s z - \omega_s t + \phi_{sx})] \hat{i} + A_{sy} \exp[i(-k_s z - \omega_s t + \phi_{sy})] \hat{j} \end{aligned} \quad (4.17)$$

$A_{px,sx}$  ( $A_{py,sy}$ ) is the amplitude of the pump and Stokes fields along the  $x$ -( $y$ -)axis and  $\phi_{px,sx}$  ( $\phi_{py,sy}$ ) is the phase of the  $x$  ( $y$ ) component of the field. Assuming the Stokes beam is not externally seeded, it is initialized by spontaneous scattering of the pump off thermal phonons in the fiber [40]. The phonon frequency and wavenumber are fixed by material properties thus the density fluctuations in the fiber is assumed to have the form

$$\rho_n = A_n \exp \left\{ i \left[ (k_s + k_p)z - (\omega_p - \omega_s)t + \phi_n \right] \right\}. \quad (4.18)$$

$\phi_n$  is the random phase of the phonon and  $A_n$  is the amplitude of the wave.

Stimulated scattering requires that the reflected Stokes beam interfere with the pump beam such that the acoustic wave is intensified through electrostriction. In other words, the high intensity regions caused by the interference between the pump and Stokes beams must overlap the high density regions in the fiber.

$$\begin{aligned} \exp \left\{ i \left[ (k_p + k_s)z - (\omega_p - \omega_s)t + \phi_{px} - \phi_{sx} \right] \right\} &= \exp \left\{ i \left[ (k_s + k_p)z - (\omega_p - \omega_s)t + \phi_n \right] \right\} \\ \exp \left\{ i \left[ (k_p + k_s)z - (\omega_p - \omega_s)t + \phi_{py} - \phi_{sy} \right] \right\} &= \exp \left\{ i \left[ (k_s + k_p)z - (\omega_p - \omega_s)t + \phi_n \right] \right\} \end{aligned} \quad (4.19)$$

Both of these equations are only satisfied if the difference between the phases goes to zero. Since the phase of the thermal phonon and both components of the pump beam are fixed, the phase of both components of the Stokes beam can be found,

$$\begin{aligned} \phi_{sx} &= \phi_{px} - \phi_n \\ \phi_{sy} &= \phi_{py} - \phi_n \end{aligned} \quad (4.20)$$

Thus the  $y$ -components of both the pump and Stokes beams lag the  $x$ -components by an equal amount,  $\phi_{sy} - \phi_{sx} = \phi_{py} - \phi_{px}$ , and the handedness of the polarization is preserved.

Although the polarization is maintained during Brillouin reflection at each point in the fiber, the polarization is not preserved as the beam propagates through the fiber. Fiber imperfections result in a small, random birefringence that leads to a fluctuating elliptical polarization along the fiber length. The birefringence is not large, approximately 1 part in 10 million [41], but the long fiber lengths used in beam cleanup

make it significant. If the birefringence was oriented in a constant direction, the fiber could rotate the polarization of a guided beam by  $90^\circ$  in approximately 5 m. In practice, however, fibers that are thousands of meters long reflect Stokes beams that are identical in polarization to the pump beam. If the Stokes beam propagated at the same frequency and in an identical fiber mode, it would pass back through the effective waveplate produced by the fiber birefringence, perfectly retracing the polarization of the pump beam. The Stokes beam, however, is not at the same frequency as the pump due to the Brillouin shift and cleanup modifies the beam's spatial structure. These characteristics of the Stokes beam limit the useful fiber length if a polarized output is required.

Since the birefringence is random, the relative phase shift imparted to the orthogonal polarization modes does not grow linearly. The phase difference can be treated like a random walk. When the birefringence is aligned such that the fast axis coincides with the  $x$ -direction, the random step advances the phase of the  $x$ -polarized beam. When the birefringence aligns the fast axis in the  $y$ -direction, the random step advances the phase of the  $y$ -polarized beam. For simplicity, the birefringence is constrained to one of these two axes. Although a more general approach would include random steps where the fast axis is aligned at random angles to the  $x$ - and  $y$ -axes, the approach taken shows the features of polarization mode dispersion needed. The birefringence is assumed to be constant over lengths,  $L_b$ , making discontinuous shifts between segments. The distance of each step in this random walk is the magnitude of the phase shift imparted to the beam over  $L_b$ ,  $\Delta\phi_b = \left(\frac{2\pi}{\lambda}\right)L_b\Delta n$ . The number of steps taken is the number of constant birefringence zones in the fiber,  $N = \frac{L_f}{L_b}$ , where  $L_f$  is the fiber length.

The probability that  $m$  of the  $N$  zones are oriented such that light polarized along the  $x$ -axis propagates faster than that polarized along the  $y$ -axis is given by the binomial probability distribution, which for large  $N$  can be approximated by a Gaussian distribution,

$$2\left(\frac{2}{\pi N}\right)^{1/2} \exp\left(-\frac{2}{N}(N-2m)^2\right). \quad (4.21)$$

If a large number of fibers were tested, it would be found that the average number of zones with the fast axis oriented in the  $x$ -direction is

$$\begin{aligned} m_{ave} &= 2\left(\frac{2}{\pi N}\right)^{1/2} \int_{-\infty}^{\infty} m \exp\left(-\frac{2}{N}(N-2m)^2\right) dm \\ &= \frac{N}{2} \end{aligned} \quad (4.22)$$

As expected, this is exactly  $\frac{1}{2}$  of the total number of zones. This is required by the fact that the  $x$ - and  $y$ -axes have not yet been defined so there cannot be a preferred axis. On the other hand, this is only an average. Some of the fibers would be found to have a net birefringence along the  $x$ -axis and some with a net birefringence along the  $y$ -axis. The difference between the number of zones oriented along the  $x$ -axis,  $m$ , and the number oriented along the  $y$ -axis,  $N-m$ , is the number of zones that constructively add to create the total birefringence of a fiber,  $b_z = N - 2m$ . The average magnitude of this number is proportional to the average magnitude of the birefringence of a fiber.

$$\begin{aligned}\overline{|b_z|} &= 2 \left( \frac{2}{\pi N} \right)^{1/2} \int_{-\infty}^{\infty} |b_z| \exp\left(-\frac{2}{N}(b_z)^2\right) db_z \\ &= \sqrt{\frac{2}{\pi} N}\end{aligned}\tag{4.23}$$

Thus the number of zones that constructively add together is proportional to the square root of the total number of zones and the average relative phase shift at the end of the fiber is

$$\Delta\phi_T = \Delta\phi_b \sqrt{\frac{2}{\pi} N} = \frac{2\Delta n}{\lambda} \sqrt{2\pi L_b L_f}.\tag{4.24}$$

This shows that the phase difference grows in proportion to the square root of the fiber length rather than linearly with the length. The collection of terms  $\frac{\Delta n}{c} \sqrt{\frac{2}{\pi} L_b}$ , where  $c$  is the speed of light, is known as the characteristic polarization mode dispersion (PMD). It is an important measure of the pulse spreading in fiber waveguides because a high characteristic PMD will limit the rate that data can be sent over fiber optic cables. It is typically on the order of  $0.1 \text{ ps}/\sqrt{\text{km}}$  [41] and is introduced here because it can be used to estimate the value of  $L_b$ .

As the pump beam travels down the fiber, the phase delay of orthogonal polarization components differ by an amount given by Equation (4.24). The Stokes beam will experience similar phase delays, but since it is propagating backward through the fiber and starts with the polarization that is conjugate to the pump, the phase delays act to reconstruct the original pump polarization. Any differences between the phase delay imparted to the pump and the phase delay imparted to the Stokes beam will generate a

polarization shift between the input pump and the output Stokes. Setting the difference between the two phase delays equal to  $\pi$  gives an estimate to the allowed fiber length that conserves polarization during Brillouin reflection.

$$\Delta\phi_p - \Delta\phi_s = 2\sqrt{2\pi L_b L_f} \left( \frac{\Delta n_p}{\lambda_p} - \frac{\Delta n_s}{\lambda_s} \right) = \pi$$

$$L_f = \frac{\pi}{8L_b} \left( \frac{\Delta n_p}{\lambda_p} - \frac{\Delta n_s}{\lambda_s} \right)^{-2}$$
(4.25)

Chromatic dispersion and modal dispersion affect the birefringence in the fiber. Chromatic dispersion is relatively small over the wavelength shift induced by SBS and will be ignored. Modal dispersion, however, is significant since beam cleanup requires that the Stokes beam propagate in the  $LP_{01}$  mode and the pump beam to propagate in higher order modes. Figure 18 shows the allowed fiber length as a function of the mode number for a 50-micron step index fiber. Clearly the higher order modes require a shorter fiber if polarization is to be maintained. However, even if the pump is coupled into the highest order mode and the Stokes beam propagates in the  $LP_{01}$  mode, the polarization can be maintained in fibers that are nearly 3 km.

There are several limitations to this calculation. First, it is not likely that the pump beam will propagate in a pure fiber mode, so the actual allowed fiber length is expected to be a weighted average that takes into account the percentage of pump power in each fiber mode. Secondly, the 50-micron fiber used in the experiment had a graded index profile. Graded-index fibers are designed to have much less modal dispersion, thus it is expected that the fiber length could be much greater and still maintain the Stokes polarization. Additionally, the calculation ignores the fact that most of the Brillouin gain

occurs in the front end of the fiber so it is more appropriate to interpret the vertical axes of Figure 18 as the effective length rather than the physical length of the fiber.

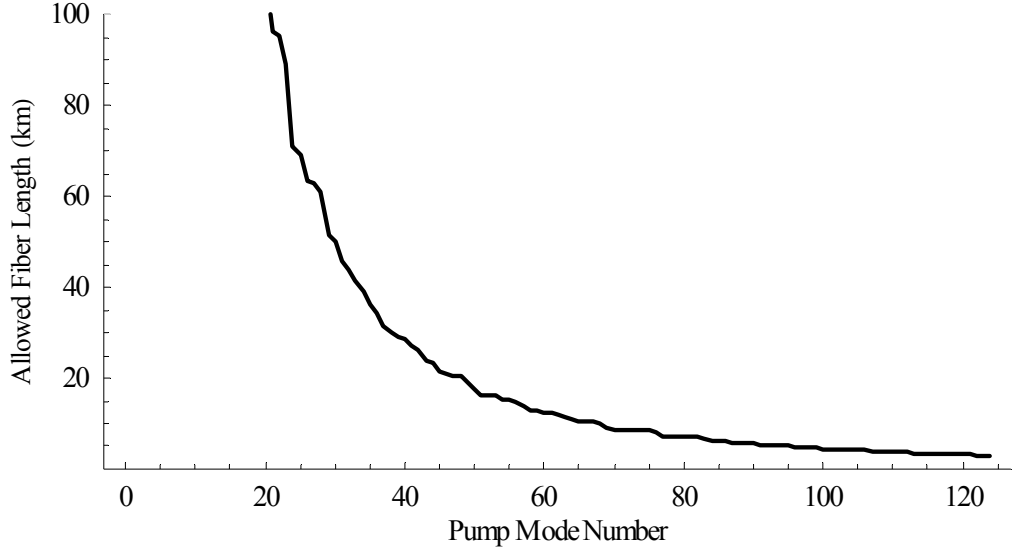


Figure 18: Modal dispersion limits the fiber length if a polarized Stokes output is desired. The allowed fiber length is shown as a function of the pump beam fiber mode. The Stokes beam is assumed to propagate in the  $LP_{01}$  mode.

#### 4.3.3. High Spatial Order Stokes Modes

In the preceding sections of Chapter 4, SBS beam cleanup is experimentally shown to produce a high quality Stokes beam in the  $LP_{01}$  fiber mode under several different pumping conditions. However, the theoretical examination of beam cleanup demonstrated that it should be possible to excite other pure fiber modes. This section describes experimental evidence of this, as well as confirmation of mode competition in the fiber.

#### Experimental Setup

A schematic of the experimental setup is shown in Figure 19. The frequencies of two Lightwave Electronics Nd:YAG single-frequency lasers were tuned to within the

Brillouin gain bandwidth of each other. The beams were then spatially combined using a polarization beamsplitter and coupled into a 4.4 km, 50-micron, graded-index fiber. A portion of the reflected Stokes beam was picked off using the Fresnel reflection off the front surface of an uncoated plane-parallel plate. It was then viewed with a CCD camera. The portion of the beam that reflected off the back surface of the plane-parallel plate was monitored with a scanning Fabry-Perot interferometer to ensure the frequencies of the two beams did not drift away from each other.

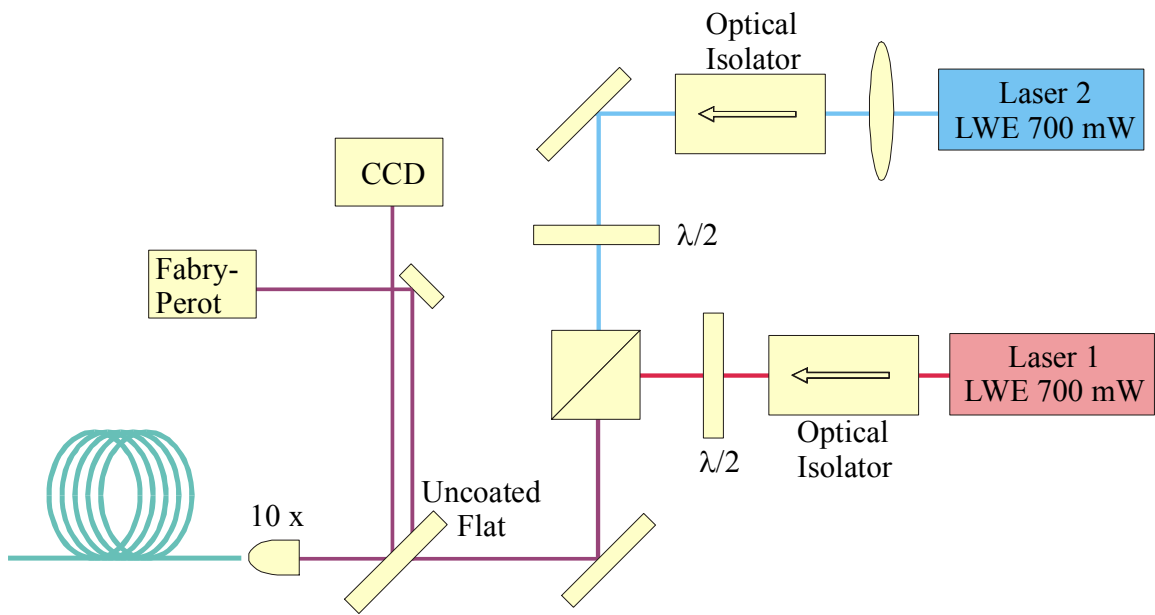


Figure 19: Multimode Stokes beam experimental schematic.

The coupling of the two beams into the fiber was carefully controlled. With the first laser blocked, the position of the second laser beam was adjusted to maximize the Stokes power generated. Once completed, the second laser was blocked and the coupling of laser 1 was adjusted until the reflected Stokes beam appeared to propagate in the  $LP_{11}$  mode. It was not a simple task to excite this spatial mode. Once excited, it would often spontaneously shift into the  $LP_{01}$  intensity pattern and again have to be adjusted to excite

the LP<sub>11</sub> mode. CCD images of the Stokes beam excited by each laser operating independently, as well as both lasers working together were collected. Finally, the frequency of the second laser was tuned slightly away from that of laser 1. Again the intensity of the Stokes beam generated by the combined action of both beams was imaged on the CCD.

### Results

The Stokes beams generated when laser 1 and laser 2 each independently pumped the fiber are shown in Figure 20(a) and (b). Laser 1 clearly produced a two lobed output, unlike the beams generated through SBS with a highly aberrated beam. This output is similar to the LP<sub>11</sub> optical mode in a fiber. On the other hand, laser 2 generated a Stokes beam with a Gaussian intensity distribution consistent with the LP<sub>01</sub> mode.

Parts (c) and (d) of Figure 20 show the intensity distribution of the Stokes beam produced when the fiber was pumped by both lasers simultaneously. The difference between the figures results from the spectral characteristics of the pump beams. Part (c) shows the output when both lasers operate at the same frequency. It will be demonstrated in Chapter 5 that under this condition, the two lasers work together to produce a single Stokes beam that is temporally coherent. In contrast, when the two laser frequencies are separated by more than the Brillouin gain bandwidth, they generate independent Stokes beams and do not interact in a significant way. This condition is shown in part (d) of Figure 20.

When the two pump beams work together (see Figure 20(c)), the LP<sub>11</sub> mode generated by laser 1 is lost and a single Gaussian-like Stokes beam is generated. In order

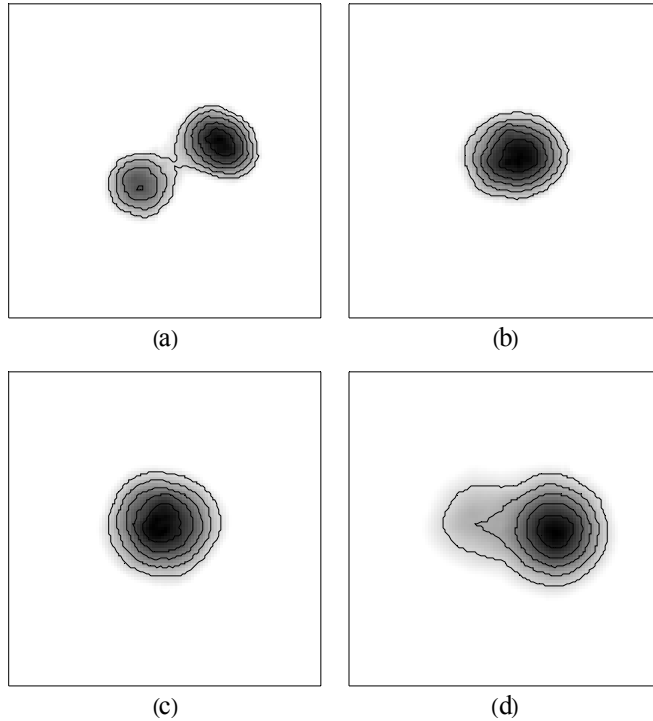


Figure 20: (a) The intensity pattern of the Stokes beam generated by laser 1. (b) The intensity pattern of the Stokes beam generated by laser 2. (c) The intensity pattern of the Stokes beam generated when both lasers pump the fiber simultaneously at the same frequency. (d) The intensity pattern of the Stokes beam generated when both lasers pump the fiber simultaneously at different frequencies.

to prove that the  $LP_{11}$  mode is not just hidden under a much stronger  $LP_{01}$  mode, the powers of the two independently generated Stokes beams were measured and found to be nearly the same. Thus, if these two beams were incoherently added, the Stokes intensity pattern would still contain a strong portion of the two lobes from laser 1.

It could also be argued that the addition of laser 2 changed the optical path of the first laser by a tiny fraction. This could be a result of heating the fiber, a change in path due to the second acoustic wave produced, or another nonlinear effect. Since the generation of the higher order Stokes beam in the  $LP_{11}$  mode was extremely sensitive to the pump alignment, any of these minuscule effects could change the coupling enough to cause the first Stokes beam to generate an  $LP_{01}$  mode. On the other hand, none of these should be

significantly affected by a shift in the frequency of laser 2 by less than 1GHz. Yet when the second laser was tuned outside the Brillouin gain bandwidth, the Stokes beam intensity distribution reverted to that shown in part (d), which closely matches the incoherent addition of the intensity patterns shown in parts (a) and (b).

The most viable explanation to the observed phenomena is that the spatial modes in the fiber compete for the gain. When laser 1 pumped the fiber alone, the LP<sub>11</sub> mode had the highest gain, resulting in an output that closely matched it. However, when both lasers worked together, the LP<sub>01</sub> mode had the greatest gain and became dominant, thus suppressing the higher order modes.

#### *4.3.4. Ring Cavity Beam Cleanup*

The SBS threshold is reduced when the Stokes beam is seeded at the back end of the fiber. This decreases the overall loss, thus increasing efficiency. While a second laser at the Stokes frequency is the most obvious choice, in practice it is difficult to control the two lasers to ensure the seed beam is pumped within the narrow Brillouin gain bandwidth of the pump beam. The approach taken by Choi in his research at AFIT was to use a portion of the pump to excite a Stokes beam in a second fiber. This beam was then coupled into the back end of the fiber used for beam cleanup [42]. In this geometry, a single-mode fiber could be used to generate the seed beam, thus threshold for the seed is very low. This configuration also has the benefit of ensuring that as the frequency of the pump beam drifts, the seed frequency follows it. Unfortunately, a highly aberrated pump beam will not efficiently couple into a single mode fiber, increasing the power required to generate the seed and reducing the overall efficiency.

Another approach that eliminates these problems is to use a single fiber in a ring cavity. This has the benefit of reducing the SBS threshold [27], but does not waste power due to low coupling efficiency. This approach was taken in the research described here.

### Experimental Setup

The experiment was completed in two parts. First, the Stokes beam shape was observed to determine if seeded beam cleanup is possible. Secondly, the Stokes beam power was measured at different levels of seeding to determine how much was required to increase SBS efficiency. These experiments used the setup shown in Figure 21.

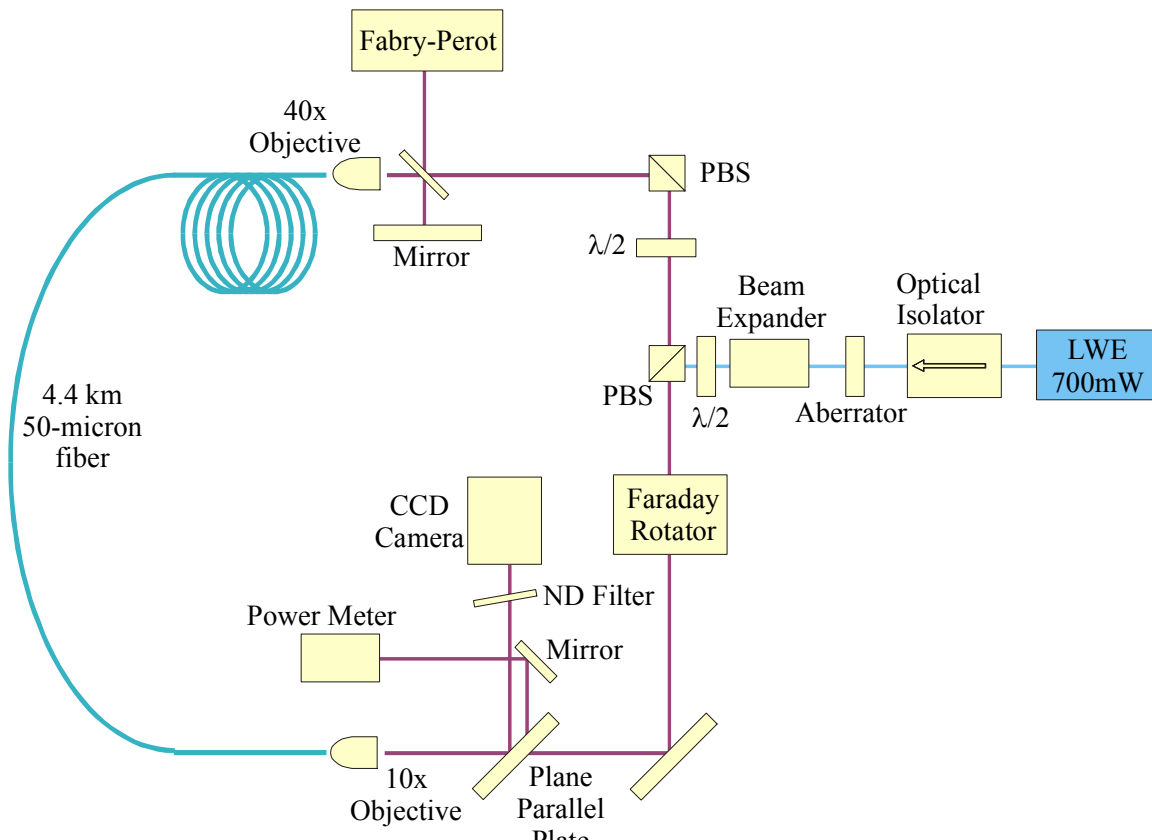


Figure 21: Ring cavity SBS beam cleanup experiment

As in the previous beam cleanup experiment, a Lightwave Electronics 700 mW source was aberrated using an etched glass plate. The beam then traveled through a polarization beamsplitter, Faraday rotator, and was focused into a 4.4 km, 50-micron optical fiber. After scattering out the front of the fiber, a portion of the beam was reflected off the front and back surfaces of a plane parallel plate. The reflection off the back surface was imaged with a CCD camera. The reflection off the front surface was measured with a power meter. The rest of the beam passed back through the Faraday rotator and was transmitted through the polarization beam splitter. Another half-wave plate and polarizer were used to control the amount of the reflected Stokes beam that was coupled into the back end of the fiber. The spectrum of the transmitted and reflected beams was measured using the reflection off a microscope slide and a scanning Fabry-Perot interferometer.

### Results

Figure 22 shows the intensity distribution of the Stokes beam for a variety of half-wave-plate settings. The labels indicate the ratio of the power that is reflected by the second polarization beam splitter to the power incident upon it. It is related to the quality factor,  $Q$ , of the ring cavity, and is directly proportional to the seed power coupled into the back end of the fiber. The proportionality constant is determined by the transmission of all the optical elements as well as the coupling efficiency at the back fiber facet. This coupling efficiency is expected to be low. A 40x microscope objective with a numerical aperture of 0.4 was used at this end of the fiber to ensure the seed beam filled fiber core ( $NA = 0.2$ ), regardless of its mode structure.

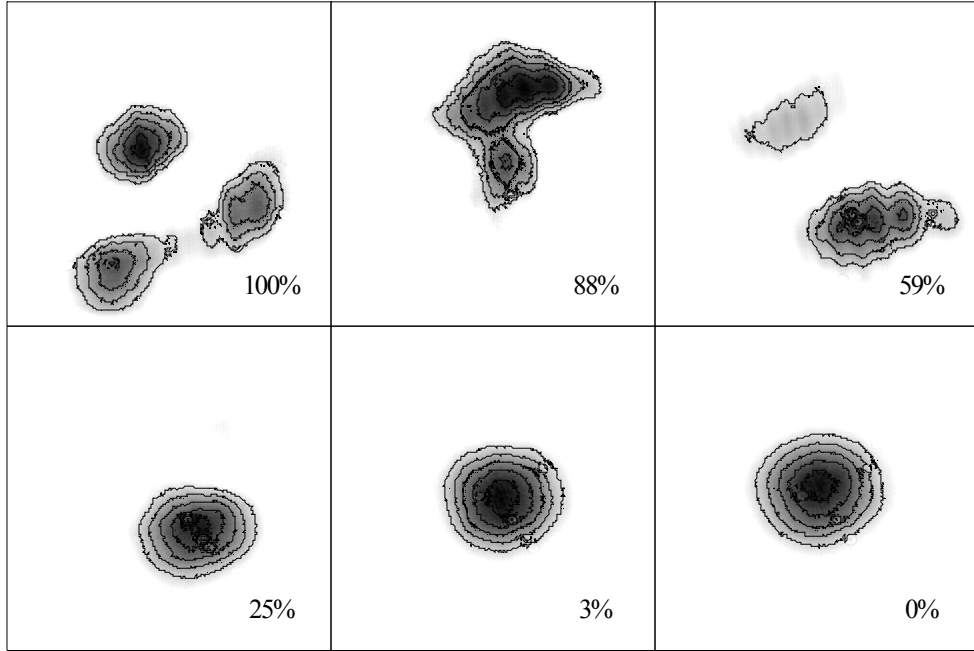


Figure 22: Stokes beam shapes at various levels of Stokes coupling into the back end of the fiber.

For high cavity quality, the ring cavity experiment verified the results of Choi [42] and beam cleanup was not observed. The beam quality, as given by Equation (4.14), is tabulated below. Both the intensity distribution and the tabulated data suggest an improvement in the quality of the beam as the amount of Stokes seeding is reduced.

Table 2: Beam quality factors for ring cavity SBS experiment.

| SBS Feedback                                    | 100%        | 88%         | 59%         | 25%        | 3%            | 0%            |
|---|-------------|-------------|-------------|------------|---------------|---------------|
| Variance of Gaussian Fit ( $10^{-6}$ ) - $\chi$ | $113 \pm 5$ | $62 \pm 20$ | $50 \pm 17$ | $17 \pm 7$ | $6.1 \pm 0.4$ | $4.3 \pm 0.3$ |
| Relative Fit                                    | 26.3        | 14.4        | 11.6        | 4.0        | 1.4           | 1             |

When very little of the Stokes beam was coupled back into the fiber, the beam spot appeared to have a Gaussian intensity distribution, yet the benefit of that slight seeding to the overall Stokes power is not readily measured from this data. To quantify the benefit

of the seed beam, the power in the Stokes beam was measured as a function of the half-wave-plate angle. The experiment was set up in response to the images observed in Figure 22 but after the original experiment had been disassembled, so the specific images of the Stokes beam cannot be directly correlated to the effect on the Stokes power. On the other hand, the experimental schematic was virtually identical so there is no reason to expect that the Stokes spatial quality would be significantly different. The result of this measurement is plotted in Figure 23. This data shows that even a relatively small Stokes seed results in a drastic increase in the Stokes output, but it contributes no information about whether the improvement is due to an increase in slope efficiency or a reduction in threshold. Comparing it to the spatial quality of the Stokes beam indicates that it is likely that most of the benefit of a seed could be obtained while maintaining a relatively clean Stokes beam.

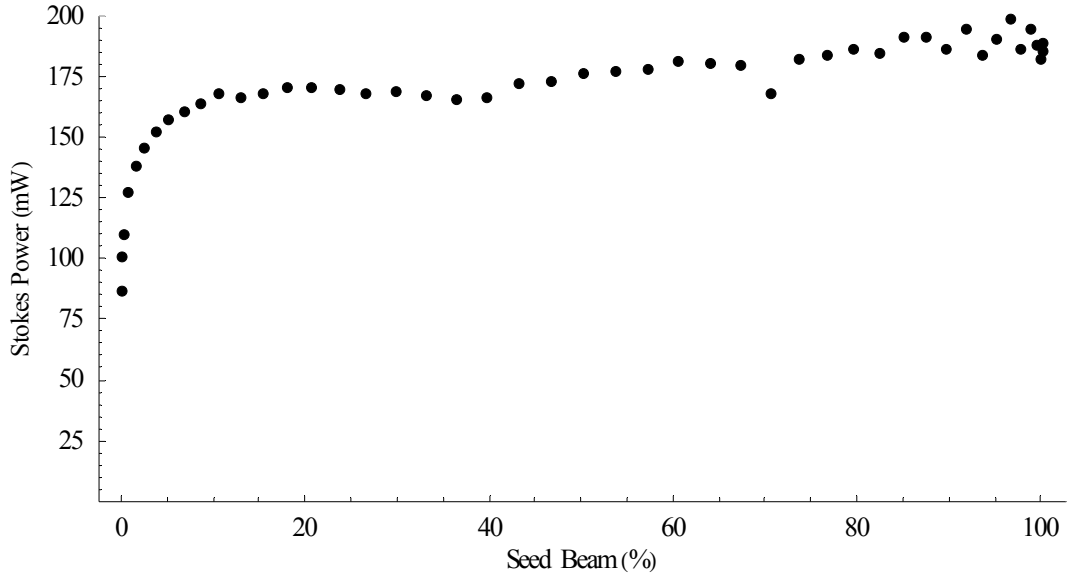


Figure 23: Stokes output at various levels of Stokes coupling into the back end of the fiber.



In the experiments described above, the Stokes beam was deliberately coupled into multiple fiber modes. A representative sample of the coupled seed beam is shown in Figure 24. Since it is unlikely that the power is uniformly distributed over all of the fiber modes, this preferentially enhances certain modes, invalidating the beam cleanup modeling described in Section 4.2. However, if the ring cavity was designed such that the LP<sub>01</sub> mode at the front end of the fiber was re-imaged at the back end of the fiber, beam cleanup should be observed regardless of how much of the Stokes beam is coupled back into the fiber. Ensuring the Stokes is injected into the fiber in the pure LP<sub>01</sub> mode can be done using a number of techniques [36, 43].

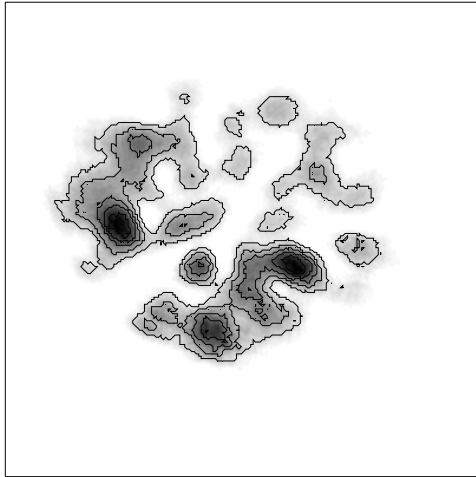


Figure 24: Beam shape of the coupled Stokes power in the ring cavity setup.

#### 4.4. Conclusions

Throughout this chapter, beam cleanup in a long, 50-micron, graded index fiber was analyzed. As described in Section 4.3.1 the spatial intensity distribution was clearly altered when aberrated pump beam was coupled into a fiber. The beam quality was quantitatively analyzed, confirming that the Stokes beam quality was a factor of 18.2

better than the incident pump and 9.1 times better than the coupled pump beam. The beams were also analyzed qualitatively. The reflected pump and transmitted pump beams were highly aberrated with clear intensity fluctuations across the image, whereas the Stokes beam had a smooth Gaussian-like intensity distribution.

This section also investigated the efficiency of the beam cleanup process. It was found that the efficiency drops dramatically when the pump beam is not coupled directly into the center of the fiber. Thus a highly aberrated pump beam is not converted into a Stokes beam as efficiently as one that perfectly matched the LP<sub>01</sub> fiber mode. The results indicate, however, that the region near the center of the fiber that must be pumped to efficiently excite a Stokes beam, is a function of the pump power. Thus for aberrated pump beams significantly above SBS threshold, the efficiency of beam cleanup is expected to be greater than that of a spatial filter, which blocks the aberrated portion of the pump beam.

In Section 4.3.2, the polarization properties of the Stokes beam were analyzed. In contrast to the reflection properties of a planar mirror, it was experimentally shown that the Stokes beam propagates in the same polarization state as the pump beam. This was also modeled theoretically. By assuming both the  $x$ - and  $y$ -components work together to generate a single density perturbation in the fiber, the observed polarization properties of the Stokes beam were predicted. Additionally, the model allowed for an estimate of the maximum fiber length that would be expected to maintain the same polarization characteristics. For a pump beam propagating in the highest order fiber mode and the Stokes beam propagating in the LP<sub>01</sub> mode, the Stokes polarization could be maintained

for nearly 3km. However, the approximations made in the model underestimate the actual allowed fiber length, thus the Stokes beam is expected to maintain the polarization of the pump beam in fibers that are in fact much longer.

The modeling described in Section 4.2 demonstrated that it should be possible to generate a Stokes beam in higher order fiber modes through careful pumping conditions. The results presented in Section 4.3.3 show that, although infrequent, this is true. A Stokes beam propagating in the LP<sub>11</sub> mode was observed. When a second laser simultaneously pumped the fiber at the same frequency, the LP<sub>11</sub> mode was lost and power from both lasers was observed in the LP<sub>01</sub> mode. This provided strong evidence that mode competition occurs in the fiber.

Finally, the feasibility of using a Stokes seed to increase the efficiency of SBS beam cleanup was examined in Section 4.3.4. Feeding a portion of the Stokes beam back into the rear end of the fiber provided the seed. When the Stokes feedback was strong, the beam cleanup characteristics of SBS were lost. In contrast, when the feedback was kept low, it appeared that the SBS efficiency could be increased while still cleaning the aberrated pump beam.

## *5. SBS Beam Combining*

### **5.1. Background**

SBS beam combining has been investigated for many years. As in the case of beam cleanup, however, these approaches typically require a high quality source that can be amplified. In one scenario, a single beam is split into several arms. Each arm is separately amplified, phase conjugated, sent back through the amplifier, and recombined. In this arrangement, each Stokes beam starts from a different noise photon thus the beams are not temporally coherent with respect to one another. To eliminate this effect, the beams can be conjugated in the same SBS medium so that they grow from the same seed photon [4-8].

Another method to ensure that each beam is coherent with respect to the others is to generate a Stokes beam that can be used to seed each arm of the setup. This way the different arms do not rely upon noise photons to initialize process and each arm will be coherent with respect to the others. This has the added benefit of reducing the threshold for SBS. Unfortunately, the phase conjugation fidelity is reduced if the seed beam becomes too powerful [44].

Rodgers took a very different approach to beam combining that is akin to the beam cleanup found in the preceding chapter. It is this approach that forms the basis of the research examined in this chapter. Since a single pump beam produces a Stokes beam in the LP<sub>01</sub> mode, two pump beams in the same fiber should produce two Stokes beams, both propagating in the LP<sub>01</sub> mode. Thus two spatially distinct pump beams could

generate two spatially coherent Stokes beams. Rodgers demonstrated this experimentally. He split a pump beam such that half the power traveled one path and the other half traveled a different path into a single fiber. The resulting Stokes beams were shown to be spatially coherent [9]. This experiment was limited by the laser source used. The overall power of the pump laser was relatively low, thus beam combining could not be examined in a highly multimode fiber. Additionally, the laser frequency drifted, precluding any significant examination of combining two different lasers at the same frequency.

This chapter builds upon the results of Rodgers and Chapter 4 with an investigation into spatially combining two laser beams using SBS. In Section 5.2, two beams at the same frequency are combined. Initially, the two beams originate from different lasers to demonstrate that they could work together to produce the Stokes beam. This was followed by experiments in which the two beams originate from the same laser, simplifying the investigation into the characteristics of the spatial combining by eliminating the added complexity of ensuring the laser frequencies do not drift apart. In Section 5.3 the results of experiments combining two beams at different frequencies are explained. Similar to Rodger's research, most of this experiment is limited to fibers with small core diameters, but the results still clearly show that the two beams can be spatially combined.

## 5.2. Coherent Combining

Coherent combining is the process of combining two beams at nearly the same frequency. It requires that both beams work together to generate a single density

perturbation in the fiber, thus their frequencies must fall within a single SBS gain bandwidth,  $\sim$ 100 MHz [45]. Since both pump beams work together, the overall efficiency can be higher than that of two beams combined incoherently. Additionally, the Stokes beam is much more spectrally pure and will therefore have a much longer coherence length. A number of different experiments are described in this section that examine the properties of two pump beams that are coherently combined. In Section 5.2.1, the coupling between the two pump beams are examined to demonstrate their mutual interaction that results in a temporally coherent Stokes beam. The polarization properties of the Stokes beams are examined in Section 5.2.2, verifying the predictions of the model described in Section 4.3.2. In Section 5.2.3, a single laser is split into two paths and recombined. The quality of this combining is characterized both qualitatively as well as quantitatively. The section also describes how the beam combination is affected by the position of the pump beams on the front fiber facet. Finally, conclusions about coherent combining of two laser beams are discussed in Section 5.2.4.

### *5.2.1. Two laser coherent combining*

#### Experimental Setup

Coherent beam combining was investigated using the setup shown in Figure 25. The power generated by two Lightwave Electronics Nd:YAG lasers was independently controlled with half-wave-plates and polarization beam splitters. One of these beams was then amplified by two passes through a Nd:YAG rod. The two beams were then nearly spatially combined using a polarization beam splitter and coupled into a 50-micron, 4.4 km, graded index fiber. A portion of the scattered beam was reflected off a plane parallel plate oriented at near normal incidence to the beam. A scanning Fabry-Perot

interferometer monitored the frequencies of the two beams to ensure they were close enough for coherent combining. The power of the Stokes beam was also monitored as a function of the power of both pump beams.

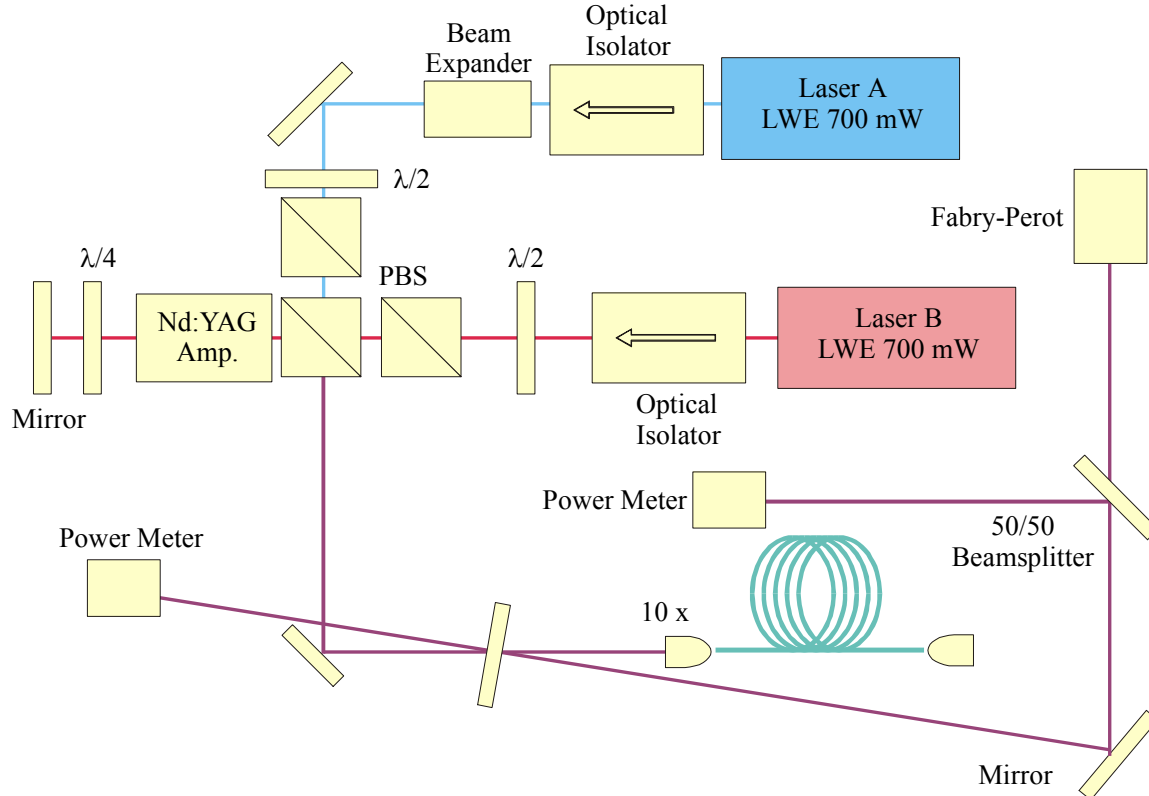


Figure 25: Two beam coherent combining schematic.

## Results

The mutual interaction of the two pump beams in a single fiber is clearly shown using the output of both the Fabry-Perot and the power meter. Two Fabry-Perot scans are shown in Figure 26. The top trace shows the Stokes output generated by the two lasers when their frequencies are separated by approximately 400 MHz. This is more than four times the Brillouin gain bandwidth, thus two individual Stokes beams are generated. The scaling along the vertical axis is arbitrary. However, it is a good measure of the relative

power in each of the Stokes beams and does not change from the top Fabry-Perot scan to the bottom scan. The heights of the two beams seen in top image are 30 and 31. In the bottom image, the frequencies of the pump beams were tuned to overlap, thus only a single Stokes beam is observed. Additionally, the Stokes beam relative power, 100, is found to be more than the incoherent addition of the two individual pump beams, 61. This synergy is a result of the two beams working together to form the Stokes output.

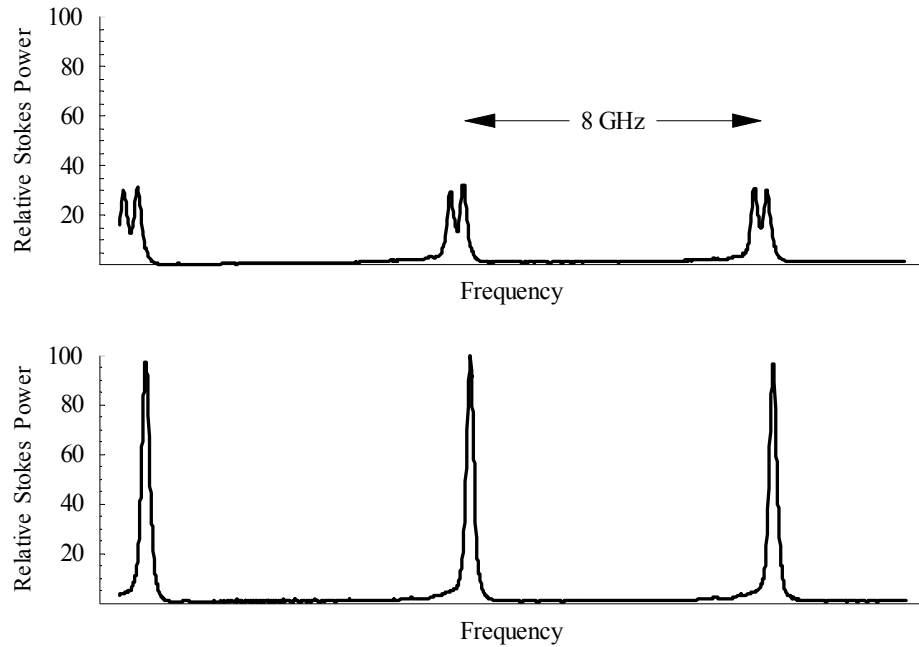


Figure 26: (Top) Scanning Fabry-Perot interferometer output when the pump beams are separated by more than the Brillouin gain bandwidth. Relative peak output of the Stokes beams is  $\sim 30$ . (Bottom) Interferometer output when the pump beams are tuned to the same frequency. Peak relative output is 100, more than twice that of each laser alone.

Coherent combining was also examined using the measured Stokes power as a function of the input beam powers. This data is shown in Figure 27, illustrating that the two pump beams collaborate to produce a single Stokes beam. Figure 28 shows the Stokes power generated along the path indicated in bold on the surface plot of Figure 27.

Initially, the power of the second laser is held at zero, while the first laser is increased to its maximum power. For the second leg of the path, the first laser is held at maximum power and the second laser is increased to its maximum power. This path is insightful because it shows that while the first laser had to overcome a threshold before it began to contribute to the Stokes beam, the second laser does not and contributes to the Stokes beam immediately. This is a direct result of the mutual interaction between the pump beams. The difference in slope efficiency for the two lasers will be explained in Section 5.2.3.

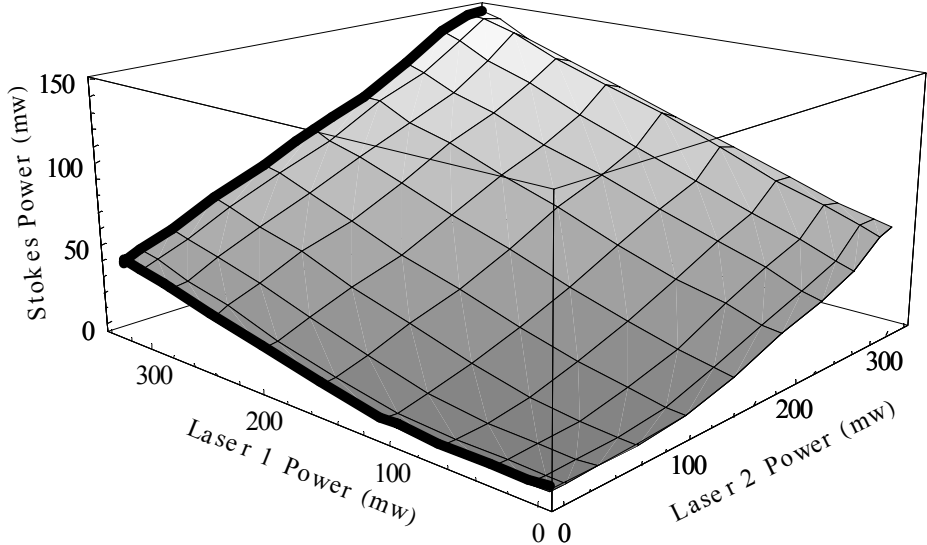


Figure 27: Stokes power as a function of the pump powers.



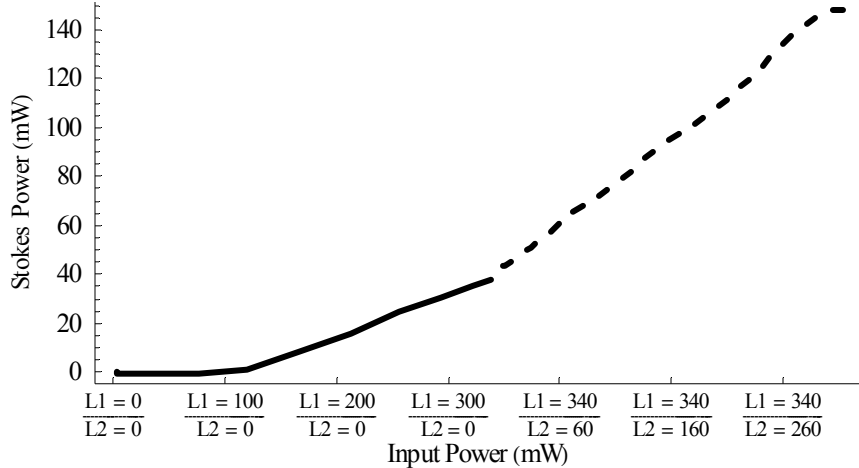


Figure 28: Stokes power generated along the bold path shown in Figure 27.

### 5.2.2. *Polarization properties*

#### Experimental Setup

The polarization properties of the coherently combined Stokes beam were investigated using an experimental setup very similar to that shown in the previous section. The only significant variation is in the tools used to analyze the reflected beam. The power meter, 50/50 beamsplitter, and Fabry-Perot were replaced by a quarter-wave-plate, half-wave-plate, analyzer, and a power meter arranged in the configuration shown by Figure 29. From this configuration, a complete description of the beam polarization was ascertained through a series of measurements at various quarter-wave- and half-wave-plate angles. These angles correspond to measuring specific polarization components of the Stokes beam and are tabulated below (Table 3). From these measurements, the Stokes parameters were calculated using the relationships in Table 4 [46]. The measurements were repeated for each power level shown along the bold path of Figure 27.

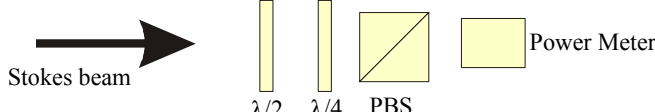


Figure 29: Polarization analysis setup.

Table 3: Measured polarization components.

| $\lambda/2$ angle (°) | $\lambda/4$ Angle (°) | Polarization Component | Label |
|-----------------------|-----------------------|------------------------|-------|
| 0                     | 0                     | Horizontal             | H     |
| 45                    | 0                     | Vertical               | V     |
| 0                     | 45                    | Right Hand Circular    | RHC   |
| 45                    | 45                    | Left Hand Circular     | LHC   |
| 22.5                  | 45                    | Linear @ 45°           | $L^+$ |
| -22.5                 | 45                    | Linear @ -45°          | $L^-$ |

Table 4: Conversion from the measured values to Stokes parameters.

| Stokes Parameter | $S_0$  | $S_1$   | $S_2$       | $S_3$       |
|------------------|--|---------|-------------|-------------|
| Equation         | $\frac{1}{3}(H + V + RHC + LHC + L^+ + L^-)$ | $H - V$ | $L^+ - L^-$ | $RHC - LHC$ |

## Results

The experimental results were analyzed to determine if the coherently combined beams follow the modeling described in Section 4.3.2 for a single pump. In this model, the  $x$ - and  $y$ -components of the Stokes beam were treated independently except to ensure that they reflect off the same density perturbation in the fiber. The experimental setup is well suited for this analysis because the two pump beams are orthogonally polarized. Thus the polarization model predicts that the horizontally polarized pump would only contribute to the horizontally polarized Stokes beam and vice versa. The measurements are consistent with this theory and are shown in Figure 30. While the power of the first laser is increased, the Stokes beam is predominantly horizontally

polarized. Likewise when the power of the second laser is increased, the Stokes beam gains a strong vertical component.

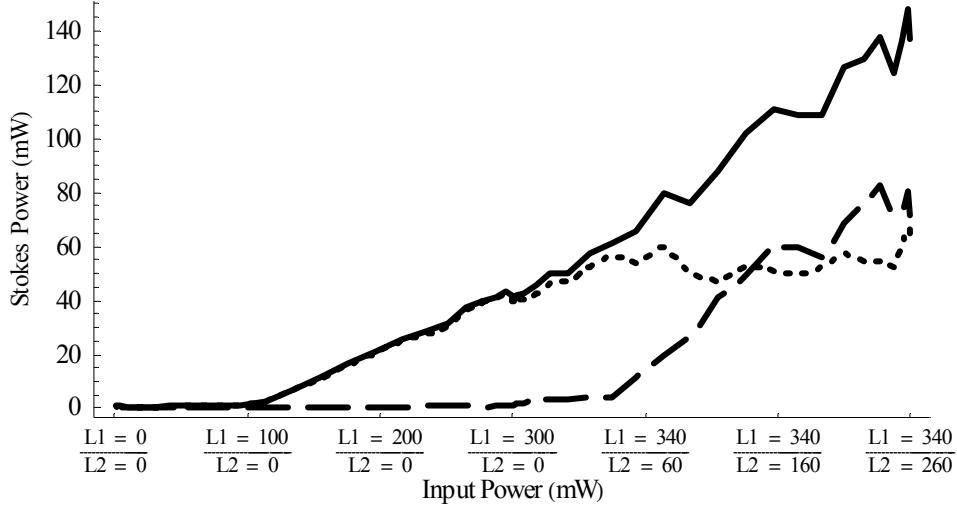


Figure 30: (solid) Total Stokes power as a function of the pump power along the path indicated in bold on Figure 27. (dotted) Horizontally polarized Stokes power as a function of pump power. (dashed) Vertically polarized Stokes power as a function of pump power.

While the magnitudes of the vertical and horizontal components of the beams are easily observed, they do not form a complete description of the polarization of the Stokes beam. A ~~com~~plete description is only determined when the phase difference between the two components is known. However, since the two pump beams are created by separate oscillators, each with a linewidth of  $\sim 5$  kHz, the polarization of the pump beam is expected to randomly shift in time. Even if the center frequencies of the two beams are perfectly aligned, there will be a change in polarization on a time scale of  $1/\sqrt{5\text{kHz}} = 200\mu\text{s}$ . The coherence time will be even shorter if the pump beam frequencies do not overlap perfectly. The degree of polarization,  $V$ , takes into account the random shifts in polarization. It is defined in terms of the Stokes vector as [46]

$$V = \frac{\left(S_1^2 + S_2^2 + S_3^2\right)^{1/2}}{S_0}. \quad (5.1)$$

If the polarization of the beam does not change in time, this equation is identically equal to one. On the other hand, if there are random fluctuations in the polarization, the degree of polarization drops.

Using the definitions for the elements of the Stokes vector in Table 4 and assuming that the phase difference between the horizontal component (laser 1) and vertical component (laser 2) of the total pump beam is random, the degree of polarization for the pump beam is

$$V = \frac{|H - V|}{H + V}. \quad (5.2)$$

This theoretical value is represented by the dotted line in Figure 31.

As described in Section 4.3.2, the phase difference between the  $x$ - and  $y$ -components of the pump beam is conserved after Brillouin reflection. Thus the Stokes degree of polarization should mimic that of the pump. The solid line of Figure 31 shows the degree of polarization of the Stokes beam as calculated using the measured Stokes vectors. As soon as the reflected power in the first laser is detectable, the degree of polarization is relatively high. However, when the second laser is turned on, the degree of polarization drops, consistent with that of the pump beam.

All of the experimental evidence agrees with the trends predicted by the polarization model described in the previous chapter. However, the experiments described in this section cannot definitively prove that the polarization of the Stokes beam was identical to

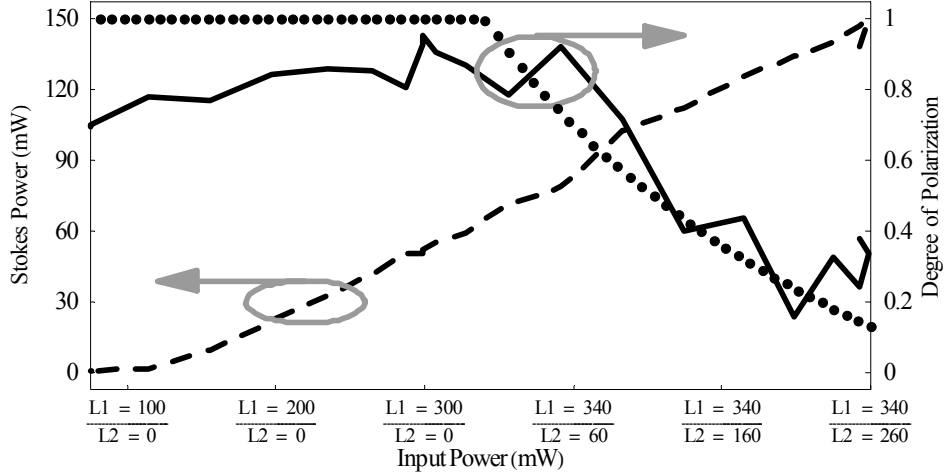


Figure 31: The degree of polarization (solid line) falls off rapidly as the second laser begins to pump the fiber, contributing to the overall Stokes output. This is relatively consistent with the predicted degree of polarization of an idealized pump beam (dotted line). The total reflected Stokes power rises linearly above threshold regardless of the polarization states of the pump beams (dashed line).

that of the pump beam. In fact, when only a single laser pumped the fiber, the pump beam was nearly 100% polarized, but the Stokes beam was found to be approximately 80% polarized. It is believed that this discrepancy was caused by power fluctuations in the Stokes beam. The measurement of the Stokes parameters required six independent power measurements. Any change in the Stokes power from one of these measurements to another would result in a reduced degree of polarization. This limitation in the experiment could be remedied by a better sample of data points. Unfortunately, that would require laser frequency stability over a longer time frame.

### 5.2.3. Spatial characteristics

#### Experimental Setup

Two lasers were critical to determine the characteristics of the Stokes beams described in Sections 5.2.1 and 5.2.2. However, ensuring coherent combination was difficult because the laser frequencies slowly drifted out of resonance with each other.

To eliminate this problem, the remaining experiments were completed with a single laser split into two independent paths. This allowed for a clear demonstration of beam combining and an accurate measurement of the combining efficiency as a function of the pump spatial position.

A schematic of the experiment used to investigate the spatial characteristics of coherent combining is shown in Figure 32. The beam from a 700 mW laser with an instantaneous spectral width  $\sim$ 5 kHz was amplified by a Nd:YAG amplifier and split using a polarization beam splitter into two paths. The beams were then nearly spatially combined using a second polarization beam splitter, and coupled into a 50-micron, 4.4 km, graded-index fiber. To demonstrate beam combining, it was critical that the pump beams were not spatially combined with the polarization beam splitter. Thus the beams were spatially separated by as much as possible while still ensuring that they were coupled into the fiber. After reflection by the fiber, a portion of the beam was observed with a CCD camera while a Fabry-Perot and a power meter were used to determine the spectrum and relative power of the Stokes beams.

Several measurements of the reflected beams were taken with the CCD camera to determine the degree of spatial coherence in the Stokes beams. First, images of the Stokes beams generated by each path were collected. These depict the relative position of the Stokes beams generated by the two pump beams. Then, without adjusting the front fiber facet, the fiber was cut to be  $\sim$ 2 m long. The shortened interaction length increased SBS threshold well above the power delivered by the two beam paths. Two more CCD images, one for each pump beam, were taken of the Fresnel reflection off the front facet

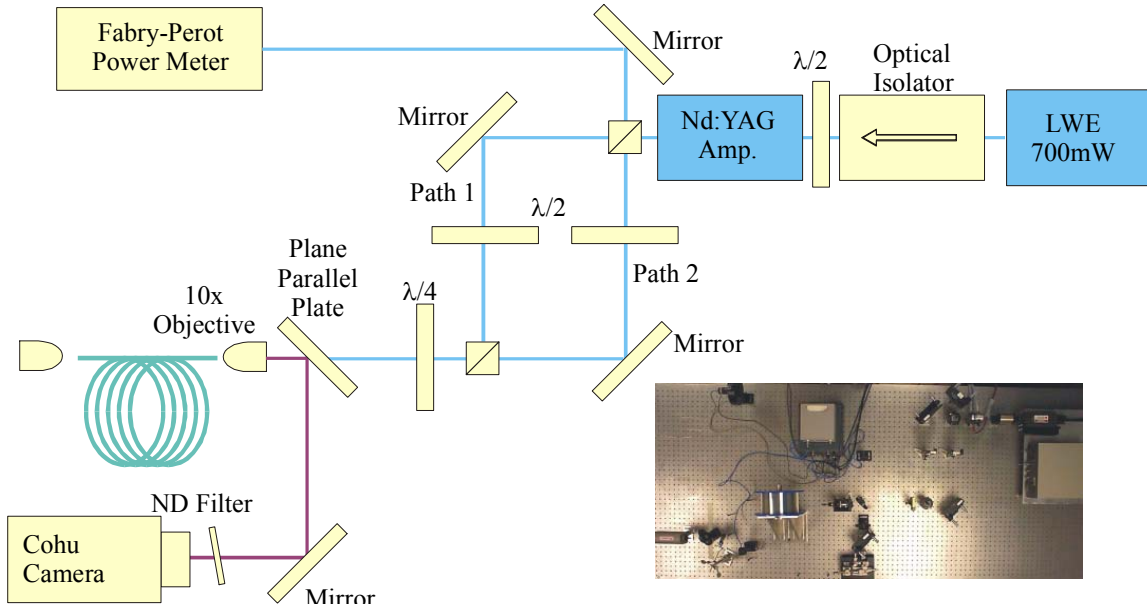


Figure 32: Two beam coherent combining schematic.

of the fiber. These images were used to subtract the contribution of the Fresnel reflection from the images of the Stokes beam, as well as allowed for a measurement of the degree of spatial coherence of the two pump beams. Finally, to ensure that the beams were spatially combined through SBS rather than some other process, such as spatial filtering, the CCD camera was moved to the output end of the 2 m fiber and the two transmitted pump beams were observed.

The beam combining efficiency was also investigated. This was completed in a similar manner to the efficiency measurements described in Chapter 4. While path one was held constant, the second beam was translated along the front fiber facet by rotating the mirror in this path. At each point, the Stokes power was measured at the CCD camera and an image of the Stokes beam was collected. The Stokes beam was much stronger than the reflected pump beam, thus the pump beam was not noticeable in the images. In order to determine the location of the pump beam on the fiber, the long fiber

was again cut to ~2 meters and the position of the pump beam observed. This also allowed for a measurement of the transmitted power and hence a determination of the fiber core size.

### Results

The results of the coherent beam combining experiment are shown in Figure 33-  
Figure 35. In each figure, part (a) is an image of the relative beam intensity due to the beam injected from the first path. In this image, darker shades indicate higher intensities. The total area under the intensity distribution is normalized to one, which eliminates fluctuations from one image to the next due to differences in the power. The second image in each figure, part (b), shows the relative beam intensity due to the second path. In this image, lighter shading indicates higher intensities and again the area is normalized to account for power fluctuations. Finally, part (c) is the combined image of parts (a) and (b). It represents the pixel-by-pixel subtraction of the intensity of one path from the other. Keeping the convention of parts (a) and (b), dark regions indicate a higher concentration of power due to the first path and brighter regions indicate a higher intensity due to the second path. Gray areas result when there is equal power from each path.

Figure 33 indicates the relative positions of the pump beams. Interpreting part (c) as described above, clearly shows that the overlap of the two beams is insignificant. It can be inferred from this picture that the pump beams are not coaxial before entering the fiber. The relative positions of the transmitted beams are shown in Figure 34. The structure in this figure demonstrates that even though there is some overlap, the beams

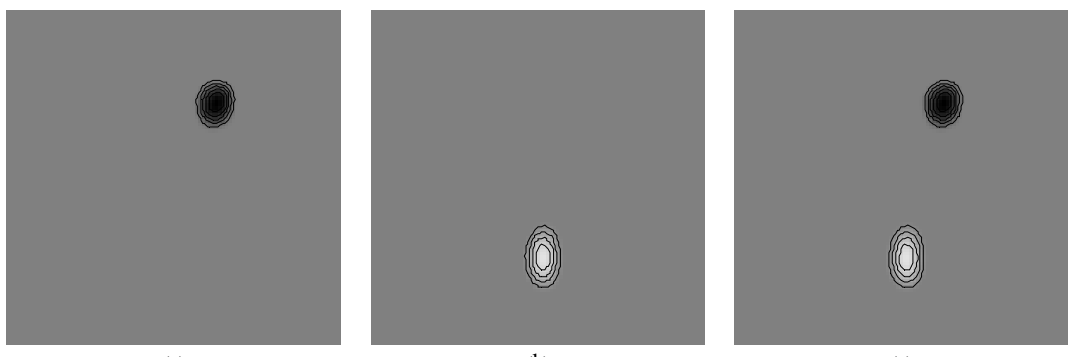


Figure 33: Images of the pump beams from each path. a) The pump beam from path 1 (high intensities are indicated by dark regions). b) The pump beam from path 2 (high intensities are indicated by bright regions. c) Image of both pump beams.

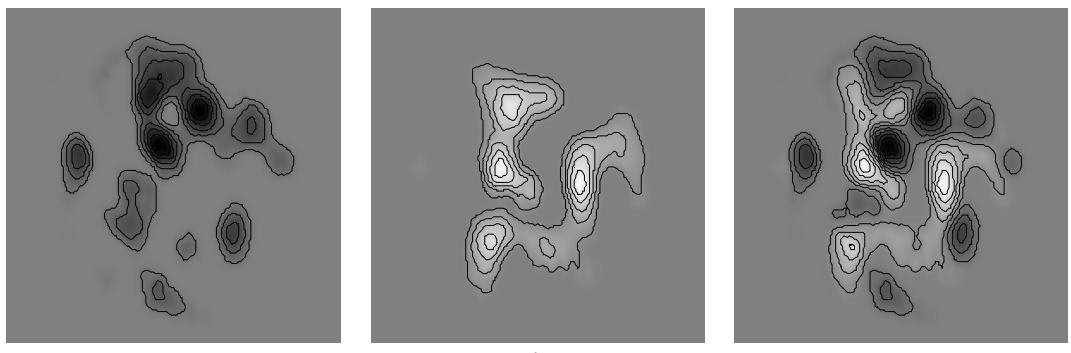


Figure 34: Images of the transmitted beams from each path. a) The transmitted beam from path 1 (high intensities are indicated by dark regions). b) The transmitted beam from path 2 (high intensities are indicated by bright regions. c) Image of both transmitted beams.

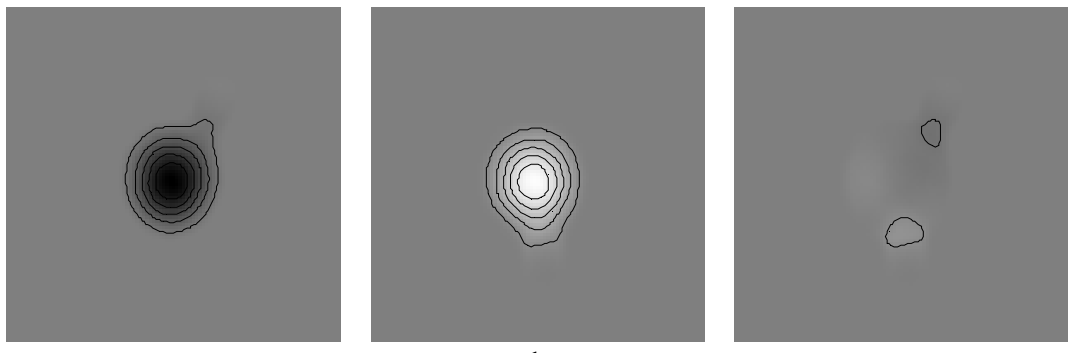


Figure 35: Images of the Stokes beams from each path. a) The Stokes beam from path 1 (high intensities are indicated by dark regions). b) The Stokes beam from path 2 (high intensities are indicated by bright regions. c) Image of both Stokes beams.



are not spatially combined upon entering the fiber. Finally, Figure 35 shows the Stokes beams generated by each path. Part (c) of this figure shows very little structure, representing the fact that the two paths generate nearly identical Stokes beam shapes.

A more formal analysis of the beam combining results was developed to quantify how well the beams were combined. This analysis uses the mean square error between the normalized intensity from path 1 and the normalized intensity from path 2. This is defined by

$$\frac{1}{N} \sum [I_A(x_i) - I_B(x_i)]^2. \quad (5.3)$$

$I_A$  and  $I_B$  represent the intensity of each path over the range of pixels in the image, and  $N$  is the total number of pixels. The results of these calculations are shown in Table 5. The Stokes beams are found to have a misalignment that is about 15 times lower than the transmitted beams and over 500 times lower than the pump beams.

Table 5: Misalignment calculation

|   | Pump | SBS  | Transmitted |
|---|------|------|-------------|
| $\frac{1}{N} \sum [I_A(x_i) - I_B(x_i)]^2 (10^{-10})$ | 3270 | 5.98 | 91.8        |
| Relative Misalignment                                 | 547  | 1    | 15          |

A similar analysis was completed using aberrated pump beam for each input. In this experiment, both pump beams propagated through a piece of Saran wrap before coupling into the fiber. The results support the same conclusions as above, but were not as dramatic for several reasons. First, scattering off the Saran wrap reduced the power coupled into the fiber, thus making the ratio of Stokes power to pump Fresnel reflection

lower. Secondly, as will be shown in the following pages, the lowered power required the pump beams to be closer together to excite the Stokes beams. Finally, the aberrations on the beams increased their physical size, causing greater overlap of the input beams.

When the pump beams are not coupled into the center of the fiber core, the combining efficiency suffers. Figure 36 shows the relative Stokes power as the path-two pump beam was moved from one side of the fiber to the other. The top of the figure shows the position of the pump relative to the Stokes beam for three of the data points. As the figure shows, the efficiency has a form similar to that observed for beam cleanup. This implies that although the contribution from power near the edge of the fiber will be low, all power coupled into the fiber will contribute to the Stokes beam.

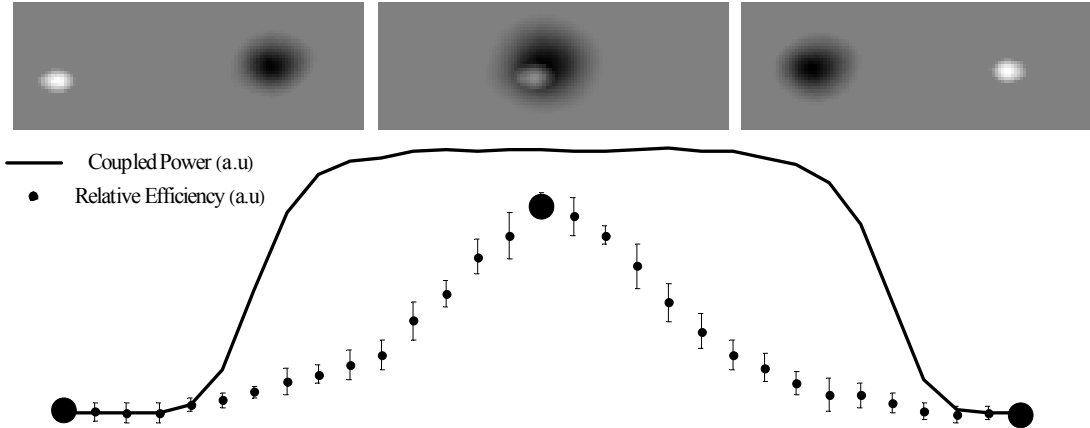


Figure 36: (Top) Stokes beam (black) as a function of the position of the path-two pump (white). (Bottom) Relative SBS efficiency as a function of the path-two beam position. The power coupled into the fiber is shown by the solid line.

#### 5.2.4. Conclusions

As the data has shown, coherent beam combining is possible using stimulated Brillouin scattering. In Section 5.2.1, the two pump beams were shown to mutually



excite the fiber when their frequencies overlapped. This resulted in a Stokes beam at a single frequency and a higher Brillouin reflection coefficient than when the pump beams operated independently.

The polarization characteristics of the Stokes beam were examined in Section 5.2.2. The results of this measurement indicated that the pump beams retain their original polarization after Brillouin reflection. This was demonstrated through a measurement of the components of the Stokes beam that were co- and cross-polarized with respect to each pump beam. Additionally, the total pump beam degree of polarization was found to match that of the Stokes output relatively well. This was expected based upon the polarization model described in the previous chapter.

Finally, in Section 5.2.3, it was shown that when two beams were coupled into the fiber at different positions and angles, the resulting Stokes beams have the same frequency and are spatially combined. The efficiency of the process was shown to mimic that of a single aberrated beam with two lobes. When coupled into the center of the fiber, the efficiency was greater than when the pump was coupled into the edge of the fiber.

### **5.3. Incoherent Combining**

As described in the previous chapter, in order for two beams to coherently combine, the frequencies of both beams must fall within a single Brillouin gain bandwidth. Even in a laboratory setup under ideal conditions, this can be difficult to obtain for two independent lasers. Scaling this solution to even more beams could become prohibitively complex. On the other hand, if each pump laser operates at a different frequency, they will excite independent Stokes beams in the fiber [45, 47-49]. Each of these Stokes

beams should be a cleaned version of the pump and is expected to propagate in the  $LP_{01}$  mode. Thus the spatially incoherent pump beams would produce spatially coherent Stokes beams. Because the Stokes beams are each excited at different frequencies, they are temporally incoherent with respect to one another. Thus this is referred to as incoherent beam combining.

Incoherent beam combining can be used to scale beam power to higher levels than those achievable through coherent beam combining. If one were to coherently combine many lasers into a single beam, the resulting Stokes wave would eventually reach second order SBS threshold, resulting in decreasing efficiency with increasing input power. While this is not expected to be a severe limitation, at some point, its effect would have to be considered. Incoherent combining would relax this limitation significantly. For the incoherent process, each Stokes beam is produced independent of the others, thus the second order threshold is dependent on the power in each Stokes beam, not the total Stokes power and second order Stokes threshold will be greater than that for a single coherent beam by a factor of the number of lasers being combined [45].

Moreover, this technique is completely general in that lasers of any wavelength can be combined as long as their wavelengths lie in the transmission window of the fiber materials. This kind of beam combining technique would be useful for any applications that require high brute-force laser power in a single beam such as in material processing. It would also be appropriate for applications that require multiple discrete wavelengths in a single beam, such as in multi-spectral electro-optic countermeasures or hyper-spectral imaging. The spatial coherence that this technique provides makes it possible for the

combined beam to be directed into a diffraction-limited spot, be it a tight focus or long-distance targeting.

The investigation of incoherent beam combining was completed in two parts. In Section 5.3.1, a set of experiments are described that were designed to investigate the mutual interaction of the two lasers in a single fiber. The goal of the experiments was to demonstrate that since the frequency of the two beams are separated by greater than the Brillouin gain bandwidth, they excite independent Stokes waves in the fiber. In Section 5.3.2, the spatial overlap of the Stokes waves generated by the two laser beams is characterized. In this section it is shown that although the pump beams do not overlap, the two Stokes beams have excellent spatial overlap. The spatial coherence of the Stokes beams is examined in Section 5.3.3. In this experiment, the Stokes beam is split and travels two paths to a CCD camera. The interference of the two beams is then analyzed as the paths change. Finally, conclusions concerning incoherent beam combining are presented in Section 5.3.4.

### *5.3.1. Independent excitation*

#### Experiment

The setup used to demonstrate incoherent beam combining is shown in Figure 37. Two SDL single mode (longitudinal) lasers were collimated using 20x microscope objectives. Laser A emitted light at 853 nm while laser B operated at 832 nm. The collimated beams passed through 40-dB Faraday optical isolators and were then spatially superimposed with two half-wave plates and a polarizing beam splitter. At the beam splitter, lasers A and B are polarized horizontally and vertically, respectively. After the

beam splitter, the light passed through a quarter-wave plate oriented to convert the crossed linear polarizations of the two beams into orthogonal circular polarizations. Finally, using a 10x microscope objective, the beams were focused into a 4.4 km, step-index, Corning SMF-28 fiber with an 8.2-micron core and a numerical aperture of 0.12.

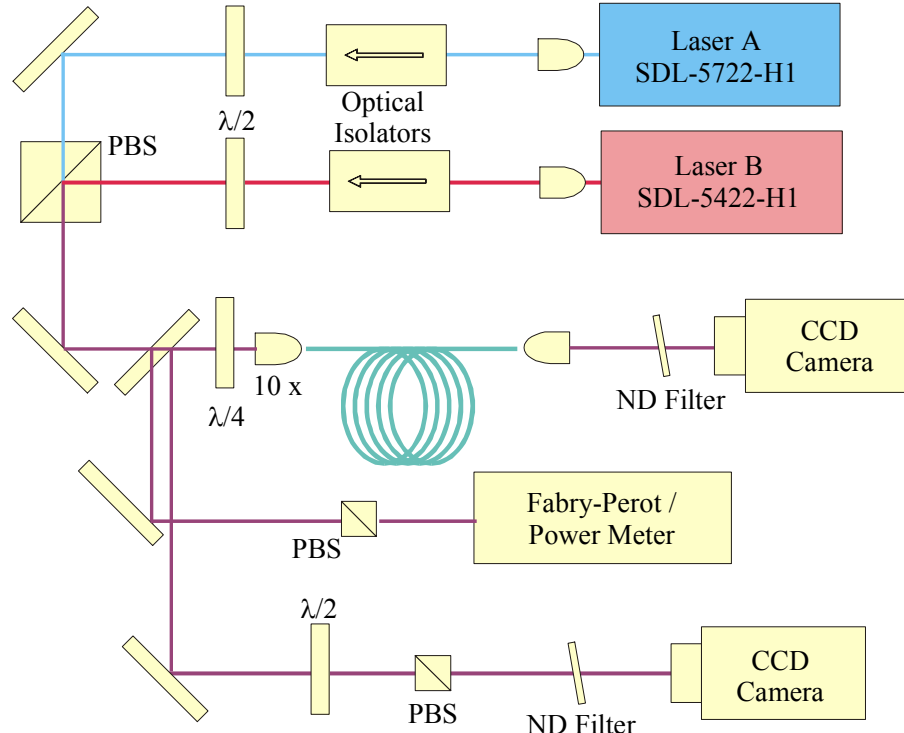


Figure 37: Two beam incoherent combination experimental setup using a multimode fiber.

The light that was reflected off the surface of the fiber by Fresnel reflection as well as the light generated through SBS was collimated as it passed back through the microscope objective and the quarter wave plate. A portion of this reflected off both the front and back surfaces of an uncoated flat window. The fraction of the beam that was reflected off of the rear surface of the flat passed through a half-wave plate, a Glan-Thompson polarizer and neutral density filters before being captured by a CCD camera. The portion

of the beam that was reflected from the front surface of the flat was picked off using a mirror and directed through a Glan-Thompson polarizer into either a Coherent power meter or a Fabry-Perot interferometer for spectral characterization. After monitoring the position of each beam, the fiber was cut ~2 m beyond the front fiber facet and more intensity profiles were collected. These images were used to extract the intensity of the pure Fresnel reflection from that of the Stokes beam since the shortened fiber increased SBS threshold well beyond the power produced by the laser.

### Results

Figure 38(a) shows a 2-D surface plot displaying the power of the horizontally polarized Stokes beam as it enters the Fabry-Perot over all possible input powers for laser A and laser B. The separation of the Fresnel reflection from the Stokes beam was facilitated by the fact that the polarization of the Fresnel reflection is orthogonal to that of the Stokes, as discussed in the previous chapter. Obviously, as the current on laser A increases (thus laser power), the horizontally polarized Stokes beam (co-polarized with the laser A input) increases as well, once threshold is passed. There is no significant change to the Stokes power due to laser A as the power coupled into the fiber from laser B is increased. Figure 38(b) demonstrates that the converse is also true. As the current driving laser B is increased, the power in the vertically polarized beam (co-polarized with the laser B input) increases, independent of the laser A power coupled into the fiber. The combined output of both polarizations is shown in Figure 38(c). If one were to trace out the path along this surface shown by the bold line, distinct threshold powers are seen for each laser. This path is plotted in Figure 39, demonstrating that each laser must exceed

threshold in order to excite its own Stokes beam. This behavior contrasts with that seen during incoherent combining when a combined threshold was observed for both lasers (Figure 28).

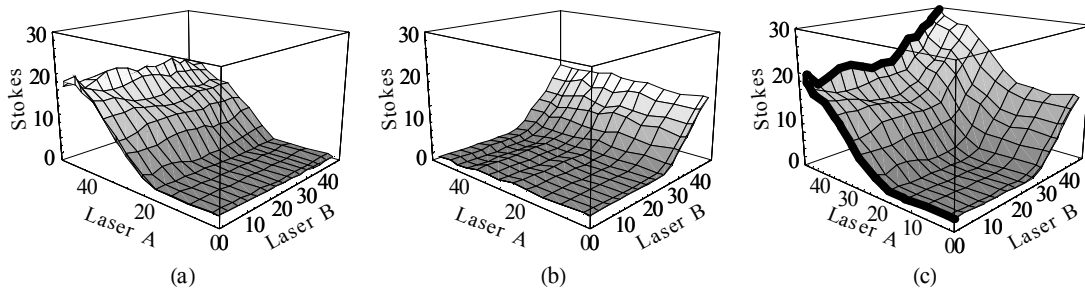


Figure 38: Polarimetric Stokes Power vs. Pump Power in mW. (a) SBS Power reflected into a horizontally polarized beam. (b) SBS Power reflected into a vertically polarized beam. (c) Total SBS Power.

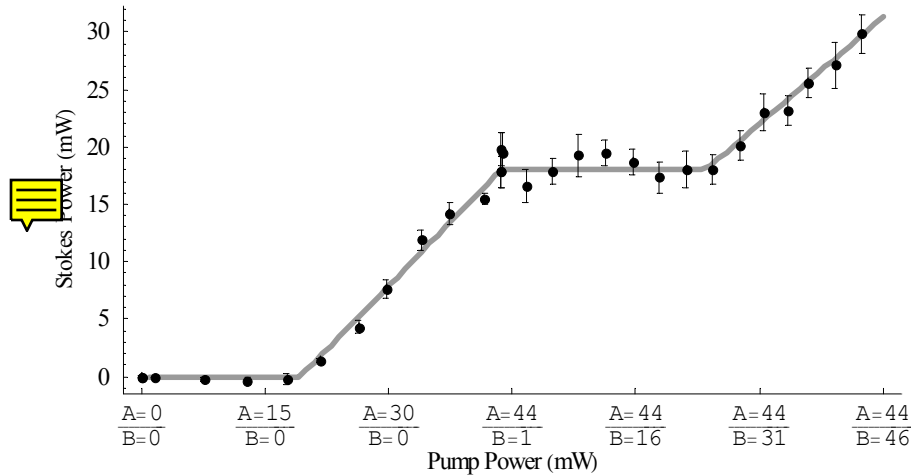


Figure 39: The indicated path of Figure 38(c) shows that the two input beams must each overcome a threshold before contributing to the Stokes beam.

Several slices of Figure 38(c) were taken along both axes, to determine the possible dependence of the SBS threshold for one laser on the power of the other. The slices were normalized such that the left hand side of each slice, corresponding to no cross laser



input, was set to zero. These slices are all plotted using a common axis in Figure 40. The similarity of the curves indicates that the slope efficiency and threshold for each laser is independent of the power in the other laser. Investigating the slices along the laser B axis further (Figure 40(a)) shows that the average slope efficiency of these curves is  $68 \pm 8\%$ , the error margin being one standard deviation. The standard deviation associated with the calculation of each slope efficiency is on average 7%. The average threshold is  $17 \pm 2$  mW. The standard deviation associated with the calculation of the threshold is on average 5 mW. This data shows that the threshold and slope efficiency are nearly identical within the experimental uncertainty over the full range of laser A input powers, indicating the complete independence between the Stokes beam generated by laser B and the power of laser A. The same analysis was completed for the Stokes power generated by laser A, demonstrating no dependence of its threshold and slope efficiency on the power of laser B.

The frequency of all the beams was continuously monitored throughout these measurements with a Fabry-Perot spectrum analyzer. A sample spectrum containing the pumps and their Stokes components is shown in Figure 41. It was observed that the Stokes shift remained constant as the power of both lasers was varied.

The observations described above collectively lead to the conclusion that when two laser beams of arbitrary frequencies simultaneously excite SBS in a common fiber, they individually excite their corresponding Stokes beams without interfering with each other. The simultaneous presence and generation of the Stokes beams by two incoherent pump

beams in a single fiber have no effect on the wavelength, threshold, or efficiency of the Stokes beam generated by each pump.

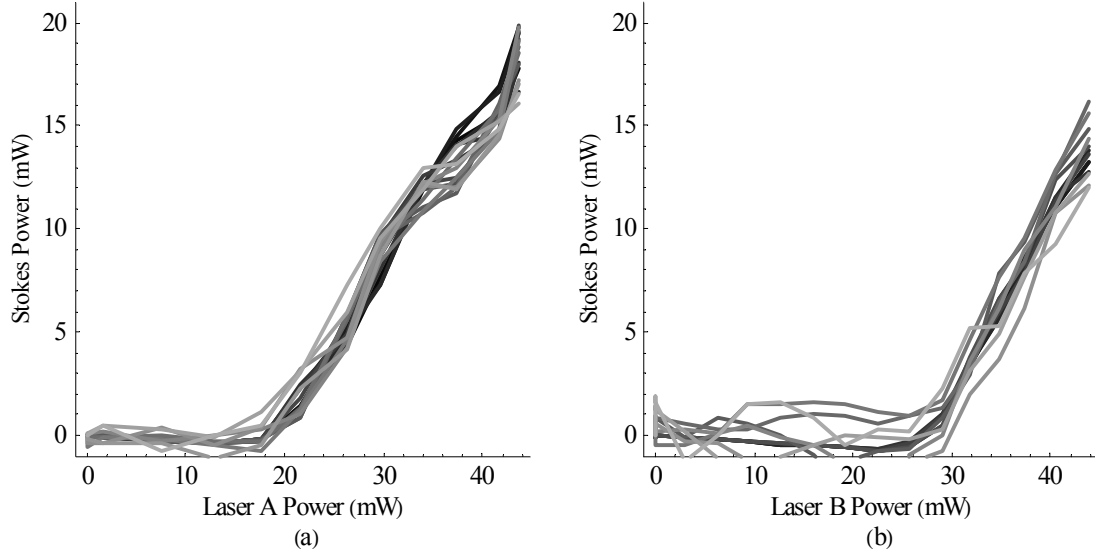


Figure 40: Slices through Figure 38(c) at different values of laser B (A) and laser A (B). Each slice is normalized at the left side. The similarity of each curve indicates that the lasers produce independent Stokes beams.

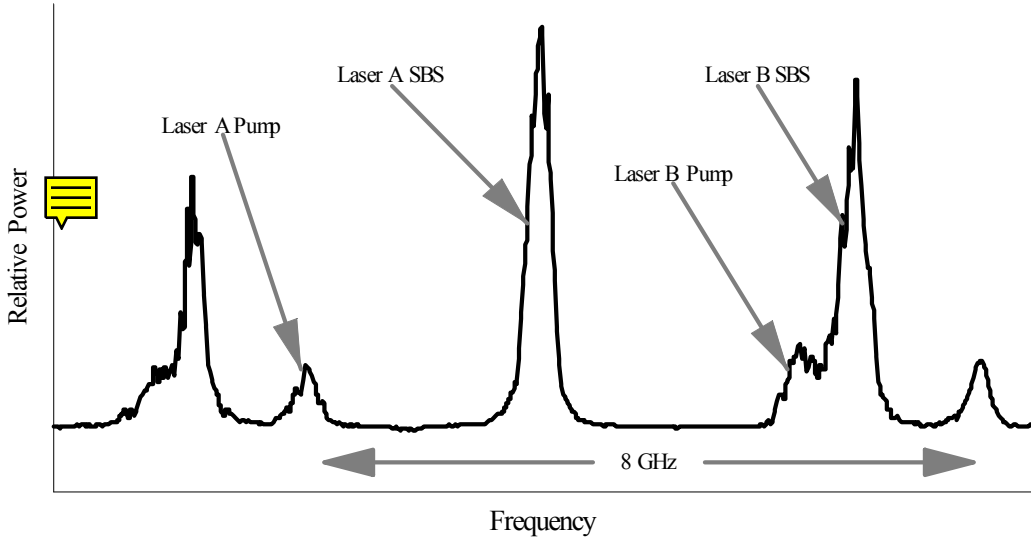


Figure 41: Dual pump and SBS spectrum generated from a Fabry-Perot interferometer with a free spectral range of 8 GHz.

### *5.3.2. Spatial Overlap*

#### Experimental Setup

A set of experiments was performed to investigate the spatial coherence properties of the Stokes beam generated through the incoherent beam combining technique. The goal of the experiments was to demonstrate the near-perfect spatial coherence of the Stokes beams generated in the SBS process by two arbitrary lasers in a multi-mode fiber.

The experimental setup was identical to Figure 37 except the quarter-wave plate was removed. Under such conditions, all light from a single pump (the Stokes beam and the Fresnel reflection) had the same polarization and could be kept separate from the second pump. The Corning SMF-28 fiber used had a fiber parameter of 4.2, indicating that four modes ( $LP_{01}$ ,  $LP_{11}$ ,  $LP_{02}$ , and  $LP_{21}$ ) could be supported by the fiber [50].

The spatial coherence properties were analyzed in the same manner as those for incoherent combining. First, each laser was turned on well above their respective SBS thresholds. The half-wave plate located in front of the beam profiler was tuned for maximum transmission of laser A and the resulting Stokes beam. At that point, eight intensity profiles were captured and averaged. The averaging was necessary due to the temporal fluctuations that accompanied the Stokes beam. This averaged profile consisted of energy in the Stokes beam created by laser A as well as energy that reflected off the front fiber face. The half-wave plate was then rotated  $45^\circ$  and similar images were collected showing the Stokes beam intensity profile due to laser B and its associated pump beam.

Upon completion of the first set of images, the fiber length was cut to two meters from the entrance face. This was done without altering the position of the front face of the fiber or adjusting the camera location. Two more sets of intensity profiles, identical to the first were then collected. However, since the fiber was only two meters long, the SBS threshold was raised well above the operating power of the two lasers. This ensured that the profiles included light due only to Fresnel reflection off the air-fiber interface. These profiles show the relative position of the two input beams and were subtracted from the first set to obtain an intensity profile due purely to the Stokes beam.

The last set of profiles was taken at the exit face of the fiber. Each laser was independently powered when the images were collected. The two profiles clearly show that the input beams were not spatially filtered into the fundamental fiber mode.

### Results

Both the qualitative measure of the beam overlap and the numerical figure of merit used to analyze coherent beam combining were applied to the experimental data. The qualitative measure was a series of grayscale plots that show the relative position and intensity of each laser. The brightness of the plots was calculated using the following algorithm. The intensity image from each laser was separately scanned through a 10 pixel x 10 pixel mean filter. The size of the filter was chosen to be large enough to remove the random noise from the intensity data but small enough to retain real intensity variations present in the images. The power of the beam in each intensity image was then separately normalized to one. The results of this analysis are shown in Figure 42-Figure 44. In each of these figures, (a) shows the intensity profile of laser A, where a brighter

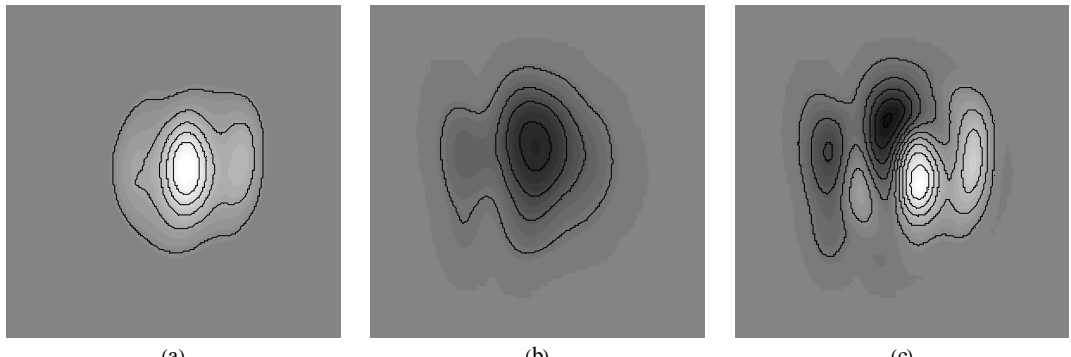


Figure 42: Reflected beam overlap. (a) Image of Laser A. Lighter shades indicate higher intensity. (b) Image of Laser B. Darker shades indicate higher intensity. (c) Combined laser beams showing significant mismatch between the reflected positions of laser A and laser B.

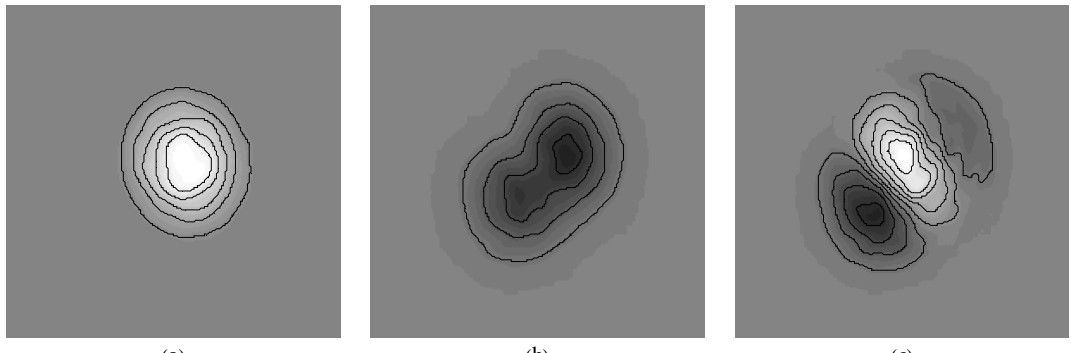


Figure 43: Transmitted beam overlap. (a) Image of Laser A. Lighter shades indicate higher intensity. (b) Image of Laser B. Darker shades indicate higher intensity. (c) Combined laser beams showing significant mismatch between the transmitted positions of laser A and laser B.

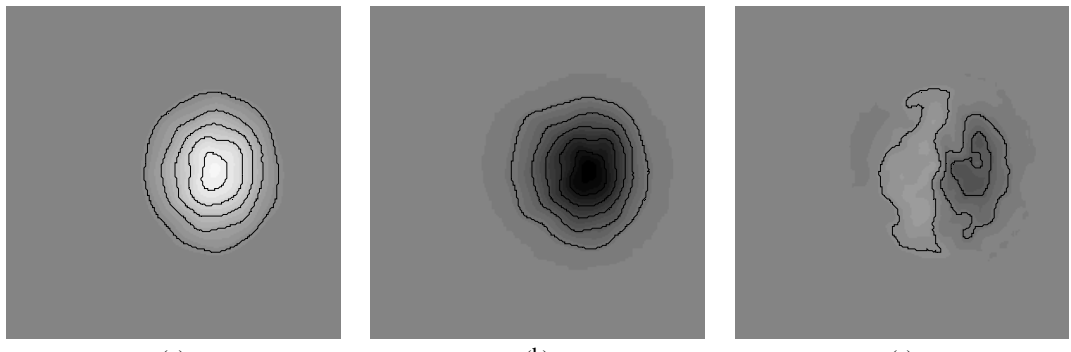


Figure 44: SBS beam overlap. (a) Image of Laser A. Lighter shades indicate higher intensity. (b) Image of Laser B. Darker shades indicate higher intensity. (c) Combined laser beams showing the two SBS beams are nearly coaxial.



output indicates a higher intensity. Part (b) of these figures shows the intensity profile of laser B. These images are shaded such that darker regions indicate higher intensities. Finally, part (c) is the addition of both the images from (a) and (b). This image corresponds to a pixel-by-pixel image subtraction of beam B from beam A.

Figure 42 shows the relative positions of the Fresnel reflection off the front fiber facet. This image was collected from the fiber after it was cut to approximately two meters. The location of the reflected beams on the camera indicates of the relative position of the input beams on the front face of the fiber. As can be seen by the obvious structure in Figure 42(c), there is a significant mismatch between the locations of the output from laser A and laser B. This clearly indicates that the two lasers were not coaxially aligned before entry into the fiber. The transmitted intensity profiles are shown in Figure 43. It is apparent by the relative displacement of the two beams that spatial filtering due to the fiber was not responsible for the alignment of the laser beams. Finally, Figure 44 shows the Stokes beams generated by the two lasers. Both beams appear to be emitted from a Gaussian-like LP<sub>01</sub> fiber mode and as can be seen from Figure 44(c), the two beams have nearly identical spatial intensity distributions.

While visually gratifying, the above analysis does not offer a quantitative measure of the two-beam alignment. In order to define a measurable quantity that would indicate how well the two laser beams were aligned under the different scenarios, the images were again separately normalized but then the mean square deviation between the two images was calculated. This deviation is defined as follows.

$$\varepsilon = \frac{1}{N} \sum_i^N [I_A(x_i) - I_B(x_i)]^2 \quad (4)$$

where  $I_{A,B}(x_i)$  indicates the intensity of the pixel at  $x_i$  associated with laser A,B and  $N$  is the total number of pixels in the image. The resulting number is a measure of the quality of the beam alignment.

Table 6 summarizes the degree of misalignment of the various beams. In this calculation  $N$  is 57,600 and the pixel intensity differences are those seen in Figure 42-Figure 44. The results in the table reinforce what was clear based on the images. The mean square deviation described indicates that the Stokes beams overlap nearly 7 times better than the transmitted and input beams. Since the output power of a single laser or amplifier is inherently limited by beam degradation, thermal loading, or pump coupling, this method of incoherent beam combining can be used to scale diffraction-limited powers beyond the limit that a single emitter can produce.

Table 6: Quantitative measure of beam overlap

|   | Pump | SBS  | Transmitted |
|---|------|------|-------------|
| $\frac{1}{N} \sum [I_A(x_i) - I_B(x_i)]^2 (10^{-10})$ | 7.07 | 1.05 | 6.86        |
| Relative Misalignment                                 | 6.73 | 1    | 6.53        |

### 5.3.3. Spatial coherence

#### Experimental Setup

The previous experiments into SBS incoherent combining were completed with relatively low power diode lasers, thus the fiber diameter had to be kept small to observe SBS. At the time of the experiment, those were the only appropriate lasers for the

investigation. However, two single-frequency Lightwave Electronics Nd:YAG lasers were acquired about 18 months later. Each laser could be tuned several GHz thus their frequencies could easily be separated by more than the Brillouin gain bandwidth. This made these sources perfect for further investigation into incoherent beam combining.

Although the previous experiments investigated the spatial overlap of the pump and Stokes beams, they do not necessarily prove spatial coherence. A Gaussian-like Stokes output could be observed if the beam traveled in a superposition of fiber modes or if the beam spatial pattern fluctuated fast relative to the CCD frame rate. This Gaussian-like output would not have the high spatial quality of the LP<sub>01</sub> mode. The following experiment was designed to further strengthen the argument that not only do the Stokes beams overlap, but they are also spatially coherent.

A schematic of this experimental setup is shown in Figure 45. Two Lightwave-Electronics Nd:YAG lasers, operating at slightly different frequencies, were nearly spatially combined with a polarization beam splitter. Both beams were then coupled into a 4.4 km, graded-index, 50-micron fiber. The portion of the scattered beam that reflects off the back surface of an uncoated plane-parallel-plate was split using a 50/50 beam splitter. The two beams then traveled two paths of equal length to a second 50/50 beam splitter where they were nearly spatially re-combined. The interference pattern generated was then imaged with a CCD camera at several points as the angle of the mirror indicated in the interferometer was adjusted.

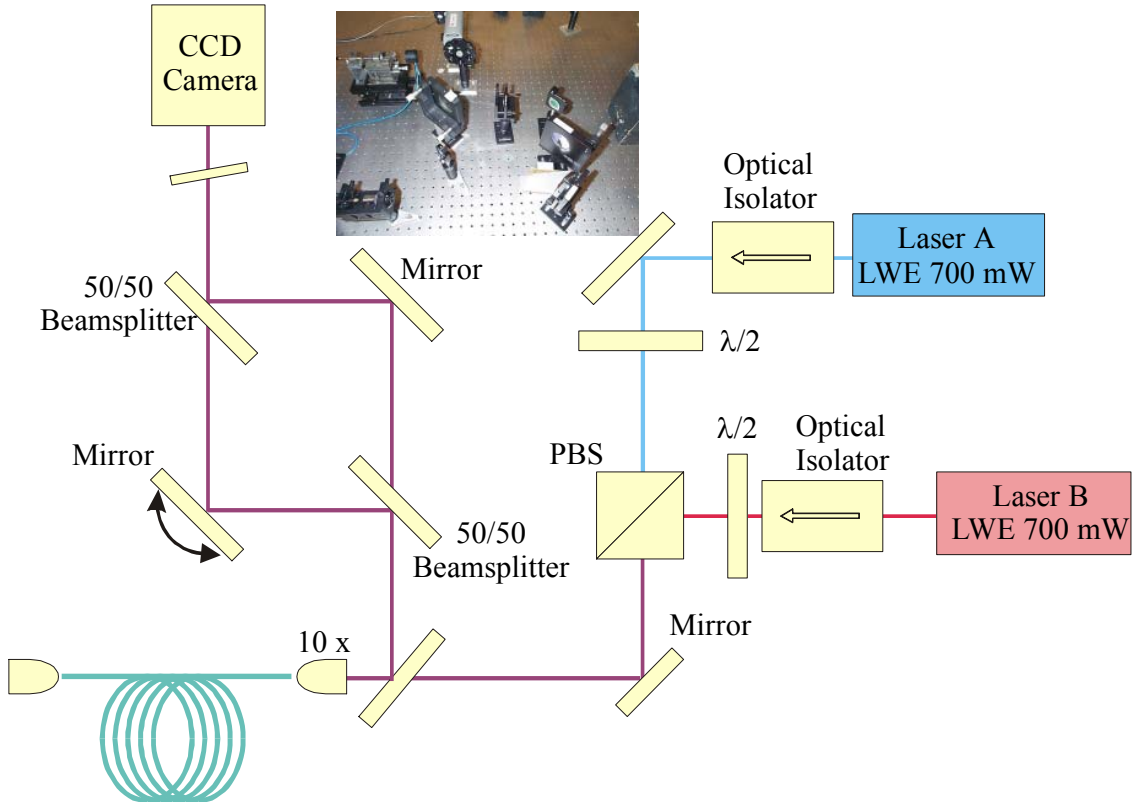


Figure 45: Experimental setup for spatial coherence measurement.

## Results

Figure 46 shows the interference pattern generated by the two paths at several mirror angles. As the mirror is rotated and the two paths overlap, a very distinct, linear interference pattern becomes visible. These interference lines are visible as the moving beam is swept through both sides of the stationary beam, which is strong evidence that the beams are spatially coherent. A spatially incoherent beam may produce linear interference pattern when the beams overlap perfectly. However, the interference would wash out or become distorted with any spatial misalignment between the two paths.

Since the separation between two adjacent constructive interference points is frequency dependent, it was critical in this experiment that the pump beams operated at

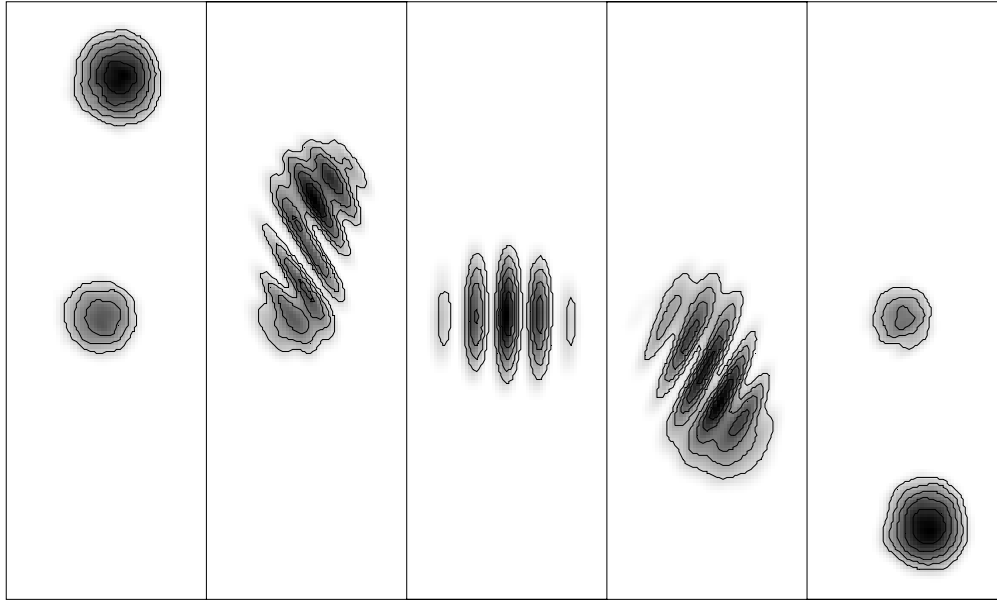


Figure 46: Interference patterns of the Stokes beam demonstrating its spatial coherence.

nearly the same frequency. If they were not, the interference lines generated by the two frequency components of the Stokes beam would become much more difficult to interpret even if both beams propagated in the  $LP_{01}$  mode.

#### *5.3.4. Conclusions*

In this chapter a method for incoherently combining multiple laser beams into a single beam of high spatial coherence through stimulated Brillouin scattering in a long multi-mode fiber is examined. The experiments demonstrate the independence of the Stokes wave excitation for pump beams with different wavelengths. The quality of beam overlap has been quantified using the mean square error between the beam profiles. Using this measure, it was shown that the two multi-mode input pump beams that were not incident coaxially were converted into a beam of single spatial mode. In addition, it was shown that the two Stokes beams resulting from the separate lasers had essentially

identical spatial intensity profiles. Finally, observing the interference between different portions of the beam further supported the spatial coherence of the beams.

## **6. SBS Beam Cleanup and Combining Limitations**

There are many potential limitations to the scalability of the beam combining and beam cleanup experiments described in Chapters 4 and 5. Some of these boundaries and schemes to overcome them are described here. In Section 6.1, a scheme to increase the number of beams that can be combined in a single is presented. This is followed by a discussion of the second order Stokes threshold, and the chapter is concluded in Section 6.2 with a description of stimulated Raman scattering beam cleanup.

### **6.1. Multiple Beam Combining**

The beam combining schemes of the previous chapter were limited by the output coupling of the Stokes beam. In all of the cases described, the useful output was collected by the Fresnel reflection of an uncoated plane-parallel-plate. This is approximately 4% of the total Stokes power and makes the true efficiency of the beam combining very low. Coatings on the surface of the flat could increase this reflection coefficient, but since the Stokes shift is so small, this will come at the expense of the pump power and nothing is gained. Neither can polarization be used since the pump beams are orthogonally polarized. If incoherent beam combining is used, the beams can be nearly spatially combined with a dichroic mirror and polarization can be used to extract the Stokes beam. However, scaling this to more than a couple lasers would be extremely complicated.

A proposed solution to this problem is to pump the edges of the fiber and extract the Stokes beam from the center of the fiber. Although this spatial output coupling was not

completed, the ideas examined during the course this research are presented here. In each of these designs, the ideas are readily expanded to more pump beams.

The most conceptually simple experiment along these lines is to use four independent mirrors equally spaced about a central hole (see Figure 47). Four pump beams incident upon these mirrors could then be coupled into the fiber at relatively high angles while the Stokes beam would escape out the central hole. In practice however, this experiment would be very difficult to implement. The multimode fiber used for the majority of the beam cleanup and combining experiments has a core diameter of 50-microns. Simply imaging the mirror assembly, diameter =  $d$ , on the fiber facet with a single lens, focal length =  $f_l$ , would require that the distance between the mirror and the lens be approximately

$$s \approx \frac{f_l d}{50 \times 10^{-6}} . \quad (6.1)$$

A lens with a short focal length and a small mirror assembly is preferable to reduce the distance from the mirrors to the lens. Assuming a standard microscope objective with a numerical aperture that matches the numerical aperture of the fiber ( $NA = 0.201$ ), the focal length is expected to be approximately 16mm. Using a relatively compact mirror assembly such that  $d = 25\text{ mm}$ , results in  $s = 8\text{ m}$ . Such a large distance between the mirrors and the lens will result in a system that is very sensitive to vibration and unreliable.

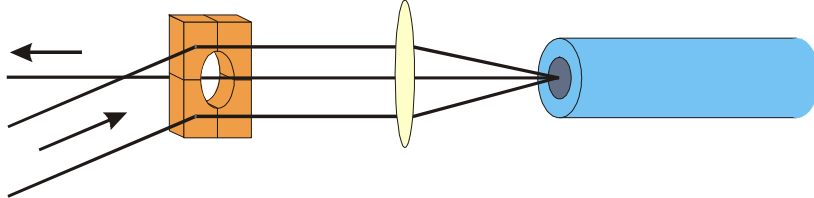


Figure 47: Multi-beam coupling for beam combining.

A more elegant solution to the problem would be to use a short bundle of fibers. In this design, six fibers could easily be arranged about a central output fiber, see Figure 48. Scaling to larger bundles, such as adding another ring of 12 input fibers, would be a relatively simple task. Immediately after the fiber, each of the diverging waves would be collimated with a lens array or fiber pigtail collimators and the overall beam would be focused into the long, multi-mode fiber.

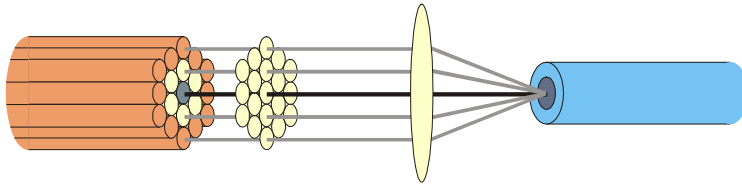


Figure 48: Fiber bundle multiple beam combining schematic diagram.

There are several constraints on the pump beam and fiber array required to ensure efficient beam combining. First, each pump beam must have a spot size that fits within the active fiber core. Second, the numerical aperture of the combined pump beams must be less than the numerical aperture of the fiber. Finally, the spot size of the reflected Stokes beam must be efficiently coupled into the output fiber. The effect of each of these requirements is analyzed below.

Assuming each beam exiting the fiber bundle has a Gaussian intensity distribution and is collimated by the lens array such that the beam diameter is  $d_{fb}$ , each beam will be

focused by the coupling lens, focal length =  $f$ , to a spot size,  $w_g = \frac{2\lambda f}{\pi d_{fb}}$ . Any aberration

on the pump beam will increase this spotsize by a constant factor. Since this spot size must fit within the fiber core, the first constraint on the pump beams becomes

$$w = M^2 w_g \leq \frac{2}{3}a . \quad (6.2)$$

where  $M^2$  is the beam quality factor reviewed by Siegman in [51] and  $a$  is the radius of the fiber core. The factor of 2/3 is included in the inequality to ensure that more than 99% of the pump beam is enclosed by the fiber core.

The second constraint on the set of pump beams is that it has a numerical aperture,  $NA_p$ , less than that of the active fiber,  $NA$ . The effective numerical aperture of the pump depends on the total diameter of the pump ring after the collimating lens,  $d_c$ , and the focal length of the coupling lens.

$$NA_p = \frac{d_c}{2f} \leq NA \quad (6.3)$$

Additionally, the backward traveling Stokes beam must be efficiently coupled into the output fiber. Assuming a graded index fiber, the  $LP_{01}$  mode is closely approximated by a Gaussian beam with a spot size of  $\sqrt{\frac{\lambda a}{\pi NA}}$  [52]. If the waist is located at the front fiber facet, the spot size just after the coupling lens is

$$w_{SBS} = \sqrt{\frac{\lambda a}{\pi N A}} \left[ 1 + \left( \frac{N A}{a} f \right)^2 \right]^{1/2} .$$

$$\approx \sqrt{\frac{\lambda N A}{\pi a}} f$$
(6.4)

To reach the approximate solution it is assumed that  $\left( \frac{N A f}{a} \right)^2 \gg 1$ . The output coupler

must be at least 1.5 times the size of the Stokes beam to collect more than 99% of the power. As can be seen by Figure 49, the total diameter of the ring of pump beams must therefore be

$$d_c \geq 3d_{fb} + 3\sqrt{\frac{\lambda N A}{\pi a}} f .$$
(6.5)

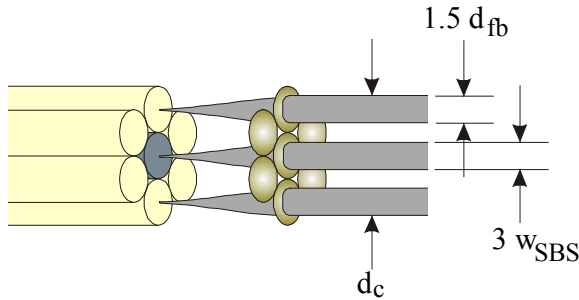


Figure 49: Definition of beam size variables.

Plugging this into Equation (6.3) and combining the result with Equation (6.2) yields

$$\frac{3}{2} \frac{d_{fb}}{N A - \frac{3}{2} \sqrt{\frac{N A \lambda}{\pi a}}} \leq f \leq \frac{2\pi}{6} \frac{a d_{fb}}{M^2 \lambda} .$$
(6.6)

Thus

$$\frac{3}{2} \frac{d_{fb}}{NA - \frac{3}{2} \sqrt{\frac{NA\lambda}{\pi a}}} \leq \frac{2\pi}{6} \frac{ad_{fb}}{M^2 \lambda}. \quad (6.7)$$

Solving for  $M^2$  results in

$$M^2 \leq \frac{2}{6} \left( \frac{2}{3} \frac{NA\pi a}{\lambda} - \sqrt{\frac{NA\pi a}{\lambda}} \right). \quad (6.8)$$

Using this equation, the maximum  $M^2$  value can be calculated as a function of the fiber parameters,  $NA$ ,  $a$ , and the wavelength of the light used,  $\lambda$ . The multi-mode fiber used in the beam combining experiments of the previous chapter had a numerical aperture of 0.206 and a fiber radius of 50 microns. If pumped at 1.064 microns, the maximum value of  $M^2$  is 2.1. Thus the fiber bundle must deliver good quality pump beams for efficient beam combining. This constraint could be significantly relaxed using a fiber with a larger core diameter, higher numerical aperture, or using a shorter wavelength.

Equation (6.6) can be used to determine the best set of values for  $d_{fb}$  and  $f$ . However, geometrical constraints will also have to be taken into account. Convenience may dictate that each fiber in the bundle be equally spaced, which would force the spacing between fiber cores to be the greater of  $d_{fb}$  and  $2w_{SBS}$ . This will increase the constraint on  $M^2$  and for some fiber parameters and pump wavelengths it may not be possible to obtain efficient beam combining.

Newer pumping schemes may also be employed to simplify beam combining. Lucent Technologies has developed a tapered fiber bundle for use in pumping fiber lasers and amplifiers [53]. A schematic diagram of the fiber is shown in Figure 50. In contrast to

the design above, the pump fibers are physically attached to the active fiber, thus the system would be very robust.

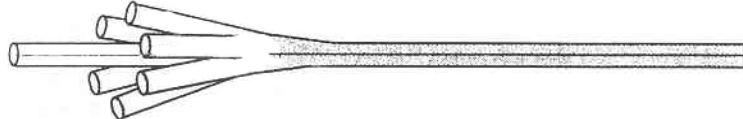


Figure 50: Tapered fiber bundle designed by Lucent Technologies [53].

## 6.2. Second Order Threshold

The second-order SBS process could potentially limit the maximum power that can be combined or cleaned in a single fiber. Above the second-order threshold, any increase in the pump power will contribute primarily to the second-order beam, resulting in decreasing efficiency with increasing pump power. Other processes that rely upon SBS in fibers such as phase conjugation [54] will suffer from similar limitations. Thus, knowledge of this threshold is critical to understanding the potential benefits and limits of these applications. In this section, the second-order Stokes threshold is measured and analyzed.

This investigation was completed in two parts. First, a long fiber with a small diameter was used to measure the threshold experimentally. Second, a set of the coupled differential equations for the pump, first Stokes, and second-Stokes beams was numerically solved using appropriate coupling terms and fit to the experimental data for validation. The coupled equations could then be used to determine the second-Stokes threshold for fibers of arbitrary length and size.

### *6.2.1. Experimental Setup*

The experiment was performed using the optical setup schematically shown in Figure 51. A 4.4 km Corning SMF-28 fiber was used as the SBS medium. It was pumped at 1.064  $\mu\text{m}$  with a diode-pumped, single-frequency Nd:YAG laser producing up to 600 mW. After accounting for two passes through an amplifier as well as coupling losses, more than 800 mW was measured in the fiber. As the pump power was varied, the power in the reflected Stokes beam was measured and the relative power transmitted through the fiber was monitored with a scanning Fabry-Perot spectrum analyzer. The spectrum analyzer output was used to determine second-order threshold. Above threshold, the output clearly showed three distinct peaks (Figure 52, inset). The height of the peak furthest to the left indicates the relative intensity of the transmitted residual pump beam that was not absorbed or converted into the Stokes beam. The second peak shows the portion of the first Stokes beam that was internally reflected off the front fiber facet and then traveled forward through the fiber to be detected by the Fabry-Perot. The third peak is due to the second-order Stokes beam. The Stokes shift of 16.1 GHz is nearly twice the free spectral range of the Fabry-Perot resonator, 8 GHz, resulting in the near overlap of the three peaks.

The height of these peaks as a function of the input pump power is shown in Figure 53(a-c). These plots reveal a strong coupling between the transmitted beams. At first order threshold, 18 mW, the growth of the transmitted pump beam was strongly attenuated and the forward propagating first order Stokes beam began to grow linearly. Similarly, at the second order threshold, 273 mW, the growth of the forward propagating Stokes beam was suppressed and the second order Stokes beam began to increase. This

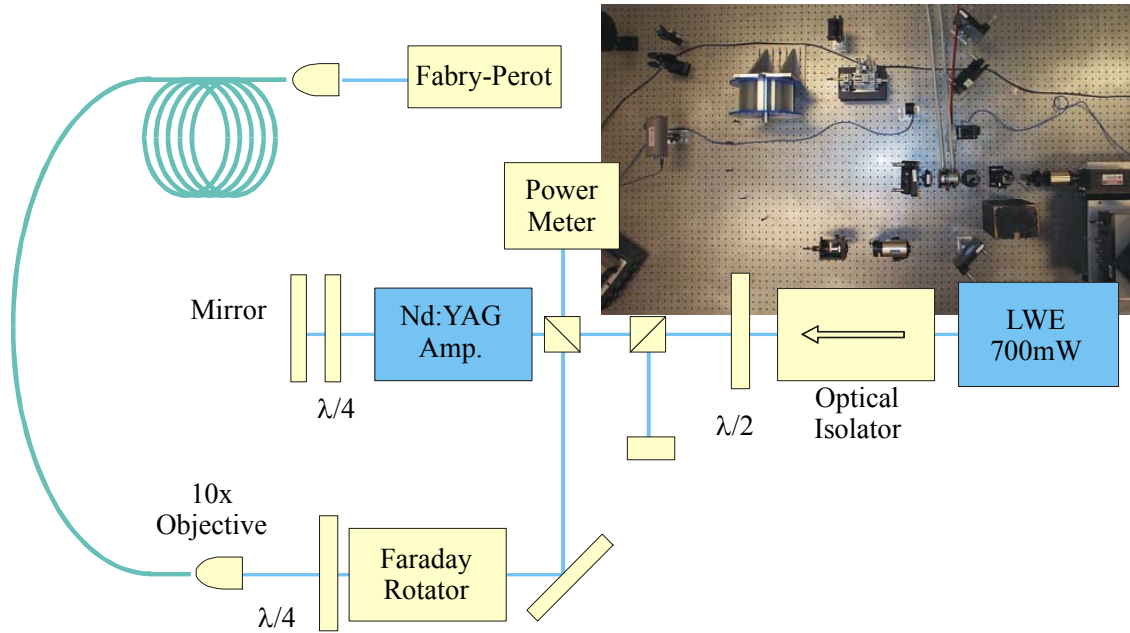


Figure 51: Schematic of the experimental setup used to measure the second order Stokes threshold.

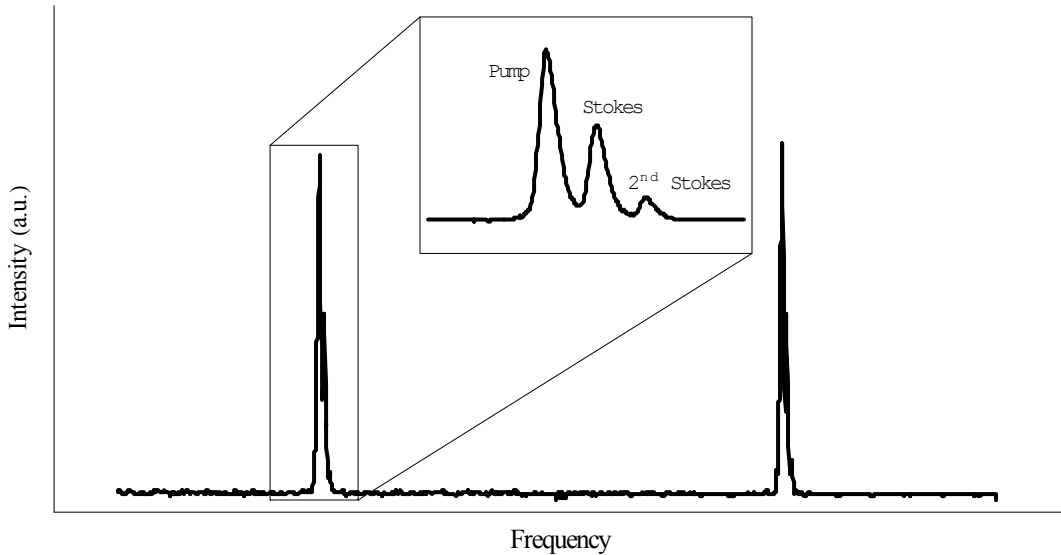


Figure 52: Transmitted spectrum through a long fiber above second order threshold.

trend was expected since power is transferred to lower energies through SBS. However, at the same point, the transmitted pump beam also began to increase. This behavior indicated that four-wave mixing (FWM) between the forward propagating Stokes beam, the pump beam and the second-order Stokes beam was responsible for part of the transfer

of energy to the pump and second-order beam. At even higher powers,  $\sim$ 500 mW, the transmitted pump and second-order beams tapered off. This behavior is found to coincide with the appearance of a third-order Stokes beam in the transmitted spectrum and is also believed to be due to four-wave-mixing.

The power in the backward traveling Stokes beam is plotted as a function of the pump power in Figure 53(d). This further reinforces the claim that four-wave mixing is at least partly responsible for the growth of the second-order Stokes beam. The slope efficiency below second order threshold was found to be  $88 \pm 1\%$ . Above second order threshold but below the appearance of the third-order Stokes beam, the slope efficiency was found to be  $81 \pm 2\%$ . Such a small change in slope efficiency reveals that the coupling between the backward traveling Stokes beam and the second-order Stokes beam is at best very weak.

To test this theory, the normal cleave at the front fiber facet was replaced by an angle cleave and the transmitted and reflected beams were monitored in the same way as before. This data is shown in Figure 54. The angle cleave prevented any of the Stokes beam that was internally reflected by the front fiber facet from being guided by the fiber. Thus Figure 54(b) shows no transmitted Stokes beam. Additionally, without the forward propagating Stokes beam in the fiber, FWM was suppressed, eliminating the second order

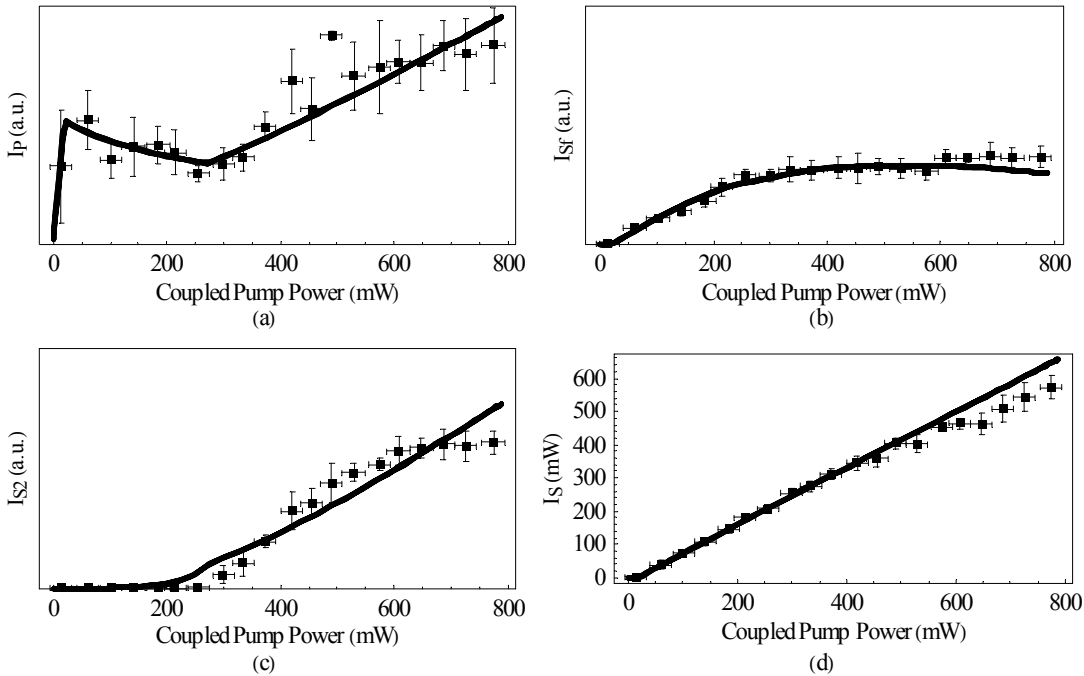


Figure 53: (a-c) Power transmitted through the SMF-28 fiber as a function of the input power at the pump, Stokes and second order Stokes frequencies. The solid lines indicate the best theoretical fit. The dashed lines show the best fit ignoring either second order SBS contributions or four wave mixing effects. (d) The first Stokes power as a function of input power.

Stokes beam. Unfortunately, the angle cleave also reduced the coupling efficiency into the fiber and the maximum power coupled into the fiber was only 500mW in the transmitted spectrum. This is nearly twice the original second-order threshold. However, no second order Stokes beam was observed. Unfortunately, the slope efficiency was also reduced to  $66 \pm 1\%$ . This reduction from the high slope efficiency of the normal cleave data is believed to be caused by a reduction in the overlap of the pump beam and the first order Stokes beam and not a direct result of the angle cleave.

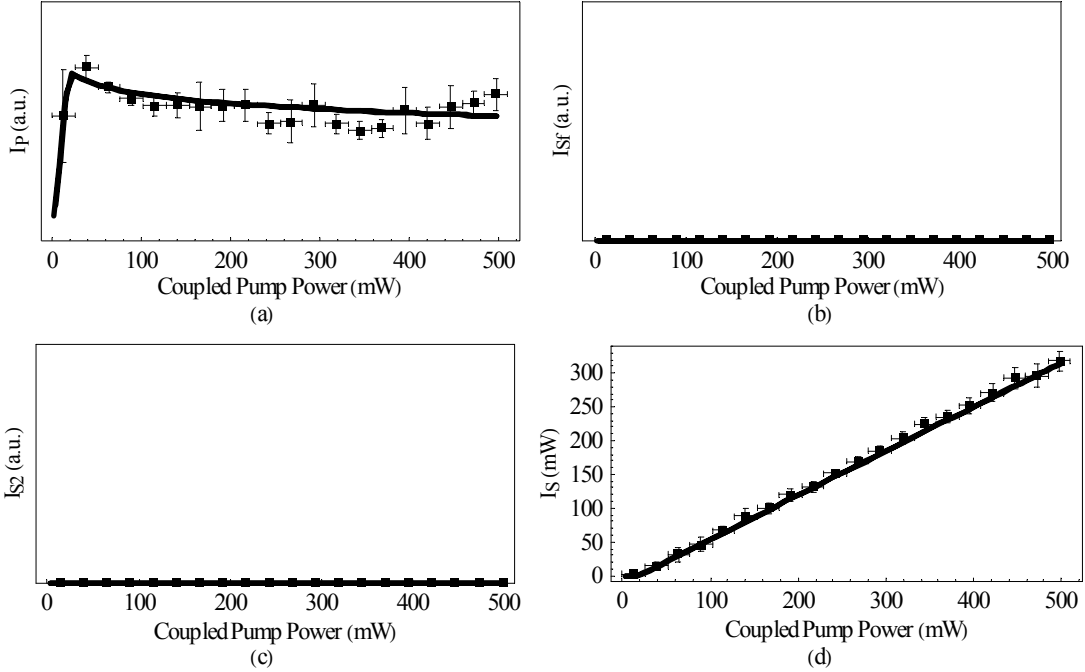


Figure 54: (a-c) Power transmitted through the SMF-28 fiber as a function of the input power at the pump, Stokes and second order Stokes frequencies when the front fiber facet was cleaved at an angle. The solid lines indicate the best theoretical fit. The dashed lines show the best fit ignoring either second order SBS contributions or four wave mixing effects. (d) The first Stokes power as a function of input power.

### 6.2.2. Modeling

The plane wave solution to Maxwell's equations including the effects of SBS, four-wave mixing and absorption on the coupling between the pump,  $A_p$ , backward traveling Stokes,  $A_s$ , forward traveling Stokes,  $A_{sf}$ , and second order Stokes,  $A_{s2}$ , electric field amplitudes is given by

$$\begin{aligned}
 \frac{\partial}{\partial z} A_p &= -g_B \epsilon_0 c n A_p |A_s|^2 + i 2 \epsilon_0 n_2 \omega n A_{sf}^2 A_{s2}^* \exp[i(2k_{sf} - k_{s2})z] - \frac{\alpha}{2} A_p \\
 \frac{\partial}{\partial z} A_s &= -g_B \epsilon_0 c n A_s |A_p|^2 + g_{B2} \epsilon_0 c n A_{s2} |A_s|^2 + \frac{\alpha}{2} A_s \\
 \frac{\partial}{\partial z} A_{sf} &= i 4 \epsilon_0 n_2 \omega n A_{sf}^* A_p A_{s2} \exp[i(k_p + k_{s2} - k_{sf})z] - \frac{\alpha}{2} A_{sf} \\
 \frac{\partial}{\partial z} A_{s2} &= g_{B2} \epsilon_0 c n A_{s2} |A_s|^2 + i 2 \epsilon_0 n_2 \omega n A_{sf}^2 A_p^* \exp[i(2k_{sf} - k_p)z] - \frac{\alpha}{2} A_{s2}
 \end{aligned} \tag{6.9}$$

In these equations,  $\epsilon_0$ ,  $g_B$ , and  $n_2$  are vacuum permittivity, the Brillouin gain, and nonlinear index, respectively. Other nonlinear coupling terms such as self- and cross-phase modulation [3] did not affect the results in a meaningful way and were therefore neglected.

To account for the fact that the fields travel in fiber modes and thus cannot be plane waves, the gain coefficients of the various components in Equation (6.9) must be adjusted. Additionally, since the depletion of the backward traveling Stokes beam due to second order SBS was relatively minor, this term was neglected in the equations. Stokes depletion was partially accounted for with the initial conditions that will be discussed later. Finally, because the SBS Stokes shift is so small, the phase mismatch was assumed to be negligible. Thus Equation (6.9) becomes

$$\begin{aligned}\frac{\partial}{\partial z} A_p &= -\eta_{SBSp} g_B \epsilon_0 c n A_p |A_s|^2 + i \eta_{FWM} 2 \epsilon_0 n_2 \omega n A_{sf}^2 A_{s2}^* - \frac{\alpha}{2} A_p \\ \frac{\partial}{\partial z} A_s &= -\eta_{SBSs} g_B \epsilon_0 c n A_s |A_p|^2 + \frac{\alpha}{2} A_s \\ \frac{\partial}{\partial z} A_{sf} &= i \eta_{FWM} 4 \epsilon_0 n_2 \omega n A_{sf}^* A_p A_{s2} - \frac{\alpha}{2} A_{sf} \\ \frac{\partial}{\partial z} A_{s2} &= \eta_{SBS2} g_{B2} \epsilon_0 c n A_{s2} |A_s|^2 + i \eta_{FWM} 2 \epsilon_0 n_2 \omega n A_{sf}^2 A_p^* - \frac{\alpha}{2} A_{s2}\end{aligned}\quad (6.10)$$

The magnitude of each of these fields at the front fiber facet was used as the initial condition to solve these coupled equations numerically. The Stokes beam amplitude is initialized based upon the measured reflected Stokes beam. Below first-order threshold, the amplitude is zero. Between the first- and second-order thresholds, the Stokes intensity is  $\eta_l (I_p - I_{thl})$ , where  $\eta_l$  is the measured slope efficiency of this region, 88%,

$I_p$  is the intensity of the pump beam and  $I_{th1}$  is the first-order Stokes threshold. Above second-order threshold,  $I_{th2}$ , the Stokes beam intensity was initialized to  $\eta_1(I_{th2} - I_{th1}) + \eta_2(I_p - I_{th2})$ , where  $\eta_2$  is the slope efficiency of this region. Based solely on the reflected Stokes beam, this efficiency would be 81%. However, this number was used as a parameter to improve the fit to the transmitted data resulting in  $\eta_2 = 84\%$ . The forward propagating Stokes beam was initialized by assuming that 3.6% of the Stokes beam was internally reflected at the front fiber facet, which was all coupled back into the fiber. Finally, the second-order Stokes beam was initialized by injecting a single spontaneous photon per mode at the front fiber facet [18].

Using Equations (6.10) and the appropriate initial conditions on the fields at the front fiber facet, the standard numerical differential equation solver in Mathematica generated the expected transmitted powers. Along with the slope efficiency of the Stokes beam above second order threshold,  $\eta_{SBS_p}$ ,  $\eta_{SBS_s}$ ,  $\eta_{SBS_2}$ , and  $\eta_{FWM}$  were adjusted to minimize the mean square error between the relative transmitted power in each frequency component and the predicted transmission based upon Equation (6.10). The fit is based solely on the region below the appearance of the third order frequency component, <500 mW where the model is expected to perform reasonably well. The best fit values are summarized in Table 7 and the resulting curve is shown by the solid lines in Figure 53.

Table 7: Fit parameters for second order Stokes threshold model.

|           | $\eta_2$ | $\eta_{SBS_p}$ | $\eta_{SBS_s}$ | $\eta_{SBS_2}$ | $\eta_{FWM}$ |
|-----------|----------|----------------|----------------|----------------|--------------|
| Fit Value | 0.84     | 0.67           | 0.58           | 2.7            | 1.5          |

The effect that each of these parameters has on the overall transmission curves is rather complicated. However, the numerical factors can be informative. The SBS gain in a non-polarization preserving fiber is expected to be a factor of 1.5 less than that of a polarization preserving fiber [55]. This explains the factor of 0.67 for  $\eta_{SBS_p}$ .

The difference between  $\eta_{SBS_s}$  and  $\eta_{SBS_p}$  is responsible for the portion of the pump beam that is Brillouin reflected into a radiation mode and is therefore not guided by the fiber. Although not modeled in this manner, the presence and excitation of these modes is explained by Garth *et al.* [56]. The ratio of these numbers is closely related to the slope efficiency of the first-order Stokes beam  $\eta_{SBS_s}/\eta_{SBS_p} = 0.86$ .

The second order Brillouin gain is enhanced in this model by a factor of  $\eta_{SBS_2}$ . This factor is due in part to the increased effective gain that results from the enhanced overlap of the Stokes and second order beams caused by beam cleanup. Since in Chapter 4 it was demonstrated that an aberrated pump beam excited a Stokes beam in an LP<sub>01</sub> fiber mode, it is reasonable to assume that the second order Stokes beam would also propagate in the LP<sub>01</sub> mode. Thus each of these modes is confined to the core more strongly than an aberrated beam and the effective intensity is increased over that of a uniformly illuminated fiber core. This accounts for part of the enhanced Brillouin gain. However it is unlikely that it completely explains the magnitude of this factor. Another contribution involves the neglected depletion of the Stokes beam. Depletion of the Stokes wave due to the second order beam would slow the growth of the Stokes beam in the backward

direction. Because of the forced condition on the Stokes power at the front fiber facet, this elevates the intensity of the Stokes beam over a longer portion of the fiber, thus increasing the fiber's effective length and improving conversion to the second order beam.

Similar arguments could be made to explain the enhancement to the four-wave-mixing gain. However, it is complicated by the inclusion of three field distributions and the fact that the different terms were not allowed to vary independent of one another. Initially, these were allowed to independently change to enhance the fit between experiment and theory. However, the benefit of the two extra degrees of freedom was minimal.

To model the effect that the angle cleave had on the transmitted beams, the initial conditions for both the backward and forward propagating Stokes beams had to be modified. The initial condition for the backward propagating Stokes beam at the front fiber facet was modeled by the reflected Stokes power shown in Figure 54(d). Thus below first order threshold, the intensity was set equal to zero. Above threshold, the slope efficiency was constant and the input intensity was equal to  $\eta_l(I_p - I_{thl})$ , where  $\eta_l = 66\%$ . On the other hand, the forward propagating Stokes beam was set equal to zero at the front fiber facet for all pump powers, accounting for the assumption that none of the Stokes beam that is internally reflected at the front fiber facet is coupled back into a guided mode. The results of these calculations are shown by the solid lines in Figure 54 and demonstrate a strong agreement with the measured data.

Since second order threshold without the forward propagating Stokes beam was not observed, the threshold for this condition had to be calculated theoretically with no experimental verification. When  $A_{sf} = 0$ , Equation (6.10) becomes

$$\begin{aligned}\frac{\partial}{\partial z} A_p &= -g_B \epsilon_0 c n A_p |A_s|^2 - \frac{\alpha}{2} A_p \\ \frac{\partial}{\partial z} A_s &= -\eta g_B \epsilon_0 c n A_s |A_p|^2 + \frac{\alpha}{2} A_s \\ \frac{\partial}{\partial z} A_{s2} &= g_{B2} \epsilon_0 c n A_{s2} |A_s|^2 - \frac{\alpha}{2} A_{s2}\end{aligned}\quad (6.11)$$

Which can be written in terms of the beam intensities

$$\begin{aligned}\frac{\partial}{\partial z} I_p &= -g_B I_p I_s - \alpha I_p \\ \frac{\partial}{\partial z} I_s &= -\eta g_B I_p I_s + \alpha I_s \\ \frac{\partial}{\partial z} I_{s2} &= g_{B2} I_{s2} I_s - \alpha I_{s2}\end{aligned}\quad (6.12)$$

Since the depletion of the backward propagating Stokes beam was ignored, the intensity distribution of the second order beam can be solved explicitly as a function of the Stokes beam intensity.

$$I_{s2}(z) = I_{s2}(0) \exp \left[ \left( g_{B2} \int_0^z I_s(z) dz - \alpha \right) z \right] \quad (6.13)$$

According to Smith [18], first-order threshold for SBS occurs when the gain in the exponent is equal to 21. Assuming this numerical factor is the same for the second-order threshold results in

$$P_{sth2} = 21 \frac{A_{eff}}{g_B L_{eff}}, \quad (6.14)$$

where  $P_{sth2}$  is the Stokes power at threshold,  $A_{eff}$  is the effective cross sectional area of the fiber, and the effective length,  $L_{eff}$ , is given by

$$L_{eff} = \frac{1}{I_s(0)} \int_0^L I_s(z) dz. \quad (6.15)$$

The Stokes intensity distribution can be solved exactly if the pump and Stokes absorption is ignored. This leads to

$$I_s(z) = \frac{I_s(0)[I_p(0) - I_s(0)]}{I_p(0) \exp\{g_B [I_p(0) - I_s(0)]z\} - I_s(0)} \quad (6.16)$$

and the effective length is analytically solved to be

$$L_{eff} = \frac{1}{I_s(0)} \left\{ L[I_s(0) - I_p(0)] + \frac{1}{g_B} \ln \left\{ \frac{\exp\{Lg_B [I_p(0) - I_s(0)]\} I_p(0) - I_s(0)}{I_p(0) - I_s(0)} \right\} \right\}. \quad (6.17)$$

With absorption taken into account, the Stokes intensity distribution in the fiber can be estimated by numerically solving the first two equations of (6.11). Similar to the analytical solution of Equation (6.16), it has a strong dependence on the pump power coupled into the fiber. At high pump powers, the Stokes beam grows very quickly near the front of the fiber resulting in a short effective length. At low pump powers, the Stokes beam has a slow growth in the backward direction, resulting in a relatively long effective length. The relative Stokes power distribution in the fiber along with the effective length of the fiber for various pumping conditions are plotted in Figure 55.

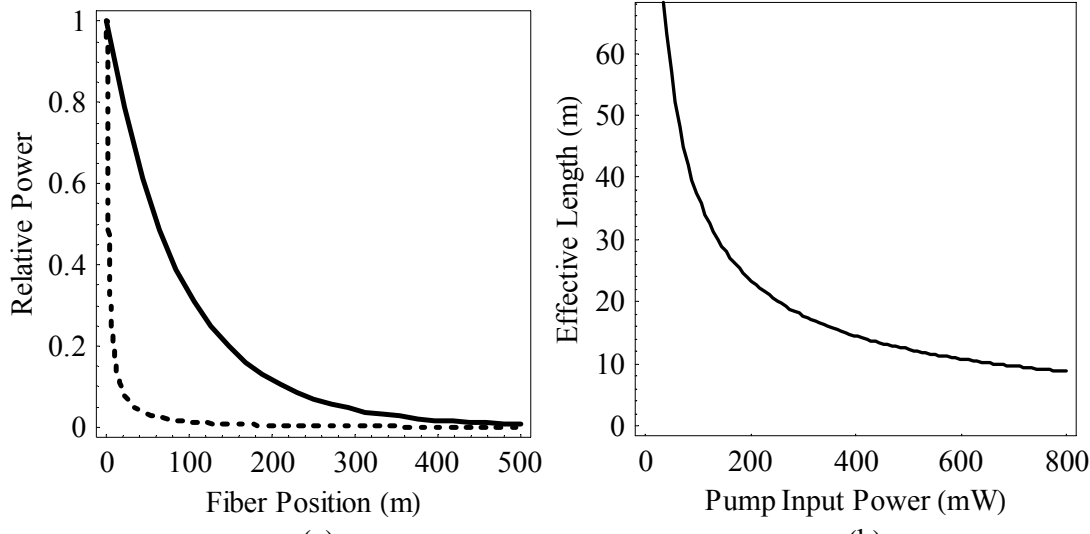


Figure 55: (a) Relative Stokes power distribution in a fiber for a 20 mW pump beam (solid) and a 800 mW pump beam (dashed). (b) Second-order effective length as a function of input power for a 4.4 km fiber.

Using this for the effective length in Equation (6.14) results in a Stokes power at threshold of  $P_{sth2} = 2.1\text{W}$  and a pump power at threshold of  $2.4\text{W}$ . If the Brillouin gain coefficient as given in the open literature is used, these values increase significantly, thus this should be regarded as a minimum threshold.

### 6.2.3. Conclusions

Even in the presence of four-wave mixing, the second order threshold was nearly fifteen times greater than the first order threshold. When four-wave mixing was suppressed, the threshold was found experimentally to be at least 27 and theoretically to be more than 130 times the first order threshold. These relatively high thresholds are due to the decreasing effective length of the fiber,  $L_{eff}$ , with increasing pump power as seen by the second Stokes beam.

As shown in Equation (6.14), the second order threshold will proportionally increase with the effective area of the fiber. Thus for beam combining, cleanup, and phase conjugation applications that require a large fiber core, the second order threshold is not expected to become a practical limiting factor. The useful power bandwidth of these devices has the potential to stretch from the first order threshold to the second order threshold, which was calculated to be  $43 \cdot A_{eff} [\text{mW}/\mu\text{m}^2]$  in the absence of a forward propagating Stokes beam. In the 50-micron fiber used for the beam cleanup and combining experiments described in Chapters 4 and 5, this results in a power bandwidth of more than 80 kW. In almost all practical cases, it can be concluded that second-order SBS will not be a significant limiting factor in the operational dynamic range of SBS fiber beam combiners.

### 6.3. SRS Beam Cleanup and Combining

The Brillouin gain bandwidth is very narrow. This forces the pump laser to be spectrally pure or results in an increase in the Brillouin threshold [57, 58]. Either of these scenarios can be problematic for practical SBS beam cleanup/combining schemes. On the other hand, the Raman gain bandwidth is about five orders of magnitude larger, eliminating the stringent requirements on the pump lasers. Spectrally broad beams, such as pulsed sources and common diode lasers, can efficiently excite a Stokes beam. Unfortunately, the relaxed requirements come with a price. The Raman gain coefficient is about two orders of magnitude smaller than the Brillouin gain coefficient, resulting in a greater threshold. For extremely high power applications however, the threshold is expected to be a small percentage of the overall power and it is reasonable that stimulated

Raman scattering will be a more practical nonlinear mechanism for beam combining and cleanup than SBS.

Similar to stimulated Brillouin scattering, SRS has been used for phase conjugation [59, 60], but in fibers with long interaction lengths the phase conjugate fidelity is lost and the resulting Stokes beam is generated in the dominant fiber mode. In 1992, Chiang showed that when SRS was excited in a fiber, fewer fiber modes were observed in the Stokes beam than found in the pump beam [25]. He demonstrated that particular fiber modes could be excited in a 30m fiber by varying the pumping conditions. Longer fiber lengths, up to 1 km, resulted in a mixture of up to two fiber modes found in the first order Stokes beam, but a pure LP<sub>01</sub> mode found in each of the higher order modes.

Raman beam cleanup is not limited to fiber based systems. Long effective interaction lengths can be obtained by placing a Raman active material in a cavity resonant at the Stokes frequency. These Raman lasers have theoretically and experimentally been shown to produce a high quality Stokes beam even when the pump is a low quality beam [61, 62]. SRS has also been used to amplify a high spatial quality Stokes beam using an aberrated pump. In these experiments, the spatial profile of the Stokes beam can be maintained in the amplified output [63, 64].

This section describes the experimental results demonstrating the beam cleanup characteristics of stimulated Raman scattering in long fibers. The experiment is described in Section 6.3.1 and the results are analyzed and explained in Section 6.3.2. Conclusions are made in Section 6.3.3.

### *6.3.1. Experimental Setup*

Stimulated Raman scattering beam cleanup was demonstrated using a setup represented by the schematic shown in Figure 56. A frequency doubled Continuum Powerlite Nd:YAG laser oscillator was used to pump a 300 m long, 50-micron graded-index fiber. The laser produced an average power of 50 mW delivered in 10.5 ns pulses at 30 Hz. The power coupled into the fiber was controlled using a half-wave plate and a polarizer. A 10x microscope objective collimated the transmitted beam.

The beam was then focused with a 1m focal length lens and a long pass filter was used to remove the pump from the Stokes beam. The evolution of the beam profile was recorded at various points after the lens, showing the spot as it propagated through focus. Each profile was normalized to have an area of one, fit to a Gaussian intensity

distribution,  $\frac{1}{\pi\sigma^2} \exp\left(-\frac{2r^2}{\sigma^2}\right)$ , and the spot size (half-width at the  $1/e^2$  point),  $\sigma$ , was

recorded. This process was repeated with the laser power reduced below threshold and the long pass filter removed, showing the propagation of the pump beam over the same region.

The transmitted beam was then characterized spectrally. First, the beam spectrum was analyzed with a monochrometer equipped with an optical multichannel analyzer. Then the mirror near the output end of the fiber was replaced with a diffraction grating and the back fiber facet was focused directly on the CCD. In this manner the spatial

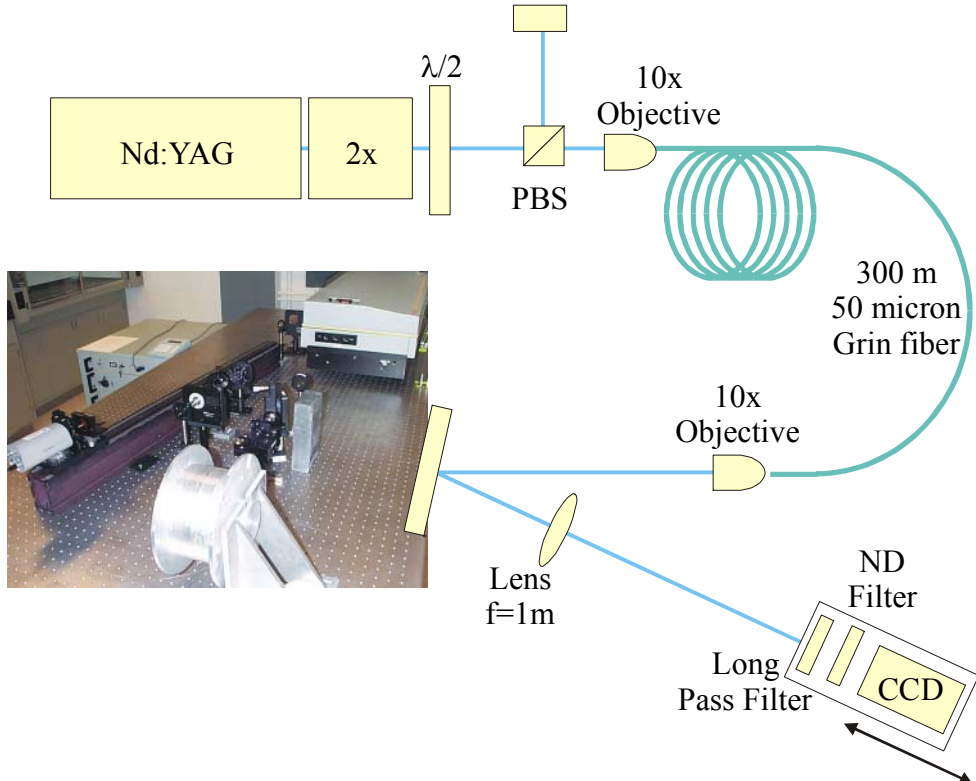


Figure 56: Schematic diagram of stimulated Raman scattering beam cleanup.

profile of each spectral component could be observed. This was completed at various fiber lengths and the size of the first Stokes component measured and compared to the size of the residual transmitted pump beam.

Fiber lengths ranging from 50 m to 300 m at 25 m increments were used to observe the effect of fiber length on the output spatial characteristics of the far-field beam profile. At each length, 65 successive images were collected under four separate conditions. The first two image sets showed the spectrally dispersed transmitted beam. These pictures included the pump, Stokes, and second order Stokes beams in each frame and were used to measure the diameter of each spectral component. The next set of images was collected below threshold, verifying that even without the excitation of the Stokes beam, the pump was transmitted in multiple fiber modes. Finally, a HeNe laser operating at

543 nm was used to illuminate the fiber end and another set of images was collected. This set showed the fiber core and cladding illuminated uniformly and allowed for an accurate calibration of the spotsize measurements made with the CCD camera. It also ensured that the fiber facet was accurately imaged on the CCD.

### 6.3.2. Results

The spatial quality of the pump and Stokes beams was measured by comparing their propagation to that of a Gaussian beam. The spot size of a Gaussian beam with a waist,  $w_0$ , located at a point,  $z_w$ , will vary with distance according to [52]

$$w_g(z) = w_0 \sqrt{1 + \left( \frac{\lambda(z - z_w)}{\pi w_0^2} \right)^2}. \quad (6.18)$$

If, on the other hand, the beam is not a perfect Gaussian, the spot size everywhere will be scaled by a constant factor,  $M$  [51]

$$w(z) = M w_g(z). \quad (6.19)$$

While this factor is a good measure of beam quality, it is typically reported as  $M^2$ . As can be found by a manipulation of Equation (6.19),  $M^2$  is the ratio of the far-field divergence of a real beam to that of a perfect Gaussian with identical waist diameters.

An example of the near- and far-field images of the pump and Stokes beams is shown in Figure 57. Clearly the pump near-field image is much larger than the Stokes near-field image. If both of these beams were perfect Gaussian beams, the pump beam would focus to a much smaller spot than the Stokes beam as predicted by Equation (6.19). The fact

that this is not the case indicates that the Stokes beam has a much better beam quality than the pump.

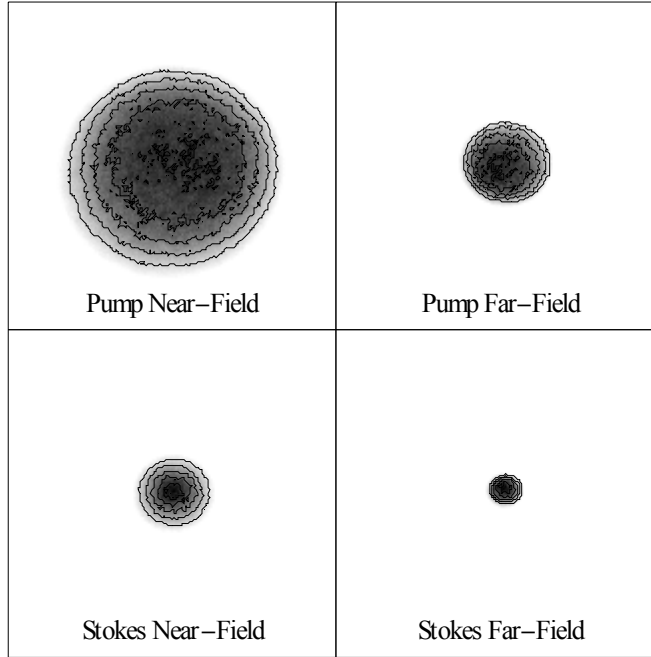


Figure 57: Near- and Far-field images of the pump and Stokes beams transmitted through a 300 m multimode fiber.

A more rigorous analysis can be completed by fitting the spot size of the real beam as a function of position to Equation (6.19). The spot sizes along with the least squares best fit are shown in Figure 58. This analysis is complicated by the fact that the wavelength difference  between the first and last observed Stokes order is nearly 100 nm or 20%. The conservative approach taken here assumed all Stokes power was found in the first order beam at 545 nm thus overestimating the value of  $M^2$ . This analysis results in an  $M^2$  value of  $2.4 \pm 0.3$  for the Stokes beam and an  $M^2$  of  $20.7 \pm 1.0$  for the pump beam. The error in the measured values takes into account the imperfect fit of the beam size to the

measured values. It neglects the error in the measurement of the pump and Stokes beam diameters and the error induced by assuming that the Stokes beam is composed of a single frequency.

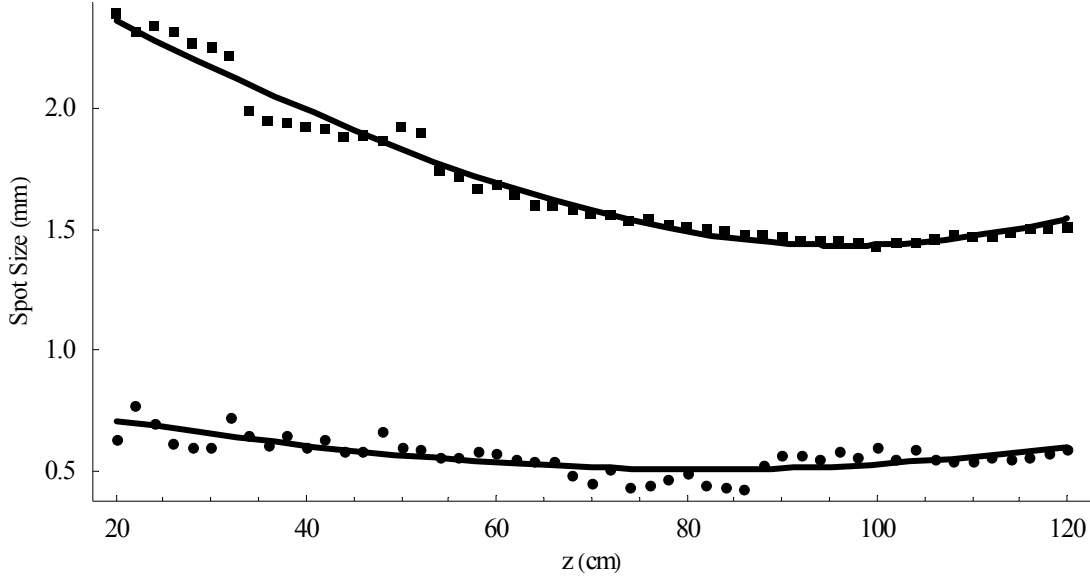


Figure 58: Circles (squares) indicate the measured size of the Stokes (pump) beam at various distances from the lens. The solid lines show the best fit to the data points.

Figure 59 shows an example of the transmitted spectrum. Up to seven Stokes shifts were observed, each separated by approximately  $440 \text{ cm}^{-1}$ . Considerable spectral broadening was noticed with each higher Stokes shift. The bottom portion of this figure shows the spatial characteristics of the different modes as imaged after the diffraction grating. The spectral broadening of successive Stokes shifts makes a fit to a two dimensional Gaussian beam pointless, but the beam size can still be quantitatively analyzed along the vertical dimension.

This was completed for far-field images of the pump and Stokes beams at various fiber lengths. Each image was examined for a pump and Stokes beam. The relative

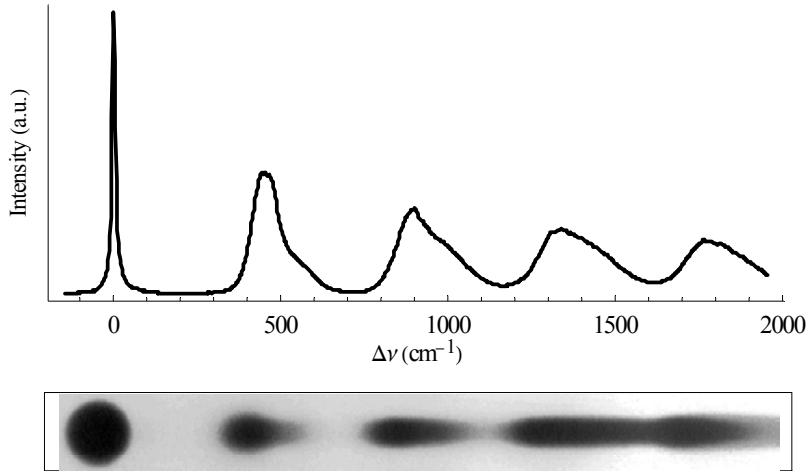


Figure 59: (Top) The spectrum of the beam transmitted through the fiber. (Bottom) The spectrally dispersed near-field image of the transmitted beam.

power in each spectral component was measured by adding the intensity in each pixel around the beam. Images in which the Stokes beam had less than 25% of the power of the pump beam were discarded to eliminate images dominated by noise. The remaining images were evaluated to determine the diameter of the pump and Stokes beams. The measurement was completed by integrating the power along the entire horizontal axis and integrating up and down from the center of the beam until 59% of the power was contained. This vertical height represents the full-width-half-maximum if the beam profile were a perfect Gaussian.

The measured far-field beam diameters are shown in Figure 60(a) as a function of the fiber length. In all cases the Stokes beam is considerably smaller than the pump beam indicating significant beam cleanup. The spot size of the far-field image is the Fourier transform of the collimated beam, or equivalently, that of the aberration on the divergent spherical wave emanating from the fiber facet. Thus the far-field spot size is a measure

of the spatial frequency content of the collimated beam. Consequently, for a given near-field beam size, the far-field spot size is a meaningful measure of the beam quality.

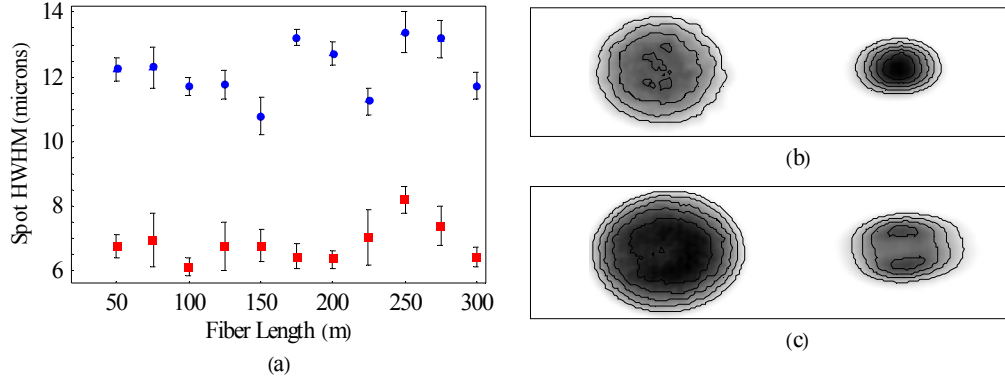


Figure 60: (a) Spot size of the pump (circles) and first order Stokes (squares) beams at the fiber facet. (b,c) Pump (left) and Stokes (right) intensity distributions for a 300 m and 75 m fiber respectively.

At short fiber lengths, the Stokes beam intensity is expected to better match the pump intensity. Although there is no indication of this in the figure, different mode shapes were observed in the Stokes output at fiber lengths below 100 m. Figure 60(b and c) shows a representative close-up of the pump and Stokes beams for long fibers ( $\sim 300$  m) as well as the same image in relatively short fibers ( $\sim 75$  m).

### 6.3.3. Conclusions

Since a real beam diverges faster than a Gaussian with the same waist by a factor of  $M^2$ , the intensity of a real beam drops by a factor of  $M^4$  compared to a Gaussian beam. This demonstrates how important beam quality is to the propagation of high intensity beams. The quality of the input beam was not measured. However, it could be at least as aberrated as the transmitted pump and still be efficiently coupled into the fiber. Assuming a pump with this poor beam quality was used, the results of the SRS beam

cleanup experiment show that the Stokes beam could illuminate a target with an intensity that is 74 times greater than that expected by the pump beam with similar power. Of course the pump to Stokes conversion is not 100% efficient. However, based upon the increase in beam quality, the efficiency only has to be greater than 1.3% to obtain an increase in the intensity on target.

The results shown in Figure 60(a) illustrate that the spot size of the Stokes beam does not significantly change in fibers down to 50 m and that the Stokes beam is significantly smaller than the pump beam. Fibers longer than 100 m consistently generated Stokes beams with Gaussian intensity distributions. This provides strong evidence that stimulated Raman scattering in long fibers produces a clean beam similar to the beam cleanup seen with SBS. However, there is clearly a transition point between long and short fibers in which the beam cleanup properties are lost and higher order modes are excited. Nevertheless, down to the shortest fiber measured (50 m), the Stokes beam always appeared to have a much smaller spot size than the pump beam. These observations are consistent with those made by Chiang in which several fiber modes were observed in a 30 m fiber [25].

Forward SRS, as used in this experiment, allows the use of short laser pulses. But it also allows four wave mixing to significantly reduce the second order Stokes threshold. Although this did not appear to affect the Stokes beam diameter, it does broaden the spectrum of the Stokes beam. This could possibly be reduced through an appropriate design of a long period grating or an absorbant that could eliminate the second Stokes

beam while not affecting the pump or first order Stokes beams. These concepts are explored in more depth in the chapters on SRS reduction in fiber lasers.

Additionally, the forward scattering scheme in a non-polarization preserving fiber provides no means to control the polarization. Even in a backward scattering design, the greater Stokes shift as compared to SBS increases the chromatic dispersion reducing the maximum fiber length that could be used while maintaining the pump polarization, although this point requires experimental verification.

It can be concluded from the experiments described above that stimulated Raman scattering could be used as a substitute for SBS in an operational beam cleanup system. Although it introduces its own set of problems, this would significantly reduce the spectral constraints on the lasers needed in a beam combining or beam cleanup design.

## 7. SRS Reduction Using Intercavity Dopants

### 7.1. Background

Fiber lasers are becoming increasingly popular. The active region is so small that it can easily handle high power beams without significant thermal gradients that can cause fracture or thermal lensing. The low loss and high beam confinement can also reduce laser threshold allowing for novel materials with low gain coefficients to be used in laser devices [11]. Using carefully chosen fiber geometries can also ensure that high spatial quality beams are excited. For example, double clad fibers accommodate highly aberrated pump beams and yet ensure single mode laser beams. In these fibers the inner core is doped with the active element, often ytterbium, and has a small enough diameter that it only allows the  $LP_{01}$  mode to be transmitted at the laser wavelength (see Figure 61). The first cladding layer has an index of refraction that is only slightly lower than that of the core. This region is used to transmit the pump light. It is large enough that it supports a multimode beam, but is not doped with the active laser ion, so little light is absorbed outside of the core. The second cladding region has an index of refraction less than that of the first cladding region. Its main purpose is to guide the pump light down the fiber.

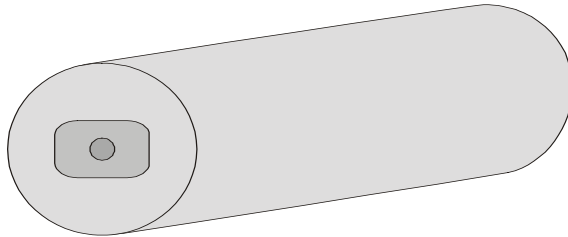


Figure 61: Double clad fiber

Although this complicated fiber geometry ensures that the laser beam oscillates in a high spatial quality, the single mode core is very small resulting in high intensities and observable nonlinear effects. All third order interactions have the potential to be detrimental to a fiber laser system, but stimulated Raman scattering is often the limiting nonlinear effect [65]. Many processes, such as four-wave mixing, require phase matching for efficient light conversion, thus in most situations, unless special care is taken, these processes will be insignificant. Stimulated Brillouin scattering, on the other hand, is automatically phase matched in the backward direction. It even has a relatively large peak gain coefficient compared to SRS, but the gain bandwidth is very narrow ( $\sim$ 100 MHz) and typical fiber lasers are spectrally broad, due to inhomogenous broadening in the amorphous glass host [11]. Figure 62 illustrates the typical spectral broadening associated with glass. The plot shows the emission spectra for Nd in YAG, a crystal, and amorphous SiO<sub>2</sub>. In comparison to SBS, SRS has a very broad gain bandwidth ( $\sim$ 30 THz [3]), which is large enough to compensate for the lower peak gain. The entire laser spectrum can work together to pump a single Raman Stokes beam causing SRS to typically have a lower threshold than SBS.

Since fiber lasers are typically not extremely long ( $\sim$ 1-10 m), it takes a lot of power to generate SRS, but fiber lasers are getting more powerful every year. In 1997, the highest reported cw output from double-clad fiber lasers was 35 watts. In 1998 that jumped to 55 watts and in 1999 a fiber laser generating 110 watts was reported [66]. At power levels this high, SRS is significant even though the fiber is short. Lang reported significant output in the Stokes beam at power levels exceeding 100 watts when presenting details of an 80-watt fiber laser he developed [67].

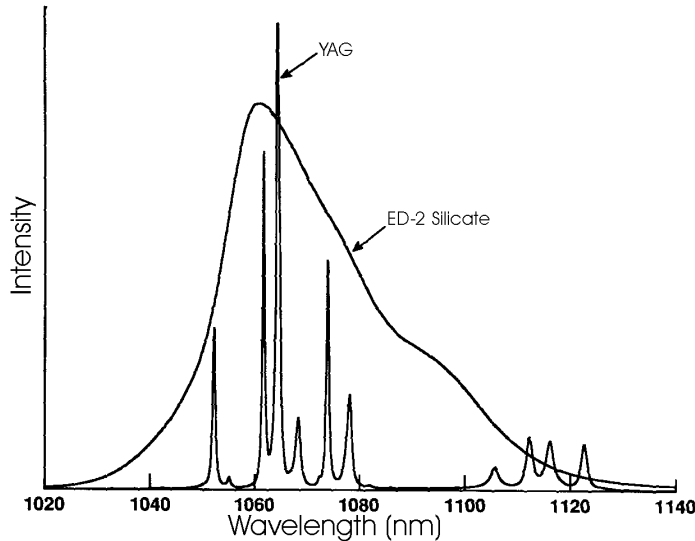


Figure 62: Emission Spectrum of Nd in a crystal and in glass [11].

Pulsed laser systems are even more susceptible to stimulated Raman scattering.

Typical laser radar systems, for example, only require a few watts of average power, but delivered in pulses less than about 10 ns. Even at pulse rates of tens of kHz, the peak powers observed are many kilowatts. Gapontsev *et al.* [68] have been investigating this issue with very good success in a master oscillator power fiber amplifier configuration. They were able to reduce nonlinear effects by increasing the master oscillator spectral width and tapering the core size of the fiber amplifier such that as the pulse increased in power, the power density remained low. Yet even with these modifications SRS was still noticeable in the output when they reached their maximum peak power level of 100 kW.

The negative effects of SRS are clear when observing how it depletes the pump beam in a fiber. The coupling between the Stokes and pump beams is described by Equation (3.12), repeated here for simplicity.

$$\begin{aligned}\frac{\partial I_s}{\partial z} &= g_r I_p I_s - \alpha_s I_s \\ \frac{\partial I_p}{\partial z} &= -\frac{\omega_p}{\omega_s} g_r I_p I_s - \alpha_p I_p\end{aligned}\tag{7.1}$$

Assuming the absorption at the pump and Stokes wavelengths is negligible and the Stokes intensity at the front of the fiber is insignificant relative to the pump intensity,  $I_{p0} - I_{s0} \approx I_{p0}$ , the pump beam intensity at the end of the fiber,  $z = L$ , is

$$I_p(L) = \frac{I_{p0}}{1 + \frac{I_{s0}}{I_{p0}} \frac{\omega_p}{\omega_s} \exp(g_r I_{p0} L)}.\tag{7.2}$$

Even a relatively small initial Stokes intensity (spontaneous scattering off thermal phonons for example) can induce significant loss in high power beams.

If the Stokes beam never becomes strong enough to cause significant pump depletion, the solution of Equation (7.1) shows that the Stokes beam intensity distribution in the fiber grows exponentially.

$$I_s(z) = I_{s0} \exp\left[\frac{g_r I_{p0}}{\alpha_p} \left(1 - \exp(-\alpha_p z)\right) - \alpha_s z\right].\tag{7.3}$$

This is only valid when the total power converted into the Stokes beam is small relative to the pump. Assuming this is so, Equation (7.3) can be treated as a small perturbation to the pump beam and used in Equation (7.1) to predict the effect of the Stokes generation on the pump power. If the absorption at the pump wavelength is negligible, the pump power transmission is

$$T_p = \exp \left\{ \frac{g_r I_{s0} \omega_p}{(g_r I_{p0} - \alpha_s) \omega_s} \left[ 1 - \exp \left[ (g_r I_{p0} - \alpha_s) L \right] \right] \right\}. \quad (7.4)$$

From Equation (7.4), it becomes apparent that as the attenuation of the Stokes beam increases, the transmission of the pump beam increases. This is particularly obvious as the fiber length is increased to infinity, at which point the pump transmission becomes a step function, transitioning from 0% when the Stokes absorption is less than the Raman gain,  $g_r I_{p0} < \alpha_s$ , to 100% when the Stokes absorption is greater than the Raman gain.

The absorption in a typical fiber is shown in Figure 63. This shows no special absorption features near 1.12-1.15 microns that will suppress SRS in Nd or Yb high power lasers. Novel concepts, however, have been used to increase the loss at the Stokes wavelength. For example, Sylvestre *et al.* used a second laser beam to induce loss at the Stokes wavelength [69, 70]. When the second pump beam was frequency tuned to exactly twice the Stokes shift, any Stokes radiation generated by the first pump beam was quickly converted to the second order Stokes beam, increasing the amount of pump power that could be transmitted through the fiber.

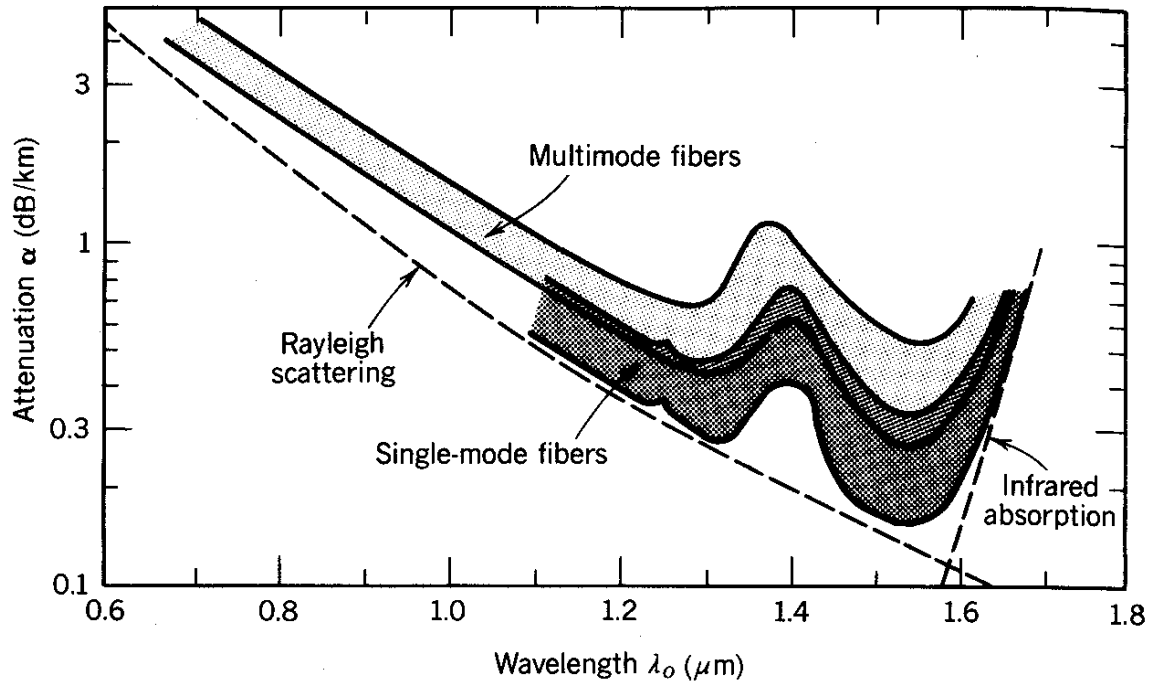


Figure 63: Absorption of typical optical fiber [13].

In another scheme, stimulated scattering beyond the first order beam was suppressed by bending the fiber [71]. Bend induced loss acts as a short pass filter with the cutoff wavelength determined by the bend radius. With the proper bend choice the second order Stokes beam would experience high attenuation with minimal effect on the first order Stokes and the pump beam. This was verified experimentally showing that the threshold for second order SRS was increased by greater than a factor of two and the power in the first order beam was increased by more than 40%.

Petrov *et al.* modeled and demonstrated second order SRS suppression using a capillary waveguide [72]. A capillary waveguide uses a liquid core with a glass cladding. If the index of refraction of the liquid is strongly dispersive, the index can be made to be higher than the glass cladding for the pump and Stokes beam, but lower than the cladding for the second order Stokes beam. For such a system, the second order beam is not

guided and will have a very high threshold. Experimentally, a 30-35% increase in the first order Stokes beam was achieved when the second order beam was suppressed.

Another method that has shown promise in suppressing stimulated Raman scattering is to dope the nonlinear material with an element that has an absorption line near the Stokes order that must be suppressed. Urata *et al.* doped praseodymium into a lanthanum tungstate crystal [73]. Pr has an absorption feature near 600 nm which is very close to the second order stokes beam generated through SRS pumped with a frequency doubled Nd:YAG laser at 532 nm. This method showed that the second order Stokes threshold increased by at least a factor of two without a significant effect on the first order threshold.

The spectral broadening of material transitions in a glass fiber can complicate suppression of stimulated Raman scattering. If the transition is not sufficiently far away from the absorption peak, the tail in the absorption line will reduce transmission of the pump beam, negating the effects of SRS suppression. On the other hand, the long interaction lengths in a fiber relax the requirements on the absorption at the Stokes wavelength to significantly affect the SRS threshold.

The primary interest of this chapter is to increase the power that can be generated by an ytterbium or a neodymium fiber laser by limiting the adverse affects of SRS. Yb and Nd are common dopants used for high power fiber lasers and amplifiers [74]. These lasers operate near 1 micron with a peak in the Stokes gain spectrum that is shifted about 55 nm to longer wavelengths. They are pumped near 920 or 980 nm [10]. There are a couple of important requirements on any dopant that could be used to suppress stimulated

Raman scattering. The dopant should minimally affect operation of the laser. This means that there should be little absorption at both the laser pump wavelength and the lasing wavelength. The second requirement is that it must absorb at the Stokes wavelength to increase the SRS threshold. The rest of this chapter will describe the modeling used to predict a substantial increase in SRS threshold for light at 1.064 and 1.090 microns transmitted through a silicate glass fiber doped with Holmium.

## 7.2. Theory

### 7.2.1. Dopant Characterization

The absorption characteristics of holmium in silicate glass has all of the features required for suppression of the first order Stokes peak associated with neodymium and ytterbium doped fiber lasers. The  $^5I_8 - ^5I_6$  transition of holmium in glass is centered around 1.152 microns [75]. Although this is not perfectly centered on the Stokes peak for both neodymium and ytterbium lasers, it has a relatively broad tail that affects the Stokes beam of both. Figure 64 shows the transmission of light through a 5 mm silicate glass window doped with 2 mol% holmium. The inset marks the location of the pump for the fiber laser, laser output, and the first order Stokes beam for an  $\text{Yb}^{3+}$  doped laser. The window was not polished to have an optically flat surface, thus scattering as well as the Fresnel reflection at the window surfaces account for part of the deviation of the pump and laser transmission from 100%.

The output of a neodymium laser is centered near 1.06 microns with a first Stokes gain peak at 1.117  $\mu\text{m}$ . Figure 65(a) shows the holmium absorption spectrum along with the Raman gain spectrum showing considerable misalignment of the two, yet the material

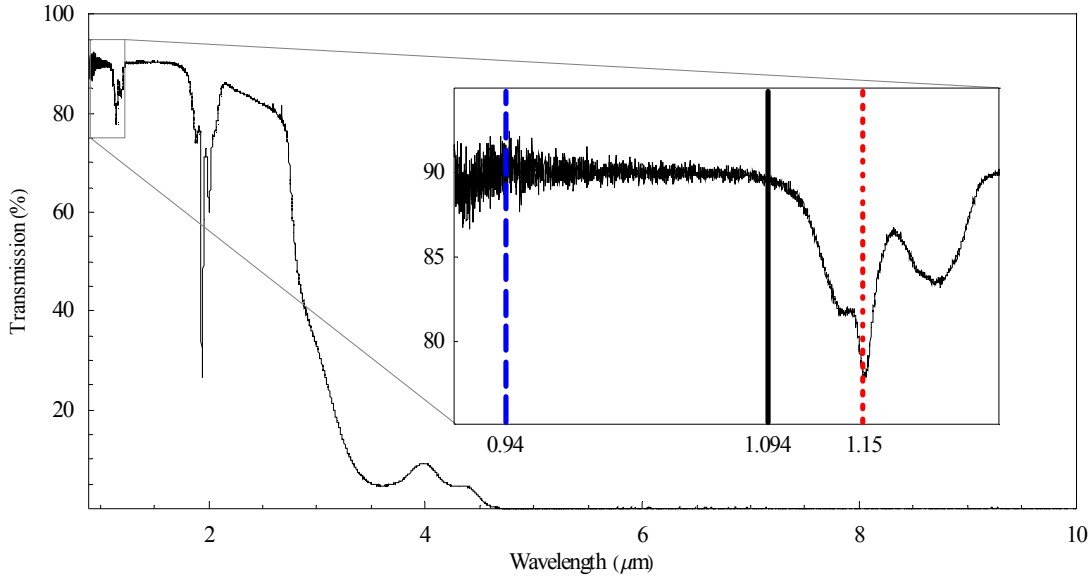


Figure 64: Transmission of a 5mm thick silicate glass window doped with 2 mol% of Ho. The dashed line indicates the location of a typical laser pump, the solid line shows the wavelength of the laser, and the dotted line represents the first order Stokes beam.

absorption is still 22.89 dB/(m mol%) greater at the Stokes wavelength than at the laser wavelength. For comparison, a standard telecom fiber at 1.064  $\mu\text{m}$  absorbs less than 0.001 dB/m.

More effective suppression of the Stokes radiation may be expected using an Yb laser. Ytterbium lasers operate from 1.06  $\mu\text{m}$  to  $\sim$ 1.10  $\mu\text{m}$  [10]. Some of the highest power cw fiber lasers to date have been operated using ytterbium lasing at 1.12  $\mu\text{m}$  [66]. This pushes the Raman gain spectrum further into the infrared where it overlaps the holmium absorption curve more effectively. The Raman suppression will be most efficient near 1.094  $\mu\text{m}$ , forcing the Stokes gain peak to overlap the holmium absorption peak at 1.15 microns. The Raman gain curve and Holmium absorption are plotted in Figure 65(b).

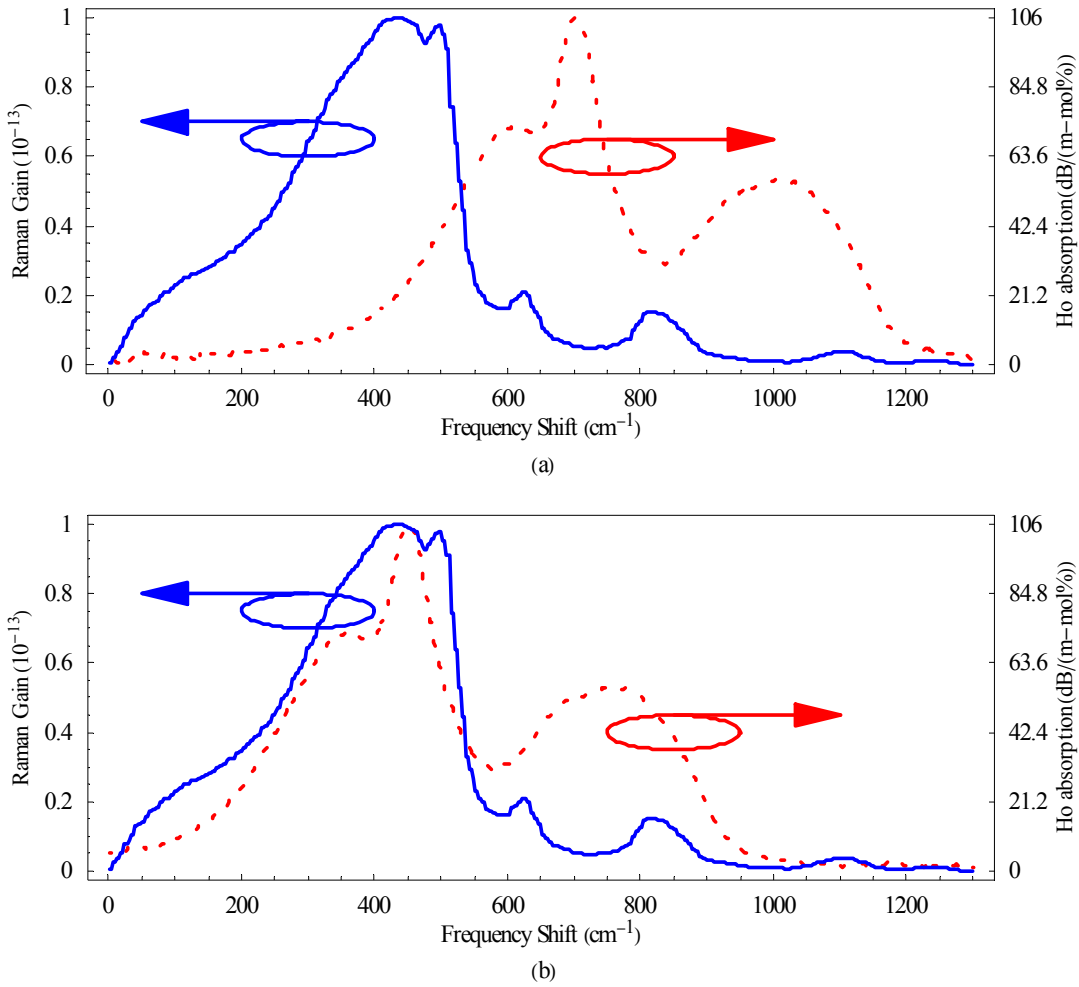


Figure 65: Holmium absorption in silicate glass (dotted line) along with the Raman gain (solid line) as a function of the frequency shift from a neodymium pump beam at 1.064 microns (a) and as a function of the frequency shift from a ytterbium pump beam at 1.094 microns (b).

### 7.2.2. Threshold Calculation

Smith defines a convenient form of the SRS threshold. In the limit of no pump depletion [18] the input intensity that yields an equivalent Stokes beam at the exit facet is identified as the threshold. This definition is relatively simple to implement. Since the assumption is made that the pump power in the fiber is only affected by absorption, the differential equations coupling the pump and Stokes beams can be solved

analytically. Equation (7.3) gives the intensity of one spectral component of the Stokes beam at the exit facet of the fiber for a given pump intensity. Assuming the pump beam is monochromatic, the only terms on the right hand side with any spectral dependence are the Raman gain and the Stokes absorption, resulting in the total Stokes power of

$$P_s = P_{s0} \int \exp \left[ \frac{g_r(\nu) I_{p0}}{\alpha_p} (1 - \exp(-\alpha_p L)) - \alpha_s(\nu) L \right] d\nu \quad (7.5)$$

where  $A_{eff}$  is the effective area of the fiber and the integration is performed over the Raman gain bandwidth.  $P_{s0}$  is the power of the noise Stokes photons that give rise to the stimulated scattering. It is approximated by the intensity of a single photon per second transmitted through the fiber. The integration is performed over all frequencies for which the Raman gain is greater than zero. The interpretation of the remaining terms has not changed from their earlier uses.

Since the spectral dependence of the Raman gain is not described by an analytical function, Equation (7.5) is best evaluated using a numerical integration.

$$P_s = P_{s0} \Delta \nu \sum_i \exp \left[ \frac{g_r(\nu_i) I_{p0}}{\alpha_p} (1 - \exp(-\alpha_p L)) - \alpha_s(\nu) L \right] \quad (7.6)$$

where  $\nu_i$  are the frequency components for which the Raman gain is tabulated and  $\Delta \nu = \nu_{i+1} - \nu_i$  is the resolution of the tabulation. Stimulated scattering threshold is found by evaluating Equation (7.6) for increasing pump intensities,  $I_{p0}$ , until the output Stokes power is equal to the input pump power.

This analysis was completed at various holmium dopant levels for a fiber pumped at 1.064  $\mu\text{m}$  and at 1.09  $\mu\text{m}$ . A 100 m length of Corning SMF-28 fiber with an 8-micron mode field diameter was modeled for the calculation. The undoped threshold was 100 watts. Adding holmium to the fiber increased the threshold almost linearly resulting in Figure 66.

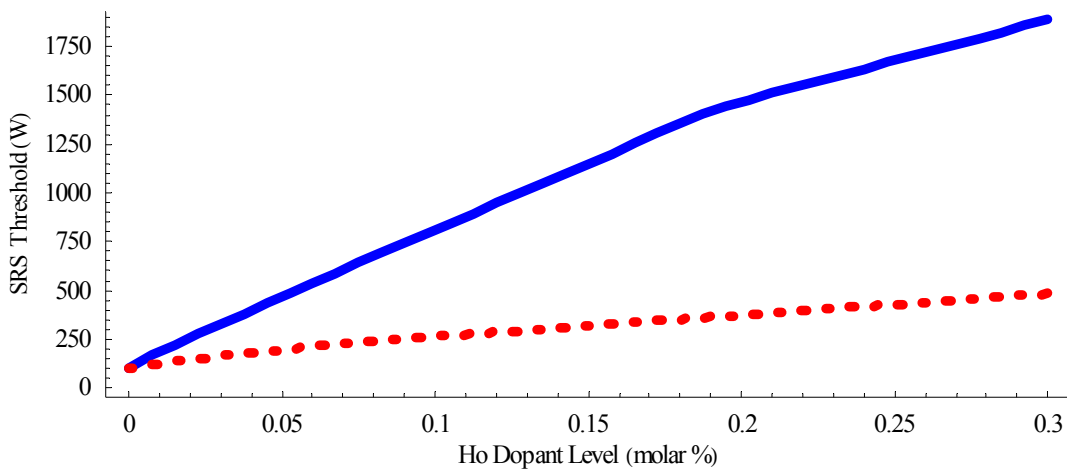


Figure 66: The threshold for SRS generation pumped at 1.064 microns (dashed line) and at 1.09 microns (solid line) calculated versus the molar % of holmium doped into the fiber.

### 7.3. Conclusions

Figure 66 shows that doping a fiber with holmium can significantly affect SRS threshold. A factor of two increase in the threshold was achieved with a pump beam at 1.064 (1.094)  $\mu\text{m}$  using a dopant level of 0.053 (0.012) molar percent of holmium. However, the effects of the dopant on the pump beam have not been tested. The poor optical quality of the holmium doped silicate windows prevented a quantitative measure of absorption at the pump wavelengths. Although absorption is 4.95 dB/(m mol%) greater at 1.09  $\mu\text{m}$  than at 1.064  $\mu\text{m}$ , the greater absorption at the Stokes peak

compensates for the extra loss at 1.09 microns. Absorption at the Raman gain peak is 79.4 dB/(m mol%) greater when the laser operates at 1.094  $\mu\text{m}$ .

The slope of the curves in Figure 66 is determined by the ratio of the SRS gain to the holmium absorption at the dominant Stokes wavelength. At low dopant levels, most of the Stokes power is contained in frequencies near the peak of the Stokes wavelength, but at high dopant levels, the peak of the Raman gain is suppressed and the Stokes beam is generated at frequencies near the edge of the gain spectrum. The kink in the slope is due to a discrete shift in the dominant SRS peak.

Several factors that affect integration of this Raman suppression technique in a fiber laser were ignored in the analysis presented here. First, the thresholds reported in Figure 66 do not represent the maximum power achievable in a fiber laser before the effects of SRS are visible. Depending on the reflectivity of the output coupler and the fiber length, the oscillating power in the cavity could vary considerably along the fiber length and could be significantly stronger than the power exiting the fiber; hence there is a strong cavity dependence that will affect the power level that can be achieved before the onset of SRS.

Secondly, although the attenuation at the pump and laser frequencies was considered, the addition of a dopant to the laser cavity can have other unforeseen effects. Ytterbium has been used to sensitize holmium to InGaAs laser diodes near 940 nm. This transition in ytterbium is broad and once excited to that level, it easily transfers energy to the holmium ion. This energy transfer process is used to increase holmium luminescence in the green [76-78] and to generate lasers operating at 2.1 microns [79, 80]. The rate of

energy transfer from the ytterbium to the holmium depends on the concentration of both ions. According to Zhang *et al.* [77, 78], the rate increases linearly with holmium concentration and quadratically with ytterbium concentration, so even if the pump absorption does not limit the holmium dopant level, the energy transfer between the holmium and ytterbium laser will.

Finally, the laser dopants as well as the holmium will affect the Raman gain spectrum. For low doping levels, the silicate glass will dominate the Raman spectrum. However, at high dopant levels, new resonant Raman peaks may appear that are not necessarily suppressed by holmium. These peaks would require consideration in a laser system.

Clearly there are many issues that must be addressed before SRS suppression with a holmium intercavity dopant is feasible in a fiber laser system. However, some of the theoretical groundwork has been laid showing a remarkable improvement in SRS threshold. At 0.3 molar % doping level, a 100 m long ytterbium laser is predicted to be able to operate at 19 times the power level that an undoped fiber could support.

## **8. SRS Reduction Using Long Period Gratings**

Although introducing a dopant into a fiber laser was shown in Chapter 7 to theoretically increase the Stokes threshold, it is not a flexible solution. Figure 65 showed that a neodymium laser operating at 1.064 microns has a much lower Stokes absorption than an ytterbium laser operating at 1.094 microns. Additionally, operation of the ytterbium laser at longer wavelengths would result in severe absorption of the laser beam. A long period grating on the other hand can be tailored to eliminate the unwanted Stokes beam while minimally affecting the pump beam.

Long period gratings, LPGs, are similar to fiber Bragg gratings in that they are periodic variations in the index of refraction that affect the propagation of light in the fiber. The results of the structures are significantly different though. Fiber Bragg gratings reflect light over a very narrow bandwidth ( $< 1 \text{ nm}$ ) while long period gratings couple light from a specific core guided mode to a cladding guided mode and have much larger bandwidths. In most fibers, cladding guided modes are very lossy thus the long period grading essentially becomes a frequency dependent loss in the fiber (Figure 67).

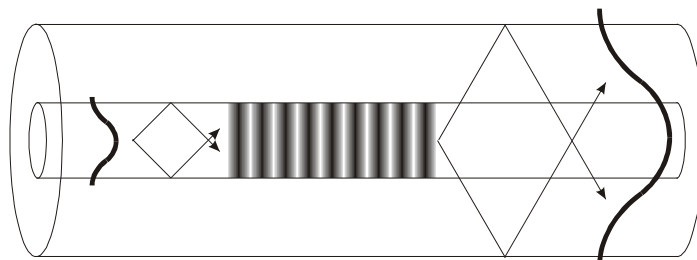


Figure 67: A long period grating couples light out of the core and into the fiber cladding where high losses account for the reduction in transmission.

This method for increasing the loss at the Stokes wavelength is investigated theoretically in this chapter. The spectral characterization of the Raman gain is examined in Section 8.1. In Section 8.2 the design of the long period grating is explained, and conclusions are made in Section 8.3.

## 8.1. Raman Spectrum Measurement

An intense ultraviolet light source can generate a permanent change in the refractive index of a photosensitive fiber. This effect is responsible for long period gratings and can be improved with the addition of certain dopants to the fiber, mainly germanium. To maximize the effect of the LPG on the SRS threshold, a highly photosensitive fiber from StockerYale, PS-SMF-30, was purchased. Jain's group at the University of New Mexico measured the index change in this fiber as well as in a hydrogen loaded standard single-mode fiber and found that it was a factor of 170 greater in the photosensitive fiber. The additional dopants, however, can affect the Raman gain spectrum, forcing a measurement of this spectrum before a final grating design is possible.

### 8.1.1. Experimental Setup

The Raman spectrum was measured using the experimental setup shown in Figure 68. A frequency doubled Q-switched Continuum Powerlite Nd:YAG laser was used as the laser source. Delaying the Q-switch relative to the flashlamp and transmitting the beam through a half-wave plate and a polarizer controlled the laser power. The beam was then coupled into the photosensitive fiber. At the output end of the fiber, a microscope objective collimated the beam, which then propagated through a Raman notch filter that

reduced the pump power. The Stokes beam was then coupled into a fiber bundle attached to a spectrum analyzer and an optical multichannel analyzer, with a resolution of  $14 \text{ cm}^{-1}$ .

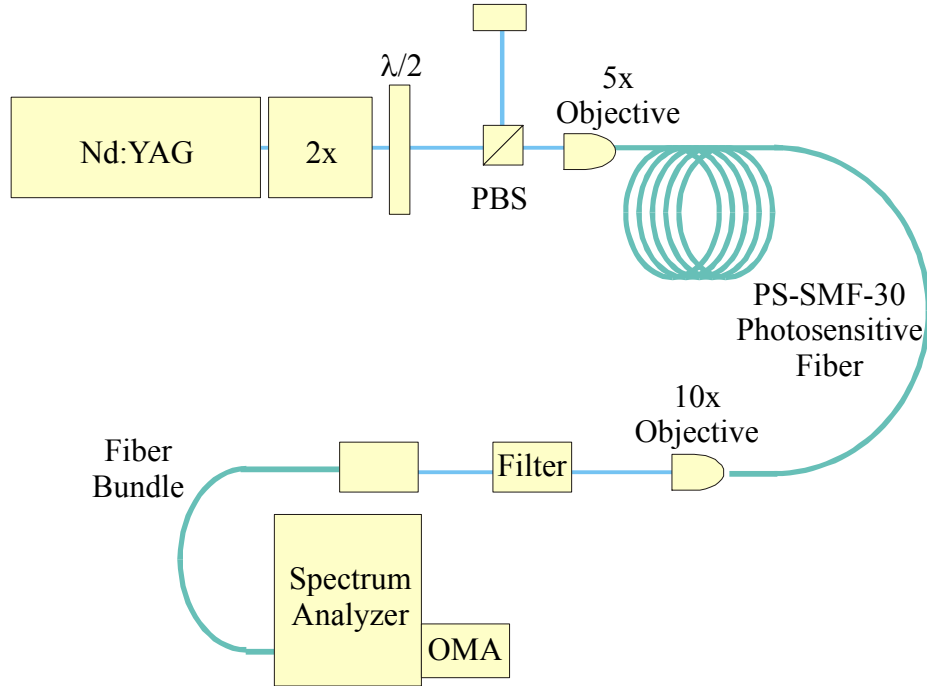


Figure 68: Schematic for Raman spectrum measurement.

The experiment was performed at various fiber lengths between 0.5 and 200 m. The pump power was also varied. However, it could not be controlled well because the laser was operated with the Q-switch delay not optimized to reduce laser power. To minimize the random variations from one measurement to the next, 100 spectral scans were taken at each power level and averaged. The measurement was further complicated by the high power of the laser. A small percentage of the beam could easily damage the front fiber facet.

### 8.1.2. Results

A complicated Stokes spectrum is revealed in Figure 69(a). This data was collected using a 0.5 m long fiber. At low power levels, peaks in the Stokes spectrum are found at  $265\text{ cm}^{-1}$  and  $480\text{ cm}^{-1}$ . As the power increases, these peaks shift to longer wavelengths,  $290\text{ cm}^{-1}$  and  $540\text{ cm}^{-1}$  respectively, and another peak at  $440\text{ cm}^{-1}$  appears in the spectrum. Figure 69(b), shows the Stokes spectrum after transmission through a slightly longer fiber, 1 m. This increase in interaction length reduces the threshold for SRS. The results show that as the  $440\text{ cm}^{-1}$  line grows, the  $290$  and  $540\text{ cm}^{-1}$  peaks remain relatively constant. Even longer fibers have confirmed this trend. The Stokes spectrum of a 200m fiber, shown in Figure 69(c), demonstrates that the  $440\text{cm}^{-1}$  peak dominates the others.

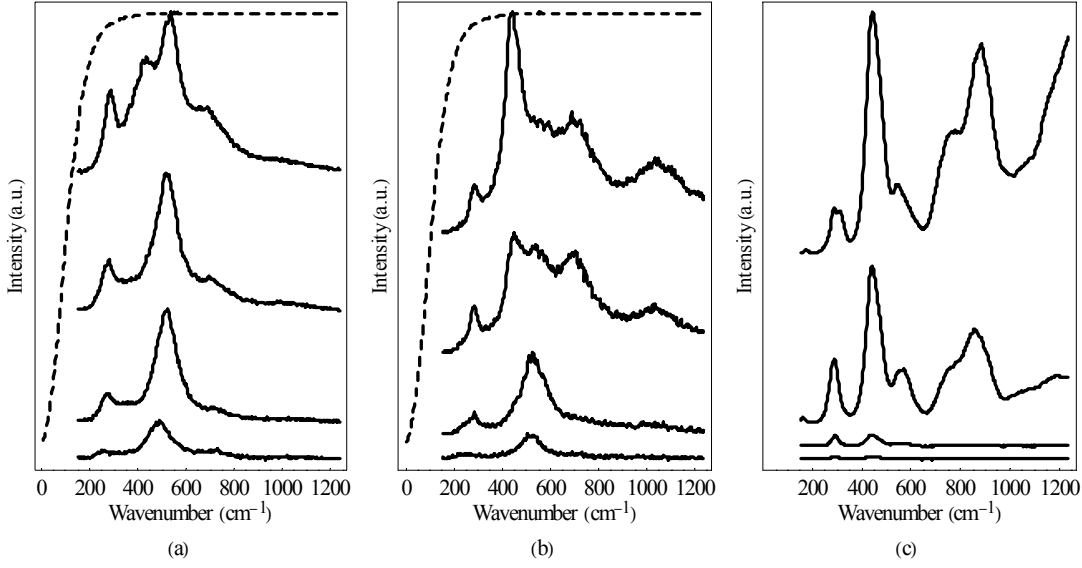


Figure 69: Stokes spectra at different pump power levels in (a) a 0.5 m fiber, (b) a 1 m fiber, and (c) a 200 m fiber. The dashed lines in (a) and (b) indicate the transmission spectrum of the Raman notch filter used in those experimental setups to attenuate the pump beam.

The growth of a frequency component at  $440\text{ cm}^{-1}$  is expected based upon the Raman gain spectrum of both  $\text{SiO}_2$  and fused  $\text{GeO}_2$  (see Figure 70). Conversely, the Stokes peaks at  $290$  and  $540\text{ cm}^{-1}$  and their variation with pump power is unexplained by the Raman gain spectrum alone. Qualitatively, however, sidelobes of the pump beam generated through modulation instability (MI) have many of the same characteristics as these two Stokes peaks. Modulation instability is a four-wave mixing phenomenon that is phase-matched through self- or cross-phase modulation [3]. In single mode fibers, MI is typically observed in the anomalous group-velocity dispersion region above  $\sim 1.3$  microns. However, in multimode fibers the pump, Stokes and anti-Stokes components can travel in different fiber modes. The difference in the effective indices of these modes can offset the material and nonlinear dispersion [81, 82]. Because the nonlinear dispersion is intensity dependent, the frequencies for which the beams are phase matched changes with pump power, thus explaining the variation in the Stokes spectrum at different power levels.

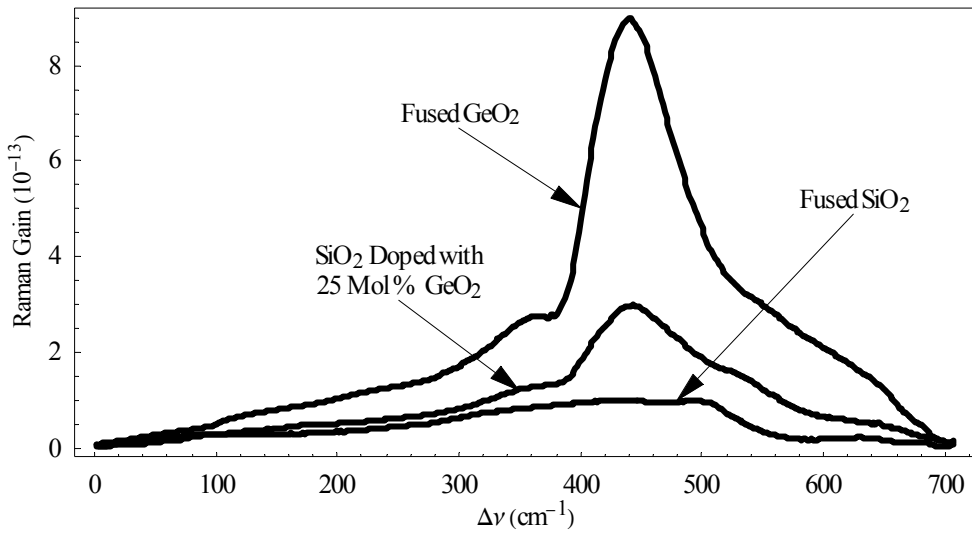


Figure 70: Raman gain spectrum for various types and concentrations of dopants [83].

Because of these complications with the measured spectrum and due to the theoretical nature of the research described here, the measured Raman gain spectrum was not used in the analysis described below. The PS-SMF-30 fiber is known to have a high concentration of germanium thus for the purpose of theoretically demonstrating the affect of a long period grating on stimulated Raman scattering, the gain spectrum of SiO<sub>2</sub> doped with 25 molar % of GeO<sub>2</sub> is used.

## 8.2. Long Period Grating Design

### 8.2.1. Theory

The LPG design hinges upon a correct calculation of the transmission characteristics of a long period grating. The steps laid out by Erdogan [12, 16] were used to determine the LPG transmission. These calculations are clearly explained and quite intricate. For these reasons, only the critical highlights are mentioned here. The results of these calculations will be used to design an appropriate LPG to reduce SRS and theoretically demonstrate its expected effect on the SRS threshold.

As mentioned previously, a long period grating couples a core-guided fiber mode to a cladding guided fiber mode. In essence, it is a volume hologram in the fiber core with the core-guided mode as the reference wave and the cladding-guided mode as the object wave [84]. Thus the grating should have an index variation that precisely matches the interference pattern of the two modes. Such an interpretation immediately demonstrates that the LPG should have a period equal to the beat frequency between the core- and cladding-guided modes. Since both of these waves travel in the same direction, the

grating has a long period relative to that of a Bragg grating in which the reference wave propagates in the opposite direction as the object wave.

Depending on the cladding mode that the beam is coupled into, the period of the grating will change. Figure 4, page 17 of Section 2.2, shows the cladding mode dispersion relation. The independent variable in this figure is the effective index and it is apparent from this graph that over the region shown, the difference between adjacent odd modes increases with mode number. Thus the resonance peaks for higher order modes will be much further apart than those for lower order modes. This is most significant when wavelength regions where high transmission is required surround the desired resonance. For the case at hand, the Stokes light must be eliminated without inducing significant loss at the pump wavelength. Thus using certain cladding modes may be problematic if one of the lower order sidelobes overlaps the pump beam. On the other hand, apodization of the LPG can reduce unwanted sidelobes [84], but would complicate the analysis and is not attempted here.

The  $LP_{01}$  fiber mode will efficiently couple to only the  $HE_{1n}$  fiber modes, where  $n$  is an odd number. All of the  $HE_{1n}$  cladding modes are circularly symmetric, a characteristic that is required to produce an interference pattern with the  $LP_{01}$  core mode that approximates a flat grating. Additionally, as can be seen by Figure 5, page 18 of Section 2.2, the odd modes have local maxima at the fiber core and overlap the fundamental core-guided mode much better than the even modes. As the mode number increases, this generalization loses its validity, but it is still important. The overlap of the core and cladding modes is closely tied to the coupling constant, which is proportional to the

efficiency with which the core mode is coupled to the cladding mode. Figure 71 shows the coupling constant from the core mode to various cladding modes. As this plot shows, up to relatively high cladding mode numbers, the beam is coupled to the odd modes much stronger than to the even modes. Additionally, it becomes apparent that the peak in the coupling constant of the odd modes is not when the  $LP_{01}$  core mode is coupled into the  $HE_{11}$  cladding mode, but rather into a higher odd mode. Although using this mode would allow for a grating with a wider spectral bandwidth, complications result from lower order modes overlapping the pump beam.

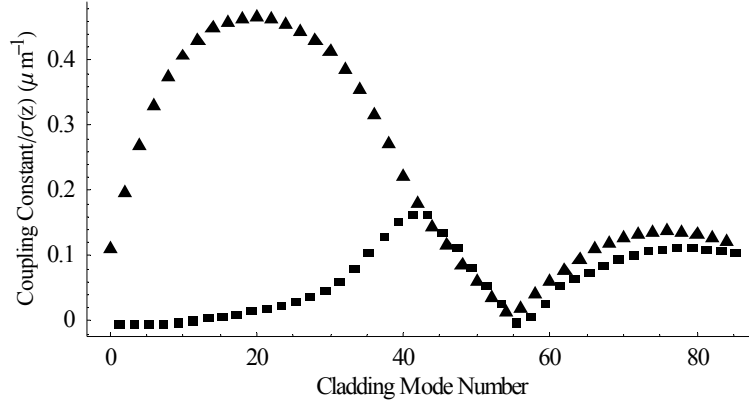


Figure 71: Proportionality constant for the efficiency of the coupling between the  $LP_{01}$  and cladding modes [12]. The odd cladding modes are designated with triangles. The even cladding modes are designated with squares.

The transmission characteristics of a long period grating are sensitive to the depth of the index grating written into the fiber. This can be problematic since the central wavelength must overlap the peak of the Raman gain curve to strongly affect the SRS threshold. However, after the grating is written into the fiber, the transmission can be adjusted slightly. It has been shown that by etching the cladding slightly, thus slightly changing its radius, the resonance wavelength will increase [85].

Another complication with the design, as implemented here, is that the analysis neglects the fact that the PS-SMF-30 fiber supports many core-guided modes at 1.064 microns. This will clearly change the results, since the LPG is designed only to induce coupling between the  $LP_{01}$  mode and the cladding modes. There will be accidental resonances between higher order core-guided modes and the cladding. However, the position of these resonances has not been calculated and it is unlikely that any of these will be useful in the suppression of SRS. Under most situations, however, the fiber laser or amplifier in question will only support a single fiber mode to ensure a high quality laser beam. Additionally, as demonstrated in Section 6.2, even in multimode fibers, SRS was generated predominantly in the  $LP_{01}$  mode. Thus the application of a long period grating to this problem is appropriate.

Once the transmission of the long period grating and the Raman gain spectrum is determined, they can be used to calculate the threshold for SRS in a way that is similar to that outlined in the previous chapter. Differences between the two cases arise from the fact that rather than absorption along the fiber, the loss is localized to discrete points. To account for this, each section of fiber can be treated independently. The power in the Stokes beam will initially grow unimpeded, seeded by the spontaneous scattering in the fiber. The beam will then pass through the long period grating and power will be lost. This reduced Stokes power is then the seed for the next stretch of unimpeded Stokes growth. This pattern continues until the beam exits the fiber and from Equation (7.6) the total Stokes power is given by

$$P_s = P_{s0} \Delta \nu \sum_i T(\nu_i)^n \exp \left[ \frac{g_r(\nu_i) I_{p0}}{\alpha} (1 - \exp(-\alpha L)) - \alpha L \right]. \quad (8.1)$$

In this equation the transmission of the grating at a frequency  $\nu$  is given by  $T(\nu)$ ,  $n$  is the number of gratings in the fiber, and the absorption at the pump and Stokes wavelengths is assumed to be constant,  $\alpha = \alpha_p = \alpha_s$ . The summation over  $i$  is completed to obtain a numerical integration over the frequencies for which there is gain. Finally, the total Stokes power is compared to the pump power. In the same manner as described by Smith [18] and in Chapter 7, threshold is identified as the pump power that produces an equally powerful Stokes beam.

The optimal grating design maximizes the SRS threshold while maintaining a high transmission at the pump wavelength. For the design performed here, the product of the Raman threshold and the transmission at the pump wavelength is maximized relative to the grating period and the grating length. The grating period determines the center wavelength and mode order as described above. The grating length is also critical. Unlike a distributed Bragg reflector, a longer grating does not necessarily result in a stronger coupling. At some point, power will begin to flow back from the cladding mode into the core mode. Thus the LPG should not be greater than this length. For the purposes described here, the grating is slightly shorter than the length resulting in best coupling. A shorter length increases the spectral bandwidth for a better overlap with the Raman gain curve.

### 8.2.2. Results

Using a single grating to maximize the figure of merit described above results in the transmission curve shown in Figure 72(a). The transmission at 1.064 microns is nearly 98%. The Raman gain curve is overlaid to demonstrate the position of the gain peak. The grating characteristics are summarized in Table 8. The SRS threshold was calculated to be 42.1W. This is a factor of 19% greater than the calculated threshold when no gratings are present in the fiber, 35.4 W. The low threshold relative to that calculated in the previous chapter with no dopant in the fiber is a direct result of the increased gain of a germanium doped fiber (see Figure 70).

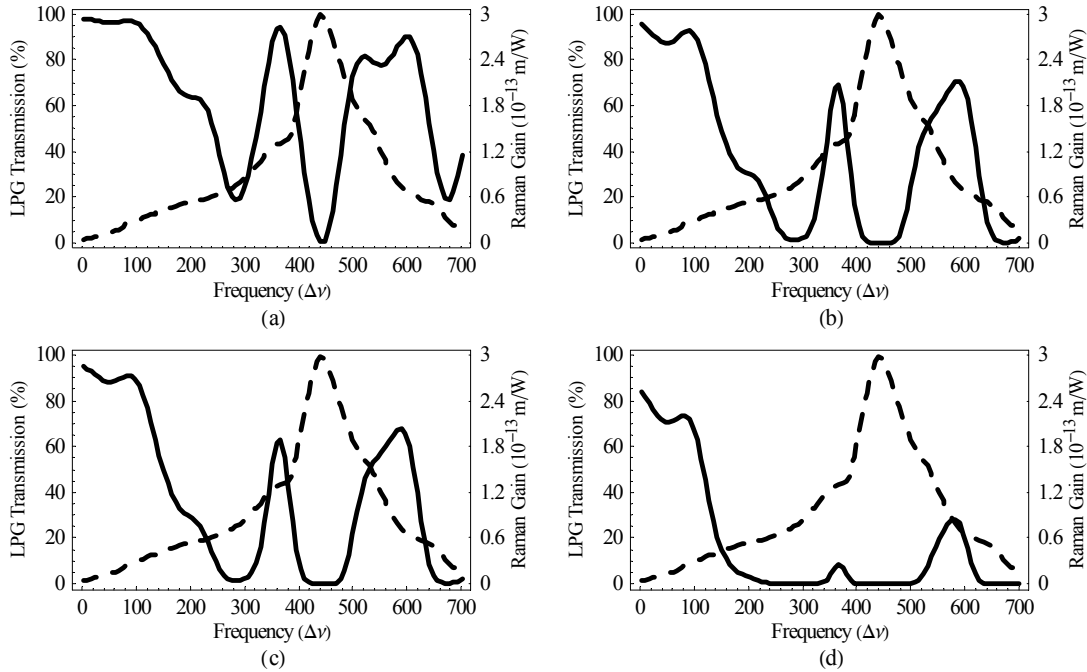


Figure 72: LPG transmission (solid) and Raman gain (dashed) as a function of the frequency difference from the pump beam at 1.064 microns. (a) A single long period grating with the  $\text{HE}_{13}$  mode centered at  $440 \text{ cm}^{-1}$ . (b) A single grating placed at three points in the fiber. (c) One set of three different gratings. (d) Three sets of three different gratings.



Table 8: Critical parameters for several LPG designs.

| Gratings per set                                    | 0    | 1     | 1     | 3     | 3     |
|---|------|-------|-------|-------|-------|
| # of sets   | 0    | 1     | 3     | 1     | 3     |
| Center Grating Period ( $\mu\text{m}$ ) - $\Lambda$ | NA   | 236.6 | 236.7 | 236.7 | 236.9 |
| Grating Length (cm) - L                             | NA   | 1.12  | 1.09  | 1.10  | 1.08  |
| $\Delta\Lambda$ Between Gratings ( $\mu\text{m}$ )  | NA   | NA    | NA    | 0.60  | 1.07  |
| Threshold Power (W)                                 | 35.4 | 42.0  | 51.0  | 52.1  | 72.3  |
| Threshold Increase (%)                              | 0    | 19    | 44    | 47    | 104   |
| Tx @ 1.064 $\mu\text{m}$                            | 100  | 97.7  | 95.6  | 95.0  | 84.4  |

Simply adding more of these gratings will further increase the SRS threshold.

However, for optimal performance, a slightly different design should be implemented when multiple gratings are used. Optimizing the same figure of merit requires a grating with a slightly shorter length and a shifted center frequency. The shorter length widens the spectral width of the grating, which suppresses SRS over the full gain curve better. The depth of the overall transmission dip is maintained by adding the extra gratings to the fiber. The result of optimizing the design for three gratings in the fiber is shown in Figure 72(b) and again the critical characteristics are summarized in Table 8.

Although it is a simple matter to just add more of a single grating to a fiber, the Raman gain curve could be better matched by a set of LPG's, each with a different center frequency. To test this idea, a single set of three gratings were designed that would maximize threshold. To simplify the optimization, all gratings were assumed to be the same length, the grating periods were constrained to be equally spaced ( $\Lambda - \Delta\Lambda, \Lambda, \text{ and } \Lambda + \Delta\Lambda$ ), and there is assumed to be no interaction between the gratings. The resulting transmission curve is shown in Figure 72(c) and the grating characteristics are

summarized in Table 8. This design increased SRS threshold by a factor of 47% to 52.1 W, while maintaining a relatively high transmission at 1.064 microns of 95%.

For completeness, another case was investigated with three sets of gratings in the fiber. Each set had three gratings with different periods for a total of nine gratings written into the fiber. The transmission curve and grating characteristics are shown in Figure 72(d) and Table 8 respectively. This design resulted in an increase of 104% in SRS threshold to 72.3 W.

### **8.3. Conclusions**

Based upon the theoretical results described above, a set of long period gratings could clearly increase SRS threshold significantly. However, there were many simplifications made to make the problem tractable. The expected effects of these simplifications are described below.

First, the pump beam was only assumed to pass through the fiber one time. Although this appropriately models a fiber amplifier, this is obviously not the case for a fiber laser where feedback is required. A laser may be affected by the grating in a remarkably different way. Depending on the cavity, the laser beam would bounce many times back and forth through the cavity, thus the transmission of the pump beam would become extremely important. It would be appropriate to increase the importance of its transmission in the figure of merit used to optimize the grating. Additionally, if there is any feedback of the Stokes beam by the cavity mirrors, SRS threshold would be remarkably affected.

It was also assumed that the index variation was perfectly sinusoidal over the grating length. This simplified the analysis, but any variations in the grating period or index depth will smear the transmission curve. Additionally, an intentional apodization of the index variation could eliminate coupling between the pump and lower order cladding modes [84], thus increase the transmission at 1.064 microns. This would also allow for efficient use of higher order cladding modes that have a stronger overlap with the LP<sub>01</sub> core-guided mode.

Along the same lines, a transmission band can be generated within a long period grating using a  $\pi$  phase shift in the center of the grating [86]. Thus by centering the transmission band at the pump wavelength, a high-order cladding mode with a broad spectral bandwidth could be used. Again, this could better match the Raman gain curve while maintaining the required high pump transmission.

Finally, the analysis performed here neglects the interaction between adjacent gratings and coupling from the core into multiple cladding modes. Since the calculation assumed that only the core-guided mode and a single cladding guided mode were coupled, an overlapping third mode would clearly change the results [12]. This is expected to affect the transmission near 200 cm<sup>-1</sup> where coupling into the HE<sub>11</sub> and the HE<sub>13</sub> modes nearly overlap, but there should not be a significant problem at the Raman gain peak unless successive gratings in a set are closely spaced. This problem would have to be characterized to fully appreciate its effect on the transmission curve.

## **9. Conclusions**

### **9.1. Technical achievements**

The goal of the research examined in this document was to generate high intensity laser beams in optical fibers. This problem was investigated from a variety of angles. In Chapter 4, the spatial characteristics of stimulated Brillouin scattering in a long multimode fiber were examined. It was clearly demonstrated in this chapter that long, multimode fibers generated a Gaussian-like Stokes beam even when the pump beam was highly aberrated. This feature of SBS was also examined theoretically. It was found that for many pump conditions, the finite Stokes shift due to SBS did not allow for phase conjugation in long fibers and resulted in a stronger gain for the  $LP_{01}$  fiber mode. On the other hand, the polarization states of the beam were preserved by Brillouin reflection. An elliptically polarized pump beam was found to reflect into an elliptically polarized Stokes beam with the same handedness, identical to the reflection properties of a phase conjugate mirror. These results were found to agree with a theoretical model that assumes orthogonal polarization states reflect off the same density grating in the fiber. Additionally, this chapter examined the characteristics of higher order modes excited in the fiber. It was found that under specific pumping conditions, an  $LP_{11}$  fiber mode could be excited. However, small perturbations to the gain, such as launching a second pump beam at the same frequency into the fiber, would result in the excitation of the  $LP_{01}$  mode. Finally, the chapter was concluded with an analysis of SBS beam cleanup in a ring cavity design. When there was strong coupling of the Stokes beam back into the

fiber, the beam quality suffered. On the other hand, a small seed was found to increase the Stokes output with a minimal affect on the beam quality.

Beam combining using stimulated Brillouin scattering was examined in Chapter 5. Since the fundamental fiber mode was excited regardless of the pumping conditions, two pump beams coupled into the fiber at different positions could be spatially combined. The effect was quantitatively analyzed using lasers at the same frequency that worked together to produce two temporally coherent Stokes beams as well as using two lasers at different frequencies that produced two temporally incoherent Stokes beams. In both cases, however, the Stokes beams were found to have nearly perfect spatial overlap. Coherent beam combining has the benefit of increased overall efficiency over that of incoherent beam combining. However, the frequency requirements on the two pump beams are very stringent, thus incoherent combining is a more practical solution to combining multiple lasers in many situations. During the course of this work, the efficiency was measured as a function of the coupling position and found to fall off as the beam was coupled into the fiber edges. Additionally, the polarization state of the Stokes beam was found to mimic that of the pump in the same manner as it did for single beam cleanup. Finally, the spatial coherence of the beams was demonstrated by the linear interference pattern generated when different portions of the Stokes beam overlapped on an observation screen.

In Chapter 6, the limitations to stimulated Brillouin scattering beam cleanup and combining were discussed along with several methods that could be used to overcome these limitations. Section 6.1 examined the requirements on an optical system designed

to combine more than two beams and efficiently collect the Stokes output into a usable beam. The ideas presented here showed that combining four sources would clearly be possible. It also demonstrated a path to incorporate more pump beams into the design.

The following section investigated the limitation that second order SBS would have on a beam combining or coherent beam cleanup system. Using a relatively small fiber, the Stokes output was monitored to find the second order threshold. This was then modeled, taking into account the forward propagating pump, backward propagating Stokes, the portion of the Stokes beam that reflects off the front fiber facet and propagates forward in the fiber, and the second order Stokes beam. These beams were coupled together through stimulated Brillouin scattering and four-wave mixing. Using this model, it was found that without four-wave mixing to seed second order SBS, the second order threshold would be much higher and would not be a significant limiting factor. This was verified to some extent experimentally by angle cleaving the front fiber facet, thus eliminating the forward propagating Stokes beam. In this experiment no second order SBS was observed at power levels much higher than the original second order threshold.

Finally, in Section 6.2, SRS was investigated as an alternative to SBS for beam cleanup applications. SRS has the benefit of an increased gain bandwidth, thus relaxing the spectral requirements on the pump. In this section, the beam quality of the Stokes power was investigated and found to be nearly nine times better than that of the transmitted pump beam. This has the potential of increasing the power on target by a factor of 74.

The remaining chapters shift from using the benefits of stimulated scattering to eliminating stimulated Raman scattering in optical systems for which SRS can be detrimental. In Chapter 7, the effect of an intercavity dopant is modeled in a fiber. The dopant, holmium, is found to have a strong absorption feature at the Raman gain peak for lasers centered at 1.094 microns. This wavelength is well within the gain curve of ytterbium doped fibers and SRS threshold could be increased by a factor of two with a relatively small amount of dopant, 0.012 molar percent. Even when pumped by a neodymium laser at 1.064 microns, the absorption of holmium is found to have a significant effect on the SRS threshold. The SRS threshold could be doubled with 0.053 molar percent of holmium. The effect of this dopant on the transmission at the pump wavelength was only qualitatively analyzed. However, it was expected to be relatively low.

Finally, in Chapter 8, SRS suppression using a long period grating was investigated. Although the results were not as dramatic as those using an intercavity dopant, the long period grating did provide a significant increase in SRS threshold. Using a series of nine gratings in a 100 m fiber, the SRS threshold was more than doubled. Additionally, relatively little effort would be required to apply this solution to lasers at different wavelengths.

## **9.2. Research impact**

The research described in this dissertation provides a tool that could be used in a variety of applications to increase the state of the art in laser brightness. Several of those applications are examined in the following discussion.

### *9.2.1. Laser Cleanup and Combining*

Diode lasers are extremely useful for their unmatched efficiency and compact design, but they are limited in output power and spatial quality. Current state of the art, high power diode lasers are capable of producing more than 8W [87], but the typical beam quality of diode lasers is on the order of 50 times diffraction limited [88]. Although individual devices have been designed with high quality output using novel cavity designs such as the tapered laser, z-laser, and alpha-DFB, these will do little to overcome the power limit imposed by facet damage. Arrays of these lasers can produce higher power than individual emitters, but unless the beams can be spatially combined and cleaned, the increased power does not result in a significant increase in overall intensity. Furthermore, heat dissipation remains a limitation to the power generated by diode arrays [88]. Physically separating the arrays and combining the overall diode laser power in a fiber using stimulated scattering can overcome this limitation, increasing the beam quality dramatically and increasing the overall power by an order of magnitude.

Although special consideration is required to force a diode laser to operate at a single frequency for use with an SBS beam combiner, narrow linewidth devices have been designed and could easily be combined [89, 90]. A portion of the research conducted in the initial stages of this dissertation was completed using a 500 mW alpha-DFB laser designed by SDL, Inc. Assuming careful optical engineering would result in optimal coupling of these diffraction limited devices into a long optical fiber (perhaps using two concentric pump rings in the arrangement shown in Figure 48), a total of 18 pump lasers could be combined producing a diffraction limited, spatially coherent diode laser source

with nearly the same output power as the highest reported diode laser. Yet this device would be far from the second order threshold, predicted to be more than 80 W.

Commercially available Diode bars, on the other hand, produce more than 50 W cw power and have been demonstrated in the lab to produce 270 W [88]. With linewidths on the order of 1 THz [91], using SBS to spatially combine the individual emitters is impractical. However, SRS beam combining is a feasible alternative for sources over the SRS threshold of nearly 100 W. As the power per bar becomes closer to the theoretical limit of 10 kW [88], the total efficiency of an SRS beam combiner becomes reasonable. If the diode laser bar had a beam quality on the order of 50 times the diffraction limit, Raman beam cleanup could increase beam brightness by a factor of about 2000.

In particular, these ideas could be applied to current military requirements. Specifically, an Air Force topic found in the Department of Defense small business innovation research program solicitation for 2002 seems well suited for SBS beam combining and cleanup. Topic AF02-006 describes a need for an efficient 0.9 micron laser for space-based lasers. The laser must produce 1-10 watts cw power and have a high spatial quality output. These characteristics are optimally suited for SBS beam combining using frequency stabilized GaAs or AlGaAs diode lasers.

For other DOD applications, high power may mean several kilowatts average power. The joint technology office has funded research by Boeing to investigate high power devices generated through SRS beam combining of high power Nd:YAG lasers [92]. This program was explored in part due to the initial results gathered and presented as a part of this dissertation research.

### *9.2.2. SRS Reduction*

The development of high power fiber lasers grew remarkably from 1997-1999. Over two years, the peak CW power reported in those devices rose by a factor of 3 [66]. This growth came to a halt partly due to the observation of SRS in the laser output. The application of an intercavity dopant or long period grating to the problem of stimulated scattering in fiber lasers removes or at least delays this limitation. At dopant levels of 0.3 molar%, more than an order of magnitude increase in SRS threshold is expected, allowing for an increase of the single mode fiber laser output from 110 W to 1.7 kW.

### Appendix A. Fiber Cladding Modes

The fiber cladding mode dispersion relation is critical in the design and characterization of long period gratings. Using the notation of Erdogan, the dispersion relation is shown below [12, 16].

$$\zeta_0 = \zeta_0' \quad (\text{A.1})$$

where

$$\zeta_0 = \frac{1}{\sigma_2} \frac{u_2 \left( JK + \frac{\sigma_1 \sigma_2 u_{21} u_{32}}{n_2^2 a_1 a_2} \right) p_l(a_2) - K q_l(a_2) + J r_l(a_2) - \frac{1}{u_2} s_l(a_2)}{-u_2 \left( \frac{u_{32}}{n_2^2 a_2} J - \frac{u_{21}}{n_1^2 a_1} K \right) p_l(a_2) + \frac{u_{32}}{n_1^2 a_2} q_l(a_2) + \frac{u_{21}}{n_1^2 a_1} r_l(a_2)} \quad (\text{A.2})$$

$$\zeta_0' = \sigma_1 \frac{u_2 \left( \frac{u_{32}}{a_2} J - \frac{n_3^2 u_{21}}{n_2^2 a_1} K \right) p_l(a_2) - \frac{u_{32}}{a_2} q_l(a_2) - \frac{u_{21}}{a_1} r_l(a_2)}{u_2 \left( \frac{n_3^2}{n_2^2} JK + \frac{\sigma_1 \sigma_2 u_{21} u_{32}}{n_1^2 a_1 a_2} \right) p_l(a_2) - \frac{n_3^2}{n_1^2} K q_l(a_2) + J r_l(a_2) - \frac{n_2^2}{n_1^2 u_2} s_l(a_2)} \quad (\text{A.3})$$

$$\begin{aligned} \sigma_1 &= il n_{eff} / Z_0 \\ \sigma_2 &= il n_{eff} Z_0 \\ u_{21} &= \frac{1}{u_2^2} - \frac{1}{u_1^2} \\ u_{32} &= \frac{1}{w_3^2} + \frac{1}{u_2^2} \end{aligned} \quad (\text{A.4})$$

$$\begin{aligned}
Z_0 &= \sqrt{\frac{\mu_0}{\epsilon_0}} \\
u_j^2 &= \left(2\pi/\lambda\right)^2 \left(n_j^2 - n_{eff}^2\right) \quad [j \in (1, 2)] \\
w_3^2 &= \left(2\pi/\lambda\right)^2 \left(n_{eff}^2 - n_3^2\right)
\end{aligned} \tag{A.5}$$

$$\begin{aligned}
J &= \frac{J_l'(u_1 a_1)}{u_1 J_l(u_1 a_1)} \\
K &= \frac{K_l'(w_3 a_2)}{w_3 K_l(w_3 a_2)}
\end{aligned} \tag{A.6}$$

$$\begin{aligned}
p_l(r) &= J_l(u_2 r) N_l(u_2 a_1) - J_l(u_2 a_1) N_l(u_2 r) \\
q_l(r) &= J_l(u_2 r) N_l'(u_2 a_1) - J_l'(u_2 a_1) N_l(u_2 r) \\
r_l(r) &= J_l'(u_2 r) N_l(u_2 a_1) - J_l(u_2 a_1) N_l'(u_2 r) \\
s_l(r) &= J_l'(u_2 r) N_l'(u_2 a_1) - J_l'(u_2 a_1) N_l'(u_2 r)
\end{aligned} \tag{A.7}$$

where  $a_1$  is the radius of the fiber core and  $a_2$  is the radius of the fiber cladding,  $n_{eff}$  is the effective index of the cladding mode, and  $\lambda$  is the wavelength.  $n_1$ ,  $n_2$ , and  $n_3$  are the indices of refraction for the core, cladding, and jacket respectively, and  $J_l$ ,  $K_l$ , and  $N_l$  are the Bessel function, modified Bessel function, and Neumann functions respectively.

Once  $\zeta_0$  is determined from the dispersion relation, the field distributions can be calculated. Since the rest of this document is only concerned with the  $l = 1$  cladding modes, these are the only modes explicitly shown here. In the fiber core, the  $r$  component of the electric field is

$$E_r^{cl}(r, \phi, z) = i E_{1\nu}^{cl} \frac{u_1}{2} \left\{ J_2(u_1 r) + J_0(u_1 r) - \frac{\sigma_2 \zeta_0}{n_1^2} [J_2(u_1 r) - J_0(u_1 r)] \right\} \cdot \exp(i\phi) \exp[i(\beta z - \omega t)] \quad (\text{A.8})$$

The  $\phi$ -component of the electric field is

$$E_\phi^{cl}(r, \phi, z) = E_{1\nu}^{cl} \frac{u_1}{2} \left\{ J_2(u_1 r) - J_0(u_1 r) - \frac{\sigma_2 \zeta_0}{n_1^2} [J_2(u_1 r) + J_0(u_1 r)] \right\} \cdot \exp(i\phi) \exp[i(\beta z - \omega t)] \quad (\text{A.9})$$

And the  $z$ -component of the electric field is

$$E_z^{cl}(r, \phi, z) = E_{1\nu}^{cl} \frac{u_1^2 \sigma_2 \zeta_0}{n_1^2 \beta} J_1(u_1 r) \exp(i\phi) \exp[i(\beta z - \omega t)]. \quad (\text{A.10})$$

where  $\beta$  is the propagation constant of the mode and  $E_{1\nu}^{cl}$  is the amplitude of the field in that mode. The  $r$ -component of the magnetic field is

$$H_r^{cl}(r, \phi, z) = E_{1\nu}^{cl} \frac{u_1}{2} \left\{ i\sigma_1 [J_2(u_1 r) - J_0(u_1 r)] + i\zeta_0 [J_2(u_1 r) + J_0(u_1 r)] \right\} \cdot \exp(i\phi) \exp[i(\beta z - \omega t)] \quad (\text{A.11})$$

The  $\phi$ -component of the magnetic field is

$$H_\phi^{cl}(r, \phi, z) = -i E_{1\nu}^{cl} \frac{u_1}{2} \left\{ i\sigma_1 [J_2(u_1 r) + J_0(u_1 r)] + i\zeta_0 [J_2(u_1 r) - J_0(u_1 r)] \right\} \cdot \exp(i\phi) \exp[i(\beta z - \omega t)] \quad (\text{A.12})$$

And the  $z$ -component of the magnetic field is

$$H_z^{cl}(r, \phi, z) = -i E_{1\nu}^{cl} \frac{u_1^2 i\sigma_1}{\beta} J_1(u_1 r) \exp(i\phi) \exp[i(\beta z - \omega t)]. \quad (\text{A.13})$$

The fields in the cladding region are

$$E_r^{cl}(r, \phi, z) = i E_{1\nu}^{cl} \frac{\pi a_1 u_1^2 J_1(u_1 a_1)}{2} \left\{ -\frac{F_2}{r} p_1(r) + \frac{1}{u_2 r} q_1(r) - \frac{\sigma_2}{n_2^2} \left[ u_2 G_2 r_1(r) - \frac{n_2^2 \zeta_0}{n_1^2} s_1(r) \right] \right\} \exp[i\phi + i(\beta z - \omega t)] \quad (A.14)$$

$$E_\phi^{cl}(r, \phi, z) = E_{1\nu}^{cl} \frac{\pi a_1 u_1^2 J_1(u_1 a_1)}{2} \left\{ \frac{\sigma_2}{n_2^2} \left[ \frac{G_2}{r} p_1(r) - \frac{n_2^2 \zeta_0}{n_1^2 u_2 r} q_1(r) \right] + u_2 F_2 r_1(r) - s_1(r) \right\} \exp[i\phi + i(\beta z - \omega t)] \quad (A.15)$$

$$E_z^{cl}(r, \phi, z) = -E_{1\nu}^{cl} \frac{\pi a_1 u_1^2 u_2^2 \sigma_2 J_1(u_1 a_1)}{2 n_2^2 \beta} \left[ G_2 p_1(r) - \frac{n_2^2 \zeta_0}{n_1^2 u_2} q_1(r) \right] \exp[i\phi + i(\beta z - \omega t)] \quad (A.16)$$

$$H_r^{cl}(r, \phi, z) = E_{1\nu}^{cl} \frac{\pi a_1 u_1^2 J_1(u_1 a_1)}{2} \left\{ -i \frac{G_2}{r} p_1(r) + i \frac{n_2^2 \zeta_0}{n_1^2 u_2 r} q_1(r) + -i \sigma_1 \left[ u_2 F_2 r_1(r) - s_1(r) \right] \right\} \exp[i\phi + i(\beta z - \omega t)] \quad (A.17)$$

$$H_z^{cl}(r, \phi, z) = -i E_{1\nu}^{cl} \frac{\pi a_1 u_1^2 u_2^2 i \sigma_1 J_1(u_1 a_1)}{2 \beta} \left[ F_2 p_1(r) - \frac{1}{u_2} q_1(r) \right] \exp[i\phi + i(\beta z - \omega t)] \quad (A.18)$$

where

$$F_2 = J - \frac{u_{21} \sigma_2 \zeta_0}{n_1^2 a_1} \quad (A.19)$$

$$G_2 = \zeta_0 J + \frac{u_{21} \sigma_1}{a_1}$$

Finally, the fields in the jacket are

$$E_r^{cl}(r, \phi, z) = i E_{1\nu}^{cl} \frac{\pi a_1 u_1^2 u_2^2 J_1(u_1 a_1)}{4\omega_3 K_1(\omega_3 a_2)} \left\{ -F_3 [K_2(\omega_3 r) - K_0(\omega_3 r)] + \right. \\ \left. \frac{\sigma_2 G_3}{n_3^2} [K_2(\omega_3 r) + K_0(\omega_3 r)] \right\} \exp[i\phi + i(\beta z - \omega t)] \quad (A.20)$$

$$E_\phi^{cl}(r, \phi, z) = E_{1\nu}^{cl} \frac{\pi a_1 u_1^2 u_2^2 J_1(u_1 a_1)}{4\omega_3 K_1(\omega_3 a_2)} \left\{ -F_3 [K_2(\omega_3 r) + K_0(\omega_3 r)] + \right. \\ \left. \frac{\sigma_2 G_3}{n_3^2} [K_2(\omega_3 r) - K_0(\omega_3 r)] \right\} \exp[i\phi + i(\beta z - \omega t)] \quad (A.21)$$

$$E_z^{cl}(r, \phi, z) = E_{1\nu}^{cl} \frac{\pi a_1 u_1^2 u_2^2 \sigma_2 J_1(u_1 a_1)}{2n_3^2 \beta K_1(\omega_3 a_2)} G_3 K_1(\omega_3 r) \exp[i\phi + i(\beta z - \omega t)] \quad (A.22)$$

$$H_r^{cl}(r, \phi, z) = E_{1\nu}^{cl} \frac{\pi a_1 u_1^2 u_2^2 J_1(u_1 a_1)}{4\omega_3 K_1(\omega_3 a_2)} \left\{ -i\sigma_1 F_3 [K_2(\omega_3 r) + K_0(\omega_3 r)] - \right. \\ \left. iG_3 [K_2(\omega_3 r) - K_0(\omega_3 r)] \right\} \exp[i\phi + i(\beta z - \omega t)] \quad (A.23)$$

$$H_\phi^{cl}(r, \phi, z) = i E_{1\nu}^{cl} \frac{\pi a_1 u_1^2 u_2^2 J_1(u_1 a_1)}{4\omega_3 K_1(\omega_3 a_2)} \left\{ i\sigma_1 F_3 [K_2(\omega_3 r) - K_0(\omega_3 r)] - \right. \\ \left. G_3 [K_2(\omega_3 r) + K_0(\omega_3 r)] \right\} \exp[i\phi + i(\beta z - \omega t)] \quad (A.24)$$

$$H_z^{cl}(r, \phi, z) = i E_{1\nu}^{cl} \frac{\pi a_1 u_1^2 u_2^2 i\sigma_1 J_1(u_1 a_1)}{2\beta K_1(\omega_3 a_2)} F_3 K_1(\omega_3 r) \exp[i\phi + i(\beta z - \omega t)] \quad (A.25)$$

where

$$F_3 = -F_2 p_1(a_2) + \frac{1}{u_2} q_1(a_2) \\ G_3 = -\frac{n_3^2}{n_2^2} \left[ G_2 p_1(a_2) - \frac{n_2^2 \zeta_0}{n_1^2 u_2} q_1(a_2) \right]. \quad (A.26)$$

From these field distributions, the intensity pattern of the modes can be calculated

$$I_z(r) = \frac{1}{2} \operatorname{Re} \left( \vec{E} \times \vec{H}^* \right). \quad (\text{A.27})$$

## Appendix B. Local Effective Brillouin Gain

Section 4.2 uses the effective Brillouin gain to explain the origin of beam cleanup.

This appendix fills in the steps between the definition of the effective gain,

Equation (4.3), and Equation (4.4). The effective Brillouin gain in a fiber is repeated here.

$$g_{B_{eff}}(z) = g_B \frac{\int I_s(r_\perp, z) I_p(r_\perp, z) \partial r_\perp}{P_s(z) P_p(z)}. \quad (\text{B.1})$$

The pump and Stokes electric fields can be expanded in terms of the optical fiber modes described in Chapter 2.

$$\begin{aligned} I(r_\perp, z) &= 2\epsilon_0 cn \frac{\omega}{2\pi} \int_0^{2\pi/\omega} |E(r_\perp, z, t)|^2 dt \\ &= 4\epsilon_0 cn \sum_{m,q} \left\{ \psi_m(r_\perp) \psi_q(r_\perp) A_m(z) A_q(z) \exp \left[ i((k_{cm} - k_{cq})z + (\phi_m - \phi_q)) \right] \right\} \end{aligned} \quad (\text{B.2})$$

where the summations are over all fiber modes and the  $m^{\text{th}}$  mode has a transverse distribution,  $\psi_m(r_\perp)$ , an amplitude,  $A_m(z)$ , a propagation constant,  $k_{cm}$ , and a phase,  $\phi_m$ . After labeling each of these terms p or s for the pump or Stokes beam, this representation for the intensity can be substituted into Equation (B.1)

$$\begin{aligned} g_{B_{eff}}(z) &= \frac{g_B 16(\epsilon_0 cn)^2}{P_s(z) P_p(z)} \sum_{m,q,p,v} A_{sm,sq,pj,pv}(z) \gamma_{sm,sq,pj,pv} \bullet \\ &\quad \exp \left[ i((\Delta k_{smq} + \Delta k_{pjv})z + (\Delta \phi_{smq} + \Delta \phi_{pjv})) \right] \end{aligned} \quad (\text{B.3})$$

The variables in Equation (B.3) are defined by

$$\begin{aligned}
\gamma_{sm,sq,pj,pv} &= \int \{\psi_{sm}(r_\perp) \psi_{sq}(r_\perp) \psi_{pj}(r_\perp) \psi_{pv}(r_\perp)\} dr_\perp \\
A_{sm,sq,pj,pv}(z) &= A_{sm}(z) A_{sq}(z) A_{pj}(z) A_{pv}(z) \\
\Delta k_{pjv} &= k_{pcj} - k_{pcv} \\
\Delta k_{smq} &= k_{scm} - k_{scq} \\
\Delta \phi_{pjv} &= \phi_{pcj} - \phi_{pcv} \\
\Delta \phi_{smq} &= \phi_{scm} - \phi_{scq}
\end{aligned} \tag{B.4}$$

It is useful to expand the summations in Equation (B.3) as follows.

$$\sum_{m,q,j,v} \rightarrow \sum_{m,q < m,j,v < j} + \sum_{m,q = m,j,v < j} + \sum_{m,q > m,j,v < j} + \sum_{m,q < m,j,v = j} + \\
\sum_{m,q = m,j,v = j} + \sum_{m,q > m,j,v = j} + \sum_{m,q < m,j,v > j} + \sum_{m,q = m,j,v > j} + \sum_{m,q > m,j,v > j} \tag{B.5}$$

When  $v = j$  ( $q = m$ ),  $\Delta k_{pjv} = 0$  ( $\Delta k_{smq} = 0$ ) and  $\Delta \phi_{pjv} = 0$  ( $\Delta \phi_{smq} = 0$ ), which leads to

$$\begin{aligned}
g_{Beff}(z) &= \frac{g_B 16 (\varepsilon_0 c n)^2}{P_s(z) P_p(z)} \left\{ \sum_{m,q=m,j,v=j} A_{sm,sq,pj,pv}(z) \gamma_{sm,sq,pj,pv} + \right. \\
&\quad \sum_{m,q < m,j,v < j} A_{sm,sq,pj,pv}(z) \gamma_{sm,sq,pj,pv} \exp \left[ i \left( (\Delta k_{smq} + \Delta k_{pjv}) z + (\Delta \phi_{smq} + \Delta \phi_{pjv}) \right) \right] + \\
&\quad \sum_{m,q = m,j,v < j} A_{sm,sq,pj,pv}(z) \gamma_{sm,sq,pj,pv} \exp \left[ i (\Delta k_{pjv} z + \Delta \phi_{pjv}) \right] + \\
&\quad \sum_{m,q > m,j,v < j} A_{sm,sq,pj,pv}(z) \gamma_{sm,sq,pj,pv} \exp \left[ i \left( (\Delta k_{smq} + \Delta k_{pjv}) z + (\Delta \phi_{smq} + \Delta \phi_{pjv}) \right) \right] + \\
&\quad \sum_{m,q < m,j,v = j} A_{sm,sq,pj,pv}(z) \gamma_{sm,sq,pj,pv} \exp \left[ i (\Delta k_{smq} z + \Delta \phi_{smq}) \right] + \\
&\quad \sum_{m,q > m,j,v = j} A_{sm,sq,pj,pv}(z) \gamma_{sm,sq,pj,pv} \exp \left[ i (\Delta k_{smq} z + \Delta \phi_{smq}) \right] + \\
&\quad \sum_{m,q < m,j,v > j} A_{sm,sq,pj,pv}(z) \gamma_{sm,sq,pj,pv} \exp \left[ i \left( (\Delta k_{smq} + \Delta k_{pjv}) z + (\Delta \phi_{smq} + \Delta \phi_{pjv}) \right) \right] + \\
&\quad \sum_{m,q = m,j,v > j} A_{sm,sq,pj,pv}(z) \gamma_{sm,sq,pj,pv} \exp \left[ i (\Delta k_{pjv} z + \Delta \phi_{pjv}) \right] + \\
&\quad \left. \sum_{m,q > m,j,v > j} A_{sm,sq,pj,pv}(z) \gamma_{sm,sq,pj,pv} \exp \left[ i \left( (\Delta k_{smq} + \Delta k_{pjv}) z + (\Delta \phi_{smq} + \Delta \phi_{pjv}) \right) \right] \right\} \tag{B.6}
\end{aligned}$$

Two of the nine summation terms in Equation (B.6) are shown below.

$$\begin{aligned} & \sum_{m,q < m,j,v=j} A_{sm,sq,pj,pv}(z) \gamma_{sm,sq,pj,pv} \exp[i(\Delta k_{smq} z + \Delta \phi_{smq})] + \\ & \sum_{m,q > m,j,v=j} A_{sm,sq,pj,pv}(z) \gamma_{sm,sq,pj,pv} \exp[i(\Delta k_{smq} z + \Delta \phi_{smq})] \end{aligned} \quad (\text{B.7})$$

These terms can be rewritten using the identity  $\sum_{m,q > m,j,v=j} = \sum_{q,m < q,j,v=j}$  and relabeling the

dummy indices of the second summation using the following rules:  $q \rightarrow m$  and  $m \rightarrow q$ .

$$\begin{aligned} & \sum_{m,q < m,j,v=j} A_{sm,sq,pj,pv}(z) \gamma_{sm,sq,pj,pv} \exp[i(\Delta k_{smq} z + \Delta \phi_{smq})] + \\ & \sum_{m,q < m,j,v=j} A_{sq,sm,pj,pv}(z) \gamma_{sq,sm,pj,pv} \exp[i(\Delta k_{sqm} z + \Delta \phi_{sqm})] \end{aligned} \quad (\text{B.8})$$

$A_{sm,sq,pj,pv}(z)$  and  $\gamma_{sm,sq,pj,pv}$  are invariant when the indices  $q$  and  $m$  are interchanged.

$\Delta k_{smq}$  and  $\Delta \phi_{smq}$ , on the other hand, are antisymmetric and change sign when  $q$  and  $m$

are interchanged. Therefore, Equation (B.8) can be simplified as follows

$$\sum_{m,q < m,j,v=j} 2A_{sm,sq,pj,pv}(z) \gamma_{sm,sq,pj,pv} \cos(\Delta k_{smq} z + \Delta \phi_{smq}). \quad (\text{B.9})$$

Applying these same steps to other pairs of sums in Equation (B.6) results in

$$\begin{aligned} g_{Beff}(z) = & \frac{g_B 16(\varepsilon_0 c n)^2}{P_s(z) P_p(z)} \left\{ \sum_{m,q=m,j,v=j} A_{sm,sq,pj,pv}(z) \gamma_{sm,sq,pj,pv} + \right. \\ & \sum_{m,q=m,j,v < j} 2A_{sm,sq,pj,pv}(z) \gamma_{sm,sq,pj,pv} \cos(\Delta k_{pjv} z + \Delta \phi_{pjv}) + \\ & \sum_{m,q < m,j,v=j} 2A_{sm,sq,pj,pv}(z) \gamma_{sm,sq,pj,pv} \cos(\Delta k_{smq} z + \Delta \phi_{smq}) + \\ & \sum_{m,q < m,j,v < j} 2A_{sm,sq,pj,pv}(z) \gamma_{sm,sq,pj,pv} \cos[(\Delta k_{smq} + \Delta k_{pjv})z + (\Delta \phi_{smq} + \Delta \phi_{pjv})] + \\ & \left. \sum_{m,q < m,j,v < j} 2A_{sm,sq,pj,pv}(z) \gamma_{sm,sq,pj,pv} \cos[(\Delta k_{smq} - \Delta k_{pjv})z + (\Delta \phi_{smq} - \Delta \phi_{pjv})] \right\} \end{aligned} \quad (\text{B.10})$$

This is the form of the effective Brillouin gain used in Equation (4.4).

## Bibliography

- [1] S. Gourley, "Making Light Legal," *Jane's Defence Weekly*, vol. 33, pp. 22-26, 2000.
- [2] H. J. Eichler, A. Haase, and O. Mehl, "High Power Solid State Lasers with Phase Conjugation for Applications with High Beam Quality," in *High Power Lasers - Science and Engineering*, vol. 7, *High Technology*, R. Kossowsky, M. Jelinek, and R. F. Walter, Eds. Boston: Kluwer Academic Publishers, 1996, pp. 241-253.
- [3] G. P. Agrawal, *Nonlinear Fiber Optics*, 3 ed. San Diego: Academic Press, Inc., 2001.
- [4] N. G. Basov, et al., "Inversion of wavefront in SMBS of a depolarized pump," *JETP Letters*, vol. 28, pp. 197-201, 1979.
- [5] D. A. Rockwell and C. R. Giuliano, "Coherent coupling of laser gain media using phase conjugation," *Opt. Lett.*, vol. 11, pp. 147-149, 1986.
- [6] M. Valley, G. Lombardi, and R. Aprahamian, "Beam combination by stimulated Brillouin scattering," *J. Opt. Soc. Am. B*, vol. 3, pp. 1492-1497, 1986.
- [7] R. H. Moyer, M. Valley, and M. C. Cimolino, "Beam combination through stimulated Brillouin scattering," *J. Opt. Soc. Am. B*, vol. 5, pp. 2473-2489, 1988.
- [8] H. J. Kong, Y. S. Shin, and H. Kim, "Beam combination characteristics in an array laser using stimulated Brillouin scattering phase conjugate mirrors considering partial coherency between the beams," *Fusion Engineering and Design*, vol. 44, pp. 407-417, 1999.
- [9] B. C. Rodgers, T. H. Russell, and W. B. Roh, "Laser beam combining and cleanup by stimulated Brillouin scattering in a multimode optical fiber," *Opt. Lett.*, vol. 24, pp. 1124-1126, 1999.
- [10] G. Mitchard and R. Waarts, "Double-clad fibers enable lasers to handle high power," *Laser Focus World*, vol. 35, pp. 113-115, 1999.
- [11] M. J. F. Digonnet, *Rare Earth Doped Fiber Lasers and Amplifiers*. New York: Marcel Dekker, Inc., 1993.
- [12] T. Erdogan, "Cladding-mode resonances in short- and long-period fiber grating filters," *J. Opt. Soc. Am. A*, vol. 14, pp. 1760-1773, 1997.

- [13] B. E. A. Saleh and M. C. Teich, *Fundamentals of Photonics*. New York: John Wiley & Sons, Inc., 1991.
- [14] D. R. Lide, *CRC Handbook of Chemistry and Physics*, 72 ed. Boston: CRC Press, 1991.
- [15] A. Yariv, *Optical Electronics*, Fourth ed. Philadelphia: Saunders College Publishing, 1991.
- [16] T. Erdogan, “Cladding-mode resonances in short- and long-period fiber grating filters: errata,” *J. Opt. Soc. Am. A*, vol. 17, pp. 2113, 2000.
- [17] P. N. Butcher and D. Cotter, *The Elements of Nonlinear Optics*. United Kingdom: Cambridge University Press, 1990.
- [18] R. G. Smith, “Optical Power Handling Capacity of Low Loss Optical Fibers as Determined by Stimulated Raman and Brillouin Scattering,” *Appl. Opt.*, vol. 11, pp. 2489-2494, 1972.
- [19] R. H. Stolen, C. Lee, and R. K. Jain, “Development of the stimulated Raman spectrum in single-mode silica fibers,” *J. Opt. Soc. Am. B*, vol. 1, pp. 652-657, 1984.
- [20] E. P. Ippen and R. H. Stolen, “Stimulated Brillouin scattering in optical fibers,” *Appl. Phys. Ltrs.*, vol. 21, pp. 539-540, 1972.
- [21] H. J. Eichler, B. Liu, M. Duelk, Z. Lu, and J. Chen, “Phase conjugation behind an ordered multimode fibre bundle,” *Opt. Commun.*, vol. 123, pp. 412-422, 1996.
- [22] Z. V. Nesterova, I. V. Aleksandrov, A. A. Polnitskii, and D. K. Sattarov, “Propagation characteristics of high power ultrashort light pulses in multimode optical fibers,” *JETP Letters*, vol. 34, pp. 371-374, 1982.
- [23] P. L. Baldeck, F. Raccah, and R. R. Alfano, “Observation of self-focusing in optical fibers with picosecond pulses,” *Opt. Lett.*, vol. 12, pp. 588-589, 1987.
- [24] A. B. Grudinin, E. M. Dianov, D. V. Korbkin, A. M. Prokhorov, and D. V. Khaidarov, “Nonlinear mode coupling in multimode optical fibers; excitation of femtosecond-range stimulated-Raman-scattering solitons,” *JETP Letters*, vol. 47, pp. 356-359, 1988.
- [25] K. S. Chiang, “Stimulated Raman scattering in a multimode optical fiber: evolution of modes in Stokes waves,” *Opt. Lett.*, vol. 17, pp. 352-354, 1992.
- [26] H. Bruesselbach, “Beam cleanup using stimulated Brillouin scattering in multimode fibers,” in *Conference on Lasers and Electro-Optics, Proc. Optical Society of America*, vol. 11, pp. 425-426, 1993.

- [27] B. C. Rodgers, "Laser Beam Combination and Cleanup via Stimulate Brillouin Scattering in Multi-Mode Optical Fibers," Master Thesis, Department of Engineering Physics, Air University, AFIT, Wright-Patterson AFB, 1999.
- [28] E. A. Kuzin, M. P. Petrov, and A. A. Fotiadi, "Phase Conjugation by SMBS in Optical Fibers," in *Optical Phase Conjugation*, M. Gower and D. Proch, Eds. Berlin: Springer-Verlag, 1994, pp. 74-96.
- [29] H. J. Eichler, J. Kunde, and B. Liu, "Quartz fibre phase conjugators with high fidelity and reflectivity," *Opt. Commun.*, vol. 139, pp. 327-334, 1997.
- [30] A. Heuer and R. Menzel, "Phase-conjugating stimulated Brillouin scattering mirror for low powers and reflectivities above 90% in an internally tapered optical fiber," *Opt. Lett.*, vol. 23, pp. 834-836, 1998.
- [31] D. Gloge, "Optical Power Flow in Multimode Fibers," *Bell System Technical Journal*, vol. 51, pp. 1767-1783, 1972.
- [32] W. A. Gambling, D. N. Payne, and H. Matsumura, "Mode Excitation in a Multimode Optical-Fiber Waveguide," *Elec. Letters*, vol. 9, pp. 412-414, 1973.
- [33] J. N. Kutz, J. A. Cox, and D. Smith, "Mode Mixing and Power Diffusion in Multimode Optical Fibers," *J. Lightwave Technol.*, vol. 16, pp. 1195-1202, 1998.
- [34] K. Nagano and S. Kawakami, "Measurements of mode conversion coefficients in graded-index fibers," *Appl. Opt.*, vol. 19, pp. 2426-2434, 1980.
- [35] G. Yabre, "Comprehensive Theory of Dispersion in Graded-Index Optical Fibers," *J. Lightwave Technol.*, vol. 18, pp. 166-177, 2000.
- [36] S. Shaklan, "Measurement of intermodal coupling in weakly multimode fiber optics," *Elec. Letters*, vol. 26, pp. 2022-2024, 1990.
- [37] D. Gloge, A. R. Tynes, M. A. Duguay, and J. W. Hansen, "Picosecond Pulse Distortion in Optical Fibers," *IEEE J. Quant. Elect.*, vol. QE-8, pp. 217-221, 1972.
- [38] R. Olshansky and D. A. Nolan, "Mode-dependent attenuation of optical fibers: excess loss," *Appl. Opt.*, vol. 15, pp. 1045-1047, 1976.
- [39] B. Y. Zel'dovich, N. F. Pilipetsky, and V. V. Shkunov, *Principles of Phase Conjugation*, vol. 42. Berlin: Springer-Verlag, 1985.
- [40] C. L. Tang, "Saturation and spectral characteristics of the Stokes emission in the stimulated Brillouin process," *J. Appl. Phys.*, vol. 37, pp. 2945-2955, 1966.

- [41] J. Hecht, "PMD threatens fiberoptic transmission speeds," *Laser Focus World*, pp. 129,130,132, December, 2000.
- [42] B. J. Choi, "Investigation of Laser Beam Combining and Clean-Up Via Seeded Stimulated Brillouin Scattering in Multimode Optical Fibers," Master Thesis, Department of Engineering Physics, Air University, AFIT, Wright-Patterson AFB, 2000.
- [43] S. Shaklan, "Selective mode injection and observation for few-mode fiber optics," *Appl. Opt.*, vol. 30, pp. 4379-4383, 1991.
- [44] G. G. Kochemasov and V. D. Nikolaev, "Investigation of the spatial characterisitcs of Stokes radiation in stimulated scattering under saturation conditions," *Sov. J. Quantum Electron.*, vol. 9, pp. 1155-1157, 1979.
- [45] Y. Aoki and K. Tajima, "Stimulated Brillouin scattering in a long single-mode fiber excited with a multimode pump laser," *J. Opt. Soc. Am. B*, vol. 5, pp. 358-363, 1988.
- [46] E. Hecht, *Optics*, 2nd ed. Massachusetts: Addison-Wesley, 1987.
- [47] E. Lichtman, A. A. Friesem, R. G. Waarts, and H. H. Yaffe, "Stimulated Brillouin scattering excited by two pump waves in single-mode fibers," *J. Opt. Soc. Am. B*, vol. 4, pp. 1397-1403, 1987.
- [48] P. Narum, M. D. Skeldon, and R. W. Boyd, "Effect of Laser Mode Structure on Stimulated Brillouin Scattering," *IEEE J. Quant. Elect.*, vol. QE-22, pp. 2161-2167, 1986.
- [49] B. Y. Zel'dovich, N. F. Pilipetskil, and V. V. Shkunov, "Phase conjugation in stimulated scattering," *Soviet Physics Usp.*, vol. 25, pp. 713-736, 1982.
- [50] C. R. Pollock, *Fundamentals of Optoelectronics*. Chicago, IL: Irwin, 1995.
- [51] A. E. Siegman, "New developments in laser resonators," in *Optical Resonators, Proc. SPIE*, vol. 1224, pp. 2-14, 1990.
- [52] J. Verdeyen, T., *Laser Electronics*, 3 ed. Englewood Cliffs: Prentice Hall, 1995.
- [53] D. P. Holcomb, "Multimode Fiber Coupling and Brightness Conservation," in *Solid State and Diode Laser Technology Review, Proc. Directed Energy Professional Society*, pp. FL-4, 2001.
- [54] E. A. Kuzin, M. P. Petrov, and A. A. Fotiadi, "Fiber-optic stimulated-Brillouin-scattering amplifier," *Soviet Physics Technical Physics*, vol. 33, pp. 206-209, 1988.

- [55] M. O. van Deventer, "Polarization Properties of Stimulated Brillouin Scattering in Single-Mode Fibers," *J. Lightwave Technol.*, vol. 12, pp. 585-590, 1994.
- [56] S. J. Garth and R. A. Sammut, "Theory of stimulated Raman scattering in two-mode optical fibers," *J. Opt. Soc. Am. B*, vol. 10, pp. 2040-2047, 1993.
- [57] G. Cook and K. D. Ridley, "Investigation of the bandwidth dependent characteristics of stimulated Brillouin scattering using a modeless dye laser," *Opt. Commun.*, vol. 130, pp. 192-204, 1996.
- [58] M. A. O'Key and M. R. Osborne, "Broadband stimulated Brillouin scattering," *Opt. Commun.*, vol. 89, pp. 269-275, 1992.
- [59] N. R. Islam and K. Sakuda, "Wave-front reconstruction by backward-stimulated Raman scattering in a multimode graded-index optical fiber," *J. Opt. Soc. Am. B*, vol. 14, pp. 3238-3241, 1997.
- [60] B. Y. Zel'dovich and V. V. Shkunov, "Wavefront reproduction in stimulated Raman scattering," *Sov. J. Quantum Electron.*, vol. 7, pp. 610-615, 1977.
- [61] J. T. Murray, R. C. Powel, and N. Peyghambarian, "Properties of stimulated Raman scattering in crystals," *Journal of Luminescence*, vol. 66, pp. 89-93, 1996.
- [62] J. T. Murray, W. L. Austin, and R. C. Powel, "Intracavity Raman conversion and Raman beam cleanup," *Optical Materials*, vol. 11, pp. 353-371, 1999.
- [63] N. F. Andreev, V. I. Bespalov, A. M. Kiselev, and G. A. Pasmanik, "Experimental investigation of the spatial structure of the first Stokes component of stimulated Raman scattering," *Sov. J. Quantum Electron.*, vol. 9, pp. 585, 1979.
- [64] J. C. van den Heuvel, "Numerical study of beam cleanup by stimulated Raman scattering," *J. Opt. Soc. Am. B*, vol. 12, pp. 650-657, 1995.
- [65] D. Richardson, J. Minelly, and D. Hanna, "Fiber laser systems shine brightly," *Laser Focus World*, pp. 87-96, September, 1997.
- [66] V. Dominic, et al., "110W fibre laser," *Elec. Letters*, vol. 35, pp. 1158-1160, 1999.
- [67] R. Lang, "Diode pumped fiber lasers and amplifiers," in *1999 Diode Laser Technology Review*, vol. 12, 1999.
- [68] V. Gapontsev, V. Fomin, A. Ount, and I. Samartsev, "100kW Ytterbium Fiber Laser," in *SPIE Conference on Solid State Lasers VIII, Proc. SPIE*, vol. 3613, pp. 49-54, 1999.

- [69] T. Sylvestre, H. Mailotte, and E. Lantz, “Stimulated Raman suppression under dual-frequency pumping in singlemode fibres,” *Elec. Letters*, vol. 34, pp. 141-142, 1998.
- [70] T. Sylvestre, H. Mailotte, P. T. Dinda, and E. Coquet, “Suppression of stimulated Raman scattering in optical fibres by power-controlled multifrequency pumping,” *Opt. Commun.*, vol. 159, pp. 32-36, 1999.
- [71] E. A. Kuzin, et al., “Simulated Raman scattering in a fiber with bending loss,” *Opt. Commun.*, vol. 169, pp. 87-91, 1999.
- [72] M. P. Petrov, E. A. Kuzin, M. A. Maksyutenko, and V. V. Spirin, “Stimulated Raman scattering in an optical fiber with strong wavelength-dependent losses,” *Sov. J. Quantum Electron.*, vol. 20, pp. 1107-1109, 1990.
- [73] Y. Urata, S. Wada, H. Tashiro, and T. Fukuda, “Doping of an absorbent into a Raman crystal for suppression of higher-order Stokes generation,” *Opt. Lett.*, vol. 25, pp. 752-754, 2000.
- [74] R. Paschotta, J. Nilsson, A. C. Tropper, and D. C. Hanna, “Ytterbium-Doped Fiber Amplifiers,” *IEEE J. Quant. Elect.*, vol. 33, pp. 1049-1056, 1997.
- [75] P. W. France, *Fluoride Glass Optical Fibres*. Boca Raton, FL: CRC Press, 1990.
- [76] J. Qiu, M. Shojiya, and Y. Kawamoto, “Sensitized  $\text{Ho}^{3+}$  up-conversion luminescence in  $\text{Nd}^{3+}$ - $\text{Yb}^{3+}$ - $\text{Ho}^{3+}$  co-doped  $\text{ZrF}_4$ -based glass,” *J. Appl. Phys.*, vol. 86, pp. 909-913, 1999.
- [77] X. X. Zhang, M. Bass, and B. H. T. Chai, “Spectroscopy of Yb, Ho codoped  $\text{KYF}_4$  and its application as up-conversion green laser,” in *Growth, Characterization, and Applications of Laser Host and Nonlinear Crystals II, Proc. SPIE*, vol. 1863, pp. 123-130, 1993.
- [78] X. X. Zhang, et al., “Temperature and concentration dependences of  $\text{Ho}^{3+}$  to  $\text{Yb}^{3+}$  energy transfer in  $\text{Yb}^{3+}$ ,  $\text{Ho}^{3+}$  codoped  $\text{KYF}_4$ ,” *Journal of Luminescence*, vol. 60, pp. 878-881, 1994.
- [79] T. Rothacher, W. Luthy, and H. P. Weber, “Diode pumping and laser properties of  $\text{Yb:Ho:YAG}$ ,” *Opt. Commun.*, vol. 155, pp. 68-72, 1998.
- [80] A. A. Nikitichev and V. A. Pis'mennyi, “1 W CW 2.12  $\mu\text{m}$  Lamp Pumped Room Temperature YAG:Yb-Ho Laser,” in *Laser Optics '95. Solid State Lasers, Proc. SPIE*, vol. 2772, pp. 35-36, 1995.
- [81] R. H. Stolen, “Phase-Matched-Stimulated Four-Photon Mixing in Silica-Fiber Waveguides,” *IEEE J. Quant. Elect.*, vol. QE-11, pp. 100-102, 1976.

- [82] P. L. Baldeck and R. R. Alfano, "Intensity Effects on the Stimulated Four Photon Spectra Generated by Picosecond Pulses in Optical Fibers," *J. Lightwave Technol.*, vol. LT-5, pp. 1712-1715, 1987.
- [83] T. Mirtchev and J. Klein, "Optimizing software aids Raman amplifier design," *WDM Solutions*, pp. 71,72,74,75, July, 2001.
- [84] K. O. Hill and G. Meltz, "Fiber Bragg grating technology fundamentals and overview," *J. Lightwave Technol.*, vol. 15, pp. 1263-1276, 1997.
- [85] S. A. Vasiliev, E. M. Dianov, D. Varelas, H. G. Limberger, and R. P. Salathe, "Postfabrication resonance peak positioning of long-period cladding-mode-coupled gratings," *Opt. Lett.*, vol. 21, pp. 1830-1832, 1996.
- [86] O. Deparis, et al., "Bandpass filters based on  $\pi$ -shifted long-period fiber gratings for actively mode-locked erbium fiber lasers," *Opt. Lett.*, vol. 26, pp. 1239-1241, 2001.
- [87] S. J. Matthews, "The pursuit of power," *Laser focus world*, pp. 103-110, September, 2000.
- [88] K. Boucke, "In Search of the Ultimate Diode Laser - Optial damage, heat dissipation and brightness will limit diode laser power, but we are not near the limit yet.," *Photonics Spectra*, pp. 122-124,126, September, 2001.
- [89] A. K. Goyal, P. Gavrilovic, and H. Po, "Stable single-frequency operation of a high-power external cavity tapered diode laser at 780 nm," *Appl. Phys. Ltrs.*, vol. 71, pp. 1296-1298, 1997.
- [90] A. Schoof, J. Grunert, S. Ritter, and A. Hemmerich, "Reducing the linewidth of a diode laser below 30 Hz by stabilization to a reference cavity with a finesse above  $10^5$ ," *Opt. Lett.*, vol. 26, pp. 1562-1564, 2001.
- [91] B. Chann, I. Nelson, and T. G. Walker, "Frequency-narrowed external-cavity diode-laser-array bar," *Opt. Lett.*, vol. 25, pp. 1352-1354, 2000.
- [92] NRL/Boeing, "SRS/FO Downshift,",, DOD Joint Technology Office.

| REPORT DOCUMENTATION PAGE  |  |   |                | Form Approved<br>OMB No. 0704-0188                              |   |
|--|--|---|----------------|---|---|
| <p>The public reporting burden for this collection of information is estimated to average 1 hour per response, including the time for reviewing instructions, searching existing data sources, gathering and maintaining the data needed, and completing and reviewing the collection of information. Send comments regarding this burden estimate or any other aspect of this collection of information, including suggestions for reducing the burden, to Department of Defense, Washington Headquarters Services, Directorate for Information Operations and Reports (0704-0188), 1215 Jefferson Davis Highway, Suite 1204, Arlington, VA 22202-4302. Respondents should be aware that notwithstanding any other provision of law, no person shall be subject to any penalty for failing to comply with a collection of information if it does not display a currently valid OMB control number.</p> <p><b>PLEASE DO NOT RETURN YOUR FORM TO THE ABOVE ADDRESS.</b></p> |  |   |                |   |   |
| 1. REPORT DATE (DD-MM-YYYY)<br>12-2001   |  | 2. REPORT TYPE<br>Doctoral Dissertation |                | 3. DATES COVERED (From - To)<br>Sep. 1998 - Dec. 2001           |   |
| 4. TITLE AND SUBTITLE<br>LASER INTENSITY SCALING THROUGH STIMULATED SCATTERING IN OPTICAL FIBERS   |  |   |                | 5a. CONTRACT NUMBER   |   |
|  |  |   |                | 5b. GRANT NUMBER  |   |
|  |  |   |                | 5c. PROGRAM ELEMENT NUMBER                                      |   |
| 6. AUTHOR(S)<br>Russell, Timothy H., Capt, USAF  |  |   |                | 5d. PROJECT NUMBER<br>00 NE 071 RR#FQ8671-0001165               |   |
|  |  |   |                | 5e. TASK NUMBER   |   |
|  |  |   |                | 5f. WORK UNIT NUMBER  |   |
| 7. PERFORMING ORGANIZATION NAME(S) AND ADDRESS(ES)<br>Air Force Institute of Technology<br>Graduate School of Engineering and Management (AFIT/EN)<br>2950 P. Street, Building 640<br>WPAFB, OH 45433-7765   |  |   |                | 8. PERFORMING ORGANIZATION<br>REPORT NUMBER<br>AFIT/DS/ENP/02-3 |   |
| 9. SPONSORING/MONITORING AGENCY NAME(S) AND ADDRESS(ES)<br>Howard Schlossberg<br>AFOSR/NE<br>Air Force Office of Scientific Research<br>801 North Randolph Street Rm 732<br>Arlington, VA 22203  |  |   |                | 10. SPONSOR/MONITOR'S ACRONYM(S)                                |   |
|  |  |   |                | 11. SPONSOR/MONITOR'S REPORT<br>NUMBER(S)                       |   |
| 12. DISTRIBUTION/AVAILABILITY STATEMENT<br>APPROVED FOR PUBLIC RELEASE; DISTRIBUTION UNLIMITED   |  |   |                |   |   |
| 13. SUPPLEMENTARY NOTES  |  |   |                |   |   |
| 14. ABSTRACT<br>The influence of stimulated scattering on laser intensity in fiber optic waveguides is examined. Stimulated Brillouin scattering (SBS) in long, multimode optical waveguides is found to generate a Stokes beam that propagates in the fiber LP01 mode. Additionally, the same process is found to combine multiple laser beams into a single spatially coherent source. Limitations in beam cleanup and combining are also investigated to identify ways to overcome them. The last portion of the dissertation theoretically examines suppression of stimulated Raman scattering in fibers to eliminate the restriction this imposes on the power of a fiber laser or amplifier. The suppression was modeled using both a holmium dopant and adding a long period grating to the fiber.  |  |   |                |   |   |
| 15. SUBJECT TERMS<br>Lasers, Optics, Fiber Optics, Nonlinear Optics, Electromagnetic scattering, Coherent scattering, Light scattering, Raman scattering, Stokes radiation   |  |   |                |   |   |
| 16. SECURITY CLASSIFICATION OF:<br>a. REPORT U   |  | b. ABSTRACT U                           | c. THIS PAGE U | 17. LIMITATION OF ABSTRACT<br>UU                                | 18. NUMBER OF PAGES<br>204                                      |
|  |  |   |                | 19a. NAME OF RESPONSIBLE PERSON<br>Won B. Roh, AFIT/ENP         | 19b. TELEPHONE NUMBER (Include area code)<br>937-255-3636 x4509 |